AECL EACL

AECL Research EACL Recherche

AECL-11016, PR-PHY-7

Progress Report
Physical Sciences, Physics Division

1993 July 1 - December 31

May 1994 mai

AECL Research

PHYSICS DIVISION

Progress Report

1993 July 1 - December 31

edited by M. Harvey

Chalk River, Ontario

1994 May

AECL-11016

AECL Research

PROGRESS REPORT

PHYSICAL SCIENCES

PHYSICS DIVISION

1993 July 1 - December 31

PR-PHY-7

Chalk River Laboratories
Chalk River, Ontario K0J 1J0

1994 May

AECL-11016

CONTENTS

AECL Research

PHYSICAL SCIENCES
PHYSICS DIVISION

STAFF LIST

1993 July 1 - December 31

Vice-President, Physical Sciences	**G. Dolling**
Executive Assistant	**M.E. Humphries**
Executive Administrative Assistant	**T. Ingram**
Director, Physics Division	**M. Harvey**
Administrative Assistant	**J. Vaudry**
Unit Administrative Assistant	**M.E. Carey**
Unit Office Assistant	**J. Charbonneau**

PHYSICS DIVISION SUMMARY

Despite the continuation of both fiscal restraint and a hiring freeze, Physics Division is still committed to doing world-class research. We did boost the strength of our neutron scattering group this term with a research associate who will strengthen the ANDI (Applied Neutron Diffraction for Industry) group in its leadership role in applying neutrons to materials research. It is particularly pleasing to note that over the past six months alone, about 50 external scientists (about half from abroad) came to use the neutron scattering facilities at NRU. This truly establishes the facilities as a Canadian national resource.

The group that has been investigating microwave properties of materials (Ron Hutcheon, Mark de Jong, Fred Adams and Blair Smith), together with colleagues from Fuel Engineering (Geoff Wood) and Fluid Sealing and Dynamics (Jim McGregor) were honoured by the Board of Governors of the International Microwave Power Institute. Their paper on "A System for Rapid Measurement of RF and Microwave Properties up to 1400°C" was selected as the most significant scientific and technical contribution to the Journal of Microwave Power during the 1992 year.

Increased interactions with the Reactor Development Operating Unit and concerns over the decreasing availability of neutron irradiation facilities have led to growing interest in the use of electron linac-based irradiation facilities for studies of critical CANDU materials. The Topical Review in this report by Ron Hutcheon gives an overview of this activity from the accelerator physics perspective.

The 13 MeV, 4 kW (average) PHELA accelerator, which has been used over the past several years as a commercial irradiator and as an experimental facility for accelerator science, is being upgraded to provide extended, reliable operation with a minimum of operator intervention. Experiments under consideration will use the electron beam either as an intense source of radiation or as a high-quality heat source that can be used in a very controlled manner. The latter use is serving as an impetus to studying the beam optics of electron linacs with the best available computer codes. Efforts are under way to acquire a PC version of PARMELA that includes the effects of coupling slots.

Good agreement has been found in a detailed comparison between theory and experiment for the Laser Plasma Beat Wave accelerator. A lower energy electron injector (4 MeV vs present 10 MeV) has been installed in the experiment and is being commissioned. This lower energy linac exhibits better beam quality and an injection energy that is better matched to the characteristics of the excited laser-plasma.

The RFQ1 hardware that was transferred to the Los Alamos National Laboratory at the termination of work on ion linacs at CRL is now being commissioned with some assistance from CRL. The assembly, which is identified at LANL as CRITS (Chalk River Injector Test Stand), has gone very smoothly and first beam was extracted from the ion source in mid-November.

In the Condensed Matter Physics program, detailed analysis of data from liquid ^{4}He has shown its behaviour to be remarkably similar in some respects to that of the classical noble gas fluids. Extensive work is reported on the heavy fermion compound URu_2Si_2 to elucidate and interpret the anomalously low moments observed in these systems. The first reflectrometry measurements at Chalk River are reported on Co-Re multilayers, while the first measurements on a single crystal specimen of a frustrated pyrochlore ($CsNiCrF_6$), permit a detailed comparison with a simple model for its structure.

Results from the Molecular Physics program include a study of the differing structures of ice grown in an electric field. Work on silicates includes refinement of the crystal structures of several Li-silicates and measurements of phonon dispersion curves in a natural chain silicate. Details of the order/disorder transition in ND_4Cl have been investigated in a joint refinement of data from isotopically pure ^{14}N and ^{15}N samples. The phase transition in KNO_3 is compared with that for the isomorphic compound $CaCO_3$. Phase transitions in the antifluorite $(ND_4)_2PdCl_6$ were studied, while the cation ordering was determined for a series of solid solutions of a synthetic spinel.

Atomic ordering in the new intermetallics Al_3Ti-X (X=Ag, Fe, Ni, Mn) was extensively investigated in the Materials Science program. The aberrations occurring in measurements of strain near surfaces were systematically investigated and test measurements were carried out on peened Waspaloy. Texture development in hot rolled Al alloys was studied, as was texture in the minority phases of pressure tube material.

In the Theory program a code to calculate the multiphonon expansion of the incoherent scattering function was written and it was applied in the analysis of the phonon density of states for amorphous and crystalline ice. Further calculations were made to develop improved understanding of superconductivity and a theory for the conductivity of vortex cores was proposed. A study of the effects of multiple scattering and wavelength dependent attenuation on residual strain measurements in steel plates has begun.

The Neutrino Physics program continues to carry out quality assurance on the acrylic sheets for fabrication of the SNO (Sudbury Neutrino Observatory) detector. A silicon diode cryotrap for monitoring the D_2O radiopurity in the detector has been designed and fabricated. A calibration scheme has been proposed for the SNO detector in which short-lived sources are produced and transported rapidly into the detector for a fast gas transport system. Several possible sources are being investigated for suitability. Additional funding to complete the SNO project has been approved. The underground laboratory and detector excavations are being converted into usable

space. The geodesic support structure for the photomultiplier tubes was test assembled and delivery of the photomultiplier tubes is on schedule.

As part of the Nuclear Data and Modelling program, the sensitivity of self-powered detector probes to mixed electron and gamma-ray fields was studied by Monte Carlo methods. The results were compared with measurements using ^{60}Co and ^{192}Ir gamma rays. Results from codes to carry out radiation shielding analysis for space missions were compared with those from Monte Carlo calculations. Data from Bubble Detector spectrometers flown in space missions were analyzed.

M. Harvey, B.M. Powell and J. Ungrin

TOPICAL REVIEW

The Basics of Radiation Damage by Particles > 1 MeV Energy

R.M. Hutcheon

During this report period, Accelerator Physics Branch, in collaboration with Fuel Channel Components Branch, has undertaken an ambitious, unique series of experiments to prove the feasibility of using high energy (≥ 10 MeV) electron beams for out-reactor irradiation of bulk samples of pressure-tube materials. The goal is to develop an accelerated test for first level screening of in-reactor corrosion (oxidation) performance. The initial experiment, a 700-hour run at $\approx 450°C$ on Zr-2.5Nb pressure-tube material, is to determine whether electron irradiation can produce the same microstructural changes as are seen in in-reactor irradiation, especially those that are, at present, believed to contribute to corrosion behaviour. Specifically, the test is to determine whether precipitates rich in β-phase niobium form in the interior of the α-phase zirconium grains. The experiment is being performed at a beam density of ≈ 6 A$\cdot$ m^{-2} ($4 * 10^{15}$ e$\cdot$ cm$^{-2}\cdot$ s^{-1}) which is estimated to give a "damage rate" of $\approx 1 * 10^{-6}$ dpa/s (displacements per atom per second). The 700-hour run ($\approx 1 * 10^{22}$ e $\cdot$ cm^{-2} fluence) should produce ≈ 2 dpa.

It is the combination of technologies and skills available in Accelerator Physics Branch that make the experiment possible. Advantage will be taken of expertise in nuclear physics, particle-interactions, high-temperature, high cooling-rate component design and manufacture, and specific high-energy electron accelerator and beam manipulation experience.

This review is designed as an introduction to the materials science side of the subject, but with a bias toward relevance to the present experiment.

Reviews of radiation damage often compare charged-particle-induced damage with that produced by ≈ 1 MeV neutrons during reactor irradiation (although recently fusion systems have generated interest in 14 MeV neutron damage). To determine the conditions of a charged-particle experiment which will produce the same measure of radiation effect as neutron irradiation, we must be able to understand the differences in long-term radiation damage resulting from differences in "particle type", temperature, dose and dose rate.

The particle type determines the short-term distribution of damage in the material lattice, while the temperature is important when considering the evolution of the damage features in a specific material. Although total dose is important in characterizing damage, the amount of primary damage - *i.e.*, the number of lattice vacancies or the number of interstitial atoms - often reaches an equilibrium value at low dose. For example, an equilibrium in the vacancy concentration (between 10^{-3} and 10^{-4} per atom) is established in $\approx$ two weeks in a CANDU pressure tube at the normal operating fast-neutron flux of $\approx 4 * 10^{17}$ n $\cdot$ m^{-2} $\cdot$ s^{-1}. Deterioration of the material continues after this, so the rate of evolution of new collective chemical and

microstructural features also depends upon time and dose rate through the values of diffusion constants (some of which are enhanced by the presence of radiation), chemical rate constants, and the driving force of chemical potentials (some of which are radiation induced).

The bombarding particle type determines the efficiency for production of atomic displacements and the initial damage morphology. The local displacement density (associated with cascade generation), the overall efficiency of generating displacements, and the energy transferred to the primary knock-on atom (PKA) can vary widely with particle type. Here PKA is defined as the first atom, in a resulting cascade, to receive the energy from the impinging particle.

Neutrons and heavy ions produce dense displacement cascades in which substantial recombination occurs during the cooling or quenching phase. The fraction of the "ballistically" produced Frenkel pairs (interstitial atoms and associated vacancies) that survive the cascade quench (rapid recombination of interstitials and vacancies in the cascade region), and are available for long range migration are referred to variously as "freely migrating" or "available migrating" defects. Present estimates suggest that, depending on the material and the primary heavy particle type, between 2% and 10% of the cascade displacements survive to become freely migrating defects. Electrons however, produce some widely spaced Frenkel pairs (FP) and some small cascades which have a lower probability of recombination. Protons produce small widely spaced cascades and many isolated FPs arising from the Coulomb interaction and therefore, fall between the extremes in displacement efficiency defined by electrons and neutrons.

The first problem in determining the equivalence between the radiation effect from charged particle and neutron irradiation is the use of a common dose unit. The basic (measurable) dose unit for neutron irradiation is n/cm^2 (E > x MeV) where x is some energy threshold. For charged particles it is the integrated current or charge fluence, Q/cm^2. The particle beam community is accustomed to reporting dose in units of dpa (displacements per atom) and dose rate in dpa/s. Dpa is not a measured quantity, but is instead calculated, based on integrated charge density and one of several models for particle interaction with the material. Although somewhat more complicated, because of the spectrum of neutron energies, the conversion from n/cm^2 (E > *x* MeV) to dpa was done in the early days of neutron damage studies to compare the results of different neutron sources. In a typical CANDU reactor, the fluence of fast neutrons (E > 1 MeV) at the pressure tube mid-section, accumulated over one year, is $\approx 1.3 * 10^{25}$ $n \cdot m^{-2}$. This is generally considered to produce ≈ 1 dpa of ballistic damage (*i.e.*, before rapid recombination) in the pressure tube material, which will be called 1 dpab.

The "ballistically" determined value of dpa is not an appropriate unit for dose comparisons where dense cascades are generated, since recombination (and thus the generation of freely migrating point defects) depends on the temperature and physical characteristics of the sample. At the same time, the remaining local high density of defects (after a cascade) may nucleate new structures (*e.g.*, voids, if dissolved gas were present, or precipitates of new crystal types) which might not occur in the absence of cascades. If the particular radiation damage effect being studied is solely dependent on the number of freely migrating point defects generated

in a CANDU pressure tube material, then the one-year accumulated neutron fluence of $\approx 1.3 * 10^{25}$ $n \cdot m^{-2}$ ($E > 1$ MeV) is roughly equivalent to 0.05 dpa.

For the present experiment using 11 MeV electrons, the efficiency of generating displacements (Frenkel pairs which are free to migrate) is ≈ 1 dpa for a fluence of $3.7 * 10^{25}$ electrons$\cdot m^{-2}$. The fast-neutron fluence required to generate the same 1 dpa of freely migrating defects is $\approx 2.5 * 10^{26}$ $n \cdot m^{-2}$ ($E > 1$ MeV), assuming a 5% yield after the cascade quench - *i.e.*, assuming 20 dpab of fast neutron damage!

A general schematic of the initiation and evolution of radiation damage is shown in Figure 1 *(S. Ishino - Time and Temperature Dependence of Defect Production)*, where, for example, the time scale for the previously mentioned recombination within a multiple-cascade process is shown to be $\leq 10^{-6}$ seconds. After this quenching or short-term-annealing period, in which the non-thermal energy distribution thermalizes, what remains are freely migrating point defects or cascade-produced clusters of defects. At a rate that depends on the temperature and ambient radiation dose-rate, these defects start diffusing through the material, and can eventually coalesce into new collective structures through nucleation and growth at special sites in the structure. Depending upon the energetics, one may have dislocation loops, voids, small defect clusters or stacking-fault tetrahedra.

Dislocation loops are ring-like features which can be seen by TEM (Transmission Electron Microscope) observations of very thin samples of irradiated material. Point defects coalesce until at some point it is more energetically favourable to form a single-atom-thick disc on preferred planes in the lattice. The local bending of the lattice planes near the edge of the disc diffracts the electrons slightly differently in the beam, producing contrast and making the edge of the disc visible. The preferential coalescing or collecting of point defects into groups on specific crystallite planes can produce radiation-induced swelling or expansion of materials, which is anisotropic if the material is textured or oriented (*i.e.*, if the individual crystallites lie in a preferred direction, such as is generated in the production of the CANDU pressure tube material by cold rolling).

The main driving forces for freely migrating defect motion are concentration gradients, which are generated by the spatial separation of the sources and sinks of the defects. The discussion, so far, has largely concentrated on the sources of defects. The basic sinks are free surfaces, dislocations (the result of cold work), and impurity clusters. Interstitials largely migrate to free surfaces, the natural sink for migrating particles, although they also recombine with vacancy structures (*i.e.*, vacancy dislocation loops). Recombination with interstitials appears to be the main sink mechanism for vacancies, although, at high fluence levels in some materials, void formation and growth forms a vacancy sink. Vacancy trapping at solute atoms may also be important.

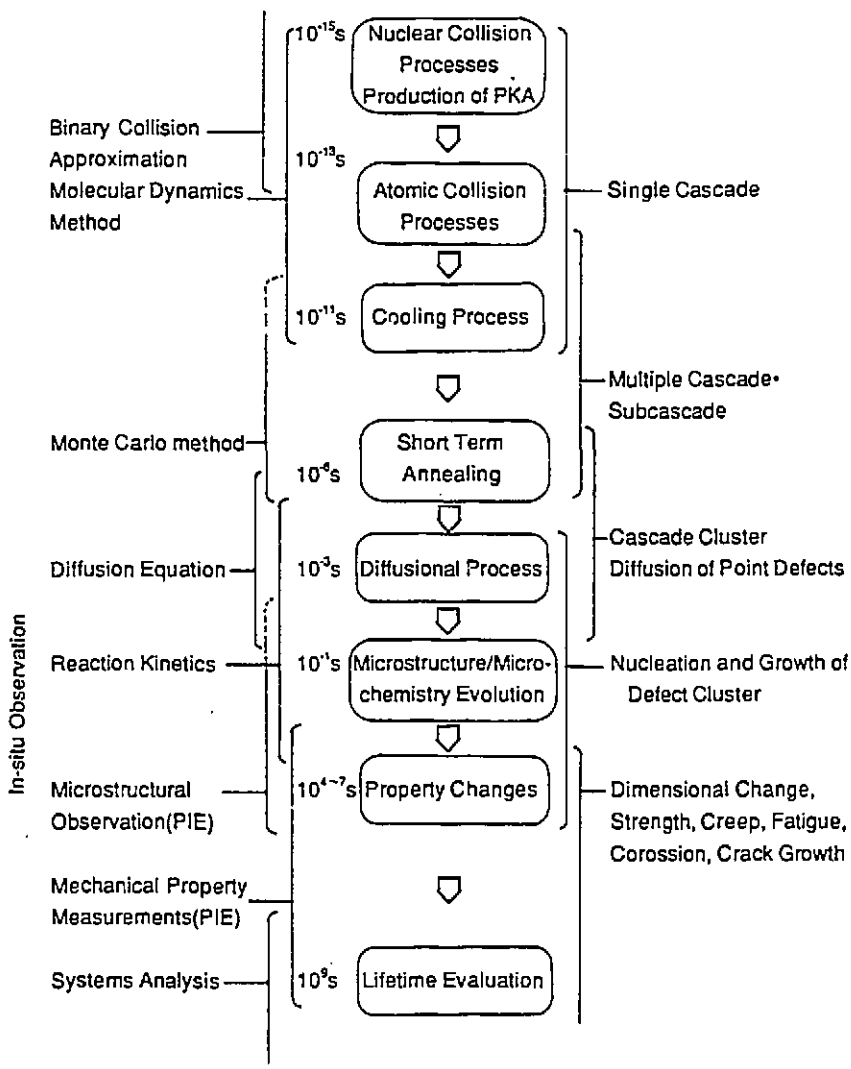

Fig. 1. Scope of time evolution of radiation damage with the means of approach and representative phenomena for various stages.

Another important sink for interstitials, within the CANDU pressure tube context, is the nucleation and growth of new crystalline species, especially within the alpha zirconium grains of the Zr-2.5Nb material (an alloy of zirconium and 2.5% niobium). At 570 K, the niobium is substitutional (in thermal equilibrium up to 0.6% niobium) and is uniformly distributed throughout the alpha phase zirconium lattice forming a supersaturated solid solution with ≈1% niobium. Neutron irradiation to a fluence of $> 1 * 10^{25}$ n · m^{-2} at 570 K (297°C) causes the formation of small precipitates of beta phase niobium (5-10 nm diameter) within the alpha grains. This migration, nucleation and growth of niobium particles is miniscule unless radiation is present. When occurring, it results in the reduction of niobium in the lattice to levels below saturation, which appears pivotal in increasing the corrosion (oxidation) resistance of the material.

The general classification of radiation damage in metals resulting from point defects can be done on the basis of point-defect mobility, and depends on temperature. The temperature range can be divided into four regions. In the highest temperature range both interstitial atoms and lattice vacancies move thermally very fast. In the medium temperature range interstitials can move but vacancies move only slowly (this second medium temperature range is not defined solely by thermal jumps of vacancies, but includes their radiation-induced diffusion, and thus is dose rate and "particle type" dependent). For low temperatures, only interstitials can move. At the lowest temperatures neither interstitials nor vacancies move.

The basic radiation damage properties of the zirconium alloys used in CANDU reactors are reviewed in CRNL-1208, including a simple summary of the dependence on temperature during the irradiation. At an irradiation temperature of 575 K (300°C) and fluences $> 3 * 10^{23}$ n·m^{-2}, many very small loops and "black spot" features are seen. At 775 K (500°C) the defects are larger and less numerous, and more are resolvable as loops rather than "black spots". The dependence on fluence is such that, regardless of temperature, no damage is resolvable at less than $\approx 3 \times 10^{23}$ n·m^{-2} (≈ 0.02 dpab).

The present state of understanding of the evolution of microstructure in Zr-2.5Nb alloy core components is discussed in AECL-10844, under the topics of dislocation structure and phase structure. Neutron irradiation of Zr-2.5Nb at 550 K results in the production of a high density of small (15 nm) <a>-type dislocation loops (whose density saturates at $1 * 10^{25}$ n·m^{-2} fluence). At 550 K and fluences $> 2 * 10^{25}$ n·m^{-2}, small β-Nb precipitates are found (5-10 nm) distributed through the α-zirconium grains. At higher temperatures (570 K), these precipitates are seen at fluences as low as $\approx 1 * 10^{25}$ n·m^{-2} (~ 1 dpab).

After irradiation of Zr-2.5Nb, there is a general expansion of the α-phase lattice which, because it does not occur with heat alone, is attributed to the precipitation of niobium from the supersaturated solid solution. Under similar irradiation, Zircaloy-2 pressure tube material shows a lattice contraction! The iron impurity (500 to 1000 ppm) in Zr-2.5Nb material, which initially is concentrated in the β-phase boundary region, is found, **after irradiation**, to be

dispersed through both the α and β phases. This is considered to be a radiation-induced effect, for it does not occur with heat alone.

The understanding of the corrosion (oxidation) of Zr-2.5Nb pressure tube material is not complete, either from an engineering or basic science point of view. The latest findings suggest that the oxidation rate in the CANDU pressure tube (and thus the deuterium uptake rate - which is apparently related to oxide formation) is dependent on the amount of niobium dissolved in the α-zirconium lattice. Recent experiments on post-irradiation corrosion in high-temperature autoclaves have found that a minimum in the corrosion rate occurs when the dissolved niobium is at 0.03 wt% in the α-zirconium grains. Short-term (60-day) experiments on fresh Zr-2.5Nb material in an NRU reactor loop showed reduced corrosion for samples in the radiation field compared with those just outside the radiation field, but otherwise in the same high-temperature, high-pressure loop environment. However, this 60-day period (≈0.16 dpab) is considered too short for complete formation of niobium precipitates in the α-zirconium. Thus, although the understanding of the corrosion behaviour of Zr-2.5Nb in the CANDU reactor is quite advanced, there are still some crucial questions to be answered and reaction mechanisms to be clarified and quantified.

The long-term goal of the present series of high energy electron irradiation experiments is to demonstrate that electron-induced damage is an adequate analogue to "in-reactor" damage, to the extent that electron irradiation can provide a valid accelerated corrosion test which can be used for initial screening of posible new pressure tube materials, prior to ultimate long-term in-reactor tests. In the course of this validation, it will be necessary to demonstrate that the high dose rates, inherent to the present electron accelerator irradiations, still provide a valid test. If the present electron irradiation experiment were based on 24-hour accelerator operation, it would take 16 days to accumulate ≈1 dpab of point defect damage. To generate the equivalent number of "freely migrating" defects in NRU or in a CANDU reactor would take 1 to 2 years. The present sample size, although smaller than the coupons traditionally used for reactor irradiations, is thought to be large enough to be representative of bulk material. A series of tests are planned by Reactor Materials Research Branch to check this in detail. The culmination of the present series of experiments will be the demonstration of corrosion of small samples of pressure tube material in a pseudo CANDU reactor environment - *i.e.*, in flowing, controlled chemistry, 300°C heavy water in the presence of radiation.

TOPICAL REVIEW

E.D. Earle

Sudbury Neutrino Observatory (SNO)

The second Topical Review in this report summarizes the development of the SNO project, which has captured the imagination internationally.

The Sudbury Neutrino Observatory (SNO) will use 1000 tonnes of heavy water, on loan from AECL, to detect elusive particles called neutrinos emitted from the centre of the sun and from exploding stars. Neutrinos are fundamental particles, unique in that they interact only via the weak force and are unaffected by the strong and electromagnetic forces. Therefore they are the only particles that can emerge directly from the thermonuclear furnaces at the cores of stars. By comparison, other messengers from a star's core take a million years to reach its surface. By detecting neutrinos, scientists gain direct information about the fusion processes that are otherwise concealed and, in addition, they can measure crucial properties of the neutrinos themselves, such as their mass.

Heavy water is an excellent medium to detect neutrinos, but large quantities are required, because neutrinos interact so infrequently with matter. For example in one day, only about 20 of the 10^{22} neutrinos passing through the heavy water will interact. The signature of a neutrino interaction with the water will be a flash of light from a high speed electron. In SNO this will be measured by an array of 9000 photomultiplier tubes surrounding the heavy water. The heavy water will be contained in a giant acrylic bottle immersed in 8000 tonnes of normal water. The acrylic is transparent and so allows the light to reach the phototubes.

There are many other interactions which produce high speed electrons (e.g., interactions with cosmic rays), and these produce an unwanted background to the neutrino signal. The main technical challenge to the SNO scientists is to construct a detector where these unwanted interactions are as low as possible and measurable. The detector will be built in a cavern as high as a 10 story building, two kilometres underground in INCO's Creighton mine, near Sudbury. The rock overburden will shield the heavy water from the cosmic ray background, while the 8000 tonnes of normal water will shield it from the radioactivity in the rock and the phototubes.

The acrylic must be made to stringent specifications in regard to the radioactive content and the optical properties. Both the light and heavy water must be continually filtered to remove unwanted radioactivity. The laboratory, when built, will be the lowest radioactivity site on earth.

The civil work in excavating the cavern and preparing the site for the installation of the phototubes, acrylic vessel, electronics and water is within weeks of completion. The components of the structure to hold the phototubes have been shipped to Sudbury ready to be taken

underground for assembly. Most of the phototubes have been purchased. The 122 acrylic panels for the giant bottle have also been purchased, and are being shaped and machined in readiness for shipping to Sudbury, where the assembly and bonding will be done underground. The water-purification plants are operating at surface locations and monitoring systems are being assembled. The water fill is planned for late 1995, with data taking beginning immediately thereafter.

AECL has a small research team, led by Davis Earle, working on the SNO project as part of the international collaboration of over fifty scientists from other institutions in Canada, USA and UK. In addition, one AECL staff member (Duncan Hepburn) is permanently located at the Creighton Mine as the SNO site manager, with responsibility to coordinate all the scientific activities at the site and be the day-to-day interface with INCO mining authorities.

SECTION 1

ACCELERATOR PHYSICS BRANCH

Edited by J. Ungrin

CONTENTS

1.1 ACCELERATOR PHYSICS BRANCH - STAFF LIST

BRANCH MANAGER: J. Ungrin

Professional Staff

F.P. Adams
R.J. Burton
S.T. Craig
M.S. de Jong
N.A. Ebrahim
C.R.J. Hoffmann
R.M. Hutcheon
G.E. McMichael (1)
J.Y. Sheikh
T. Taylor

Technical Staff

S.B. Alexander
A.D. Davidson
R.W. Davis
G. Frketich
I.L. McIntyre
W.L. Michel
G.F. Morin
J.F. Mouris
L.W. Shankland
B.H. Smith
D.L. Smyth

Mechanical Laboratory

R.J. Bakewell
R.J. Kelly
J.F. Weaver

Laboratory Services

K.T. McKee

Secretarial Staff

M.A. Trecartin

Casual Part-time

A.A. Hammond (2)
R.J. Kim (3)

Students

M.D. Lucuta
B.A. Walker (4)
M.J. Tooley

(1) Retired 1993 August 18.
(2) Science Academy Tutor from the University of Guelph, departed 1993 August 20.
(3) Summer student, departed 1993 August 27.
(4) Resigned 1993 July 09.

1.2 SUMMARIES

Electron Linear Accelerator Development

The BEDROCS and PHELA accelerators are being maintained as branch facilities for both accelerator physics and irradiation studies. The PHELA control system is being upgraded and computerized to permit "hands-off" operation.

Electron Beam Dynamics

Copies of the electron linear accelerator beam dynamics code PARMELA and the electron gun simulation code PBGUN were acquired and installed and tested on a personal computer.

Laser Acceleration of Particles

Detailed comparisons of theory and experiments on electron acceleration by laser-driven relativistic electron plasma waves show excellent agreement.

Superconducting Cyclotron

Transfer of computer source code and data files from the Cyber 990 to personal computers continued, in response to the announced shutdown of the 990 in 1994 May. The task is about 20% completed.

Modifications were made to TRIUMF2 to allow magnetic field maps to be extrapolated to zero current in the outer coil. A data error was corrected in TRIUMF3 and related codes, to remove inconsistencies in calculated first harmonic fields generated by trim rods.

Synchrotron Radiation Source for Canada

The status of synchrotron radiation research in Canada was reviewed in a two-day meeting in Ottawa by an NSERC Synchrotron Light Sources Subcommittee. It is expected that the subcommittee will make its recommendations by mid-1994.

Application of Radiofrequency Waves to Materials

Development work continued on multi-mode cavity systems and on measurement of properties of industrially-relevant materials. The collaboration with the University of Florida is increasing our visibility in the area of industrial ceramics.

Chalk River Injector Test Stand (CRITS)

The RFQ1 system was reassembled at Los Alamos National Laboratory (LANL) under the acronym CRITS (Chalk River Injector Test Stand). The microwave proton ion source generated a 78 mA beam of 50 keV hydrogen ions within eight partial days of operation.

Ion Source Technologies

Beams of He^- and O^- were accelerated from a permanent magnet microwave ion source installed on one of the TASCC decks.

1.3 INDIVIDUAL REPORTS

1.3.1 Electron Linear Accelerator Development

F.P. Adams

Two 3 GHz linacs are housed in a common shielding tunnel in Bldg. 610. The high-power accelerator, PHELA, is used for a range of commercial and CANDU materials irradiations and for the development of dosimetry. The second accelerator, BEDROCS, is used for lower-energy irradiations.

1.3.1.1 BEDROCS

F.P. Adams

The BEDROCS "rotated slot" accelerator continues to be installed in the PHELA tunnel, and is being maintained as a branch facility. The accelerator is capable of producing electron beams at an energy of up to 6 MeV and a power level of up to 350 W. The "aligned-slot" structure, which had been used in the BEDROCS program and which produces a higher-quality beam, has been transferred to the plasma beatwave accelerator experiment.

1.3.1.2 PHELA

F.P. Adams, A.D. Davidson, I.L. McIntyre, J.Y. Sheikh and B.H. Smith

The PHELA accelerator is being maintained as a branch facility, and produces an electron beam at an energy of up to 13 MeV and a power level of up to 4 kW.

A computer has been added to the accelerator control system to log data and reduce operator workload. The computer is an 80386-based PC-compatible running LabView software under Microsoft Windows. Using this software package, a control program has been developed which provides closed-loop control of sample temperatures and accelerator rf drive frequency. The

computer now produces the accelerator beam pulse trigger signal, and the temperature of the samples is controlled by changing the pulse repetition frequency. The rf frequency tuning- error signal for the computer is derived from the phase of the rf power reflected from the structure, and the computer controls the rf frequency using a frequency-modulated signal generator. The PHELA control system is being upgraded further, with unattended operation the long-term goal.

To automate the accelerator for extended, unattended operation with a high availability factor, it was necessary to evaluate the existing hardware and control system for possible upgrade and to assess the spares available. Some spares had been purchased in the past; others are being ordered as the evaluation and upgrading of the accelerator continues. Drawings for the Cober rf system were marked-up over the years to show modifications, but they were not updated, since there were no originals available. With the assistance of a design draftsman, all of the Cober drawings have been updated on a CAD system and have been converted to standard AECL-RC drawings. Various power distribution drawings for the accelerator have been checked and are being updated as required. Drawings for the accelerator and safety interlocks are also being redrawn to incorporate the modifications and upgrades of the new system.

The travelling-wave tube (TWT) driver that is used to drive the klystron has worked well over the years, but is believed to be approaching the end of its useful life. After examining several options a solid-state driver manufactured by PROCOMM was ordered as a replacement. This 500 watt driver has been received and accepted following tests that compared its performance against the specifications. An interface panel is currently being designed to incorporate this driver into the control system; the interface panel will provide both local and remote operation from the LabView computer.

The capacitors used in the pulse forming network (PFN) that generates the klystron pulse have operated reliably since the system was purchased. The total number of pulses is now approaching the lifetime rating originally specified. To avoid the possibility of an extended forced shutdown if the capacitors failed, a set of replacement capacitors have been obtained. The present plan is to continue with the old capacitors as long as possible.

Two panel meters have been added on the Cober cabinets, to show the thyratron filament voltage and reservoir voltage during startup and operation. The thyratron is used to trigger the PFN, and the voltage readings provide a good check during debugging of problems associated with the rf system.

To upgrade the present interlock system, a complete system based on a programmable logic controller (PLC) has been purchased. The system utilizes a touch screen to provide a user-friendly interface for the accelerator operator. Assembly of the unit is in progress. Programming and incorporation into the main system will follow later.

An operating manual has been written for the accelerator. The present version of the manual describes operation with the TWT driver. This version is being revised to adapt to the operation of the new driver and the associated upgrades.

1.3.1.3 Electron Beam Dynamics

T. Taylor

The source code of the beam dynamics programme, PARMELA (Phase and Radial Motion in Electron Linear Accelerators), was obtained from the Los Alamos National Laboratory (LANL) via the Continuous Electron Beam Accelerator Facility (CEBAF). The code was successfully installed on an 80486 personal computer and is presently being converted to the WATCOM compiler for compatibility with Accelerator Physics Branch standards and, potentially, for increased execution speed. Unfortunately, the acquired version is unable to simulate the influence of the quadrupolar electric and magnetic fields arising from the cavity-to-cavity coupling slots. Possible methods of incorporating these fields, or of acquiring an updated version of the code, are being investigated.

A copy of the new electron gun simulation programme, PBGUNS, was acquired from Thunderbird Simulations of Garland, Texas.

1.3.2 Laser Acceleration of Particles

N.A. Ebrahim

The high-power CO_2 laser laboratory is operated by the branch to study advanced accelerator concepts, laser chemistry and laser surface treatment of pressure tube materials for CANDU reactors.

1.3.2.1 High-Power CO_2 Laser System

N.A. Ebrahim, R.W. Davis and J.F. Mouris

The CO_2 laser system continues to perform reasonably well and several major upgrades have been implemented. The vacuum pumping system on the Lumonics 612 laser amplifier was completely redesigned, components were fabricated and the system re-assembled. The new system has increased the pumping speed significantly.

The laser gas-scrubbing system on the 612 amplifier was also completely redesigned, fabricated and commissioned. This has increased the laser gas recirculation through the ferrocene oven and the molecular sieve, so that oxygen and water vapour impurities produced during the laser discharge are removed more rapidly, thereby reducing gas contamination and arcing in the discharge. Significant improvement in the performance of the amplifier has been observed.

1.3.2.2 Laser Plasma Acceleration Experiments

N.A. Ebrahim, R.W. Davis and J.F. Mouris

Detailed analysis of the experimental data on electron acceleration has been completed. Theoretical estimates of plasma wave amplitude saturation based on mode-coupling theory, collisional damping theory and relativistic theory suggest that wave amplitude is determined by relativistic saturation. The level at which plasma wave amplitude saturates as a result of relativistic detuning of the resonance has been calculated from a one-dimensional, fully relativistic theory. For our experimental conditions, these calculations give a field gradient of 2.2 GV/m. With a plasma length of approximately 1 cm, this electric field gradient corresponds to an energy gain of 22 MeV compared to the energy gain of 16.5 MeV (12.5 to 29 MeV) in our experiments.

Further comparisons between experiments and theory have been made by calculating the output energy spectrum of electrons injected into a plasma wave from a high energy linac. We have conducted extensive three-dimensional computer studies of relativistic wave particle dynamics with a model of the plasma wave which includes longitudinal and radial fields, as well as linear amplitude growth rates and a relativistic model of particle acceleration which includes finite beam emittance. It has been assumed that the plasma wave is linear and that beam loading is negligible. Approximately 450 000 electrons were injected with an energy of 12.5 MeV, randomly distributed over a phase-ellipse with an emittance of 6.2×10^{-7} m·rad (obtained from TRANSOPTR calculations) with a uniform phase distribution between 0 and 2π radians. The calculated output energy spectrum shows electrons accelerated out to approximately 30 MeV, which is in agreement with experimental observations. The normalized accelerated current from our model also shows excellent agreement with experimental observations.

We have also established that the observed acceleration is due to the laser plasma beatwave mechanism, by measuring the acceleration of electrons as a function of the neutral gas filling pressure (and hence the electron plasma density). The variation of the accelerated current shows a clear resonance around a filling pressure of 280 mtorr, which corresponds to a density of 9×10^{15} cm^{-3}. The theoretically calculated electron plasma density from the laser wavelengths used in these experiments (10.59 and 10.25 μm) is 1×10^{16} cm^{-3}. To compare the experimental results with theory, we have used a non-linear, fully relativistic treatment of the plasma waves that includes a mismatch between the laser beat frequency and the plasma frequency. The governing equations describe the growth of the plasma up to saturation. Excellent agreement between theory and experiments was obtained over the entire density range.

1.3.2.3 Linear Electron Accelerator System

R.W. Davis, N.A. Ebrahim and J.F. Mouris

The accelerator system has continued to perform reliably. No major problems were encountered with the transport beamline or the detector system.

Several major modifications to the accelerator system were implemented. The 12.5 MeV accelerator structure was replaced by a 5 MeV BEDROCS structure in order to inject particles at a lower energy. The beam quality from the BEDROCS structure is also expected to be significantly better.

In conjunction with the structure change-over, the control and logging system for the linac were completely upgraded. The modulator controls, power systems, safety interlocks, beamline components and diagnostic equipment were completely rewired to streamline the operation of the accelerator system and improve its reliability.

The cooling system for the accelerator system and beamline magnets was also upgraded with new headers, cooling lines and flow controllers.

1.3.2.4 Beamline Calculations

C.R. Hoffmann

The magnet code GFUN3D has been setup on the Cyber 990 system with the intention of using it to improve the design of the small steering magnets that are distributed along the electron beamline. This code was in Fortran IV and in a form to operate on the obsolete NOS/BE system. After migration to NOS/VE, the code was checked by comparing calculations done previously with the old code (for the superconducting cyclotron magnetic extraction system) against the same calculations for the new code. The results were identical.

1.3.3 Heavy Ion Superconducting Cyclotron

C.R.J. Hoffmann

TASCC Accelerators and Development Branch operate the Chalk River superconducting cyclotron. Accelerator Physics Branch provides assistance in maintenance and operation, and in the design of improved components to enhance performance and reliability.

1.3.3.1 Main Magnet

1.3.3.1.1 Diagnostics

C.R. Hoffmann with G.L. Backmeier (TASCC Accelerators and Development Branch)

A small power supply and a distribution panel have been installed for monitoring magnet pancake-coil temperatures when they go above 10 K. The power supply will provide a dc current of 1 A which flows through both inner and outer coils in series. The distribution panel accepts the input that usually goes to the voltage tap monitors, and makes it available so that the voltage across each pancake can be measured. (The pancake-coil temperature is deduced from the known variation of copper resistivity with temperature.) The task of interlocking the power supply to the dump switch still must be completed. The dump switch must be open to force the current through both coils in series.

1.3.3.1.2 Magnet Power Supply Troubleshooting

L.W. Shankland with G.L. Backmeier (TASCC Accelerators and Development Branch)

Consulting assistance was provided to aid in attempts to resolve unstable operation of the coupled power supplies that drive the inner and outer coils of the magnet. The cause has not yet been identified. The operational solution has been to decrease the gains in the regulation amplifiers.

Repairs were made to a monitoring circuitry in the power supply that trips the supply off when the coil currents violate preset limits; for example, during charging when the outer coil current increases beyond 50 A before the inner coil current reaches 600 A. Investigation showed that a small dc power supply had failed and subsequently opened the interlock chain to prevent operation of the magnet power supply.

1.3.3.2 Foil Changer

J.F. Weaver with J.S.C. Wills (TASCC Accelerators and Development Branch)

The unloader mechanism of the foil changer failed as a result of two pivot pins on the foil grabber working loose and falling off. They had performed satisfactorily for over eight years. New pins, modified to have longer shanks imbedded in the support plate, were fabricated and installed. The new pins were both rivetted and silver-soldered into place. The repaired unloader was reinstalled and returned to service.

1.3.3.3 Computation

1.3.3.3.1 Code Development

C.R. Hoffmann

The code TRIUMF2 has been modified to allow field maps to be calculated for zero current in the outer magnet coil windings. This modification allows additional field maps to be extrapolated outside the measured array of maps, which is of interest for light ions such as ^{3}He. In all cases, coil currents are not allowed beyond the safe operating range of the magnet.

The source code for SUPERGOBLIN has successfully run on a personal computer (see section 1.3.3.3.2) when it was compiled for debugging. However, it does not run when compiled with default options that provide a higher level of optimization than for debugging (a factor of about 8 faster). Several changes in the program are being investigated to correct this problem.

Modifications were made to the TRIUMF3 code, in response to inconsistencies that arose in calculations of first harmonic field corrections generated by trim rods. It was found that the code incorrectly specified maximum magnetic field for the number 9 trim rod set. The data was corrected in TRIUMF3 and in other source codes where similar data was used for first harmonic field calculations.

1.3.3.3.2 File Transfer

C.R. Hoffmann and W.L. Michel, with E.H. Lindqvist (TASCC Accelerators and Development Branch)

Transfer of code and data files from the Cyber 990 computer to fast personal computers continued. This activity is in response to the announcement that the 990 will be shut down 1994 May 31. The personal computers operate under DOS and use the Watcom Fortran 77/386 compiler. About 400 files have been transferred; i.e., the task is about 20% completed.

1.3.4 Synchrotron Radiation Source for Canada

N.A. Ebrahim

In 1993 October, the status of synchrotron radiation research in Canada was reviewed in a two-day meeting in Ottawa by a Synchrotron Light Sources Subcommittee, which is one of the three subcommittees that form the NSERC Ad-hoc Committee on Materials Research Facilities (CMRF). The other two are: "Neutrons", and "Other Facilities" outside the Neutron and Synchrotron categories. Representatives from CISR (Canadian Institute for Synchrotron Radiation) and the Canadian synchrotron community, as well as some foreign experts, were present. The subcommittee is expected to make its recommendations by mid-1994 for future

funding of synchrotron radiation research. There are two probable scenarios. One is to construct a Canadian synchrotron, whereas the other is to fund beamlines on synchrotron sources in the US. Accelerator Physics Branch has an interest in this project from the point of view of designing and constructing specific accelerator components. Representatives presented the Branch capabilities to the CMRF at the October meeting.

1.3.5 Application of Radiofrequency Waves to Materials

1.3.5.1 Studies of RF and Microwave Properties of Materials

R.M. Hutcheon, G.F. Morin, M.S. de Jong, F.P. Adams and A.A. Hammond (DRSA Tutor)

Development work continued on multimode cavity-based systems for measuring high temperature rf properties of industrially relevant and scientifically interesting materials.

An improved ridge-loaded waveguide resonator for permeability measurements on magnetically biased materials is in the test stage. A TM_{ono} cavity for the frequency range 0.9 to 6 GHz was built and is being tested.

The measurement of the high temperature dielectric properties of a selected group of thermal-insulating materials thought to be suitable for use in microwave furnaces is almost complete. Preliminary data has been sent to a few interested industrial groups in the hopes of generating future contacts and commercial contracts.

The dielectric properties of a common soft wood, trembling aspen, were measured by two Deep River Science Academy students. This work was deliberately undertaken to foster the interest of the forest-products industry, that has recently started the manufacturing of softwood composites.

A group at the Mining Research Laboratories of CANMET are interested in development of a simple way to quantatively measure the amount of carbon collected on soot-monitoring filters in mines. The dielectric response of a set of filters loaded with various amounts of soot (supplied by CANMET) was measured between 50 and 600 MHz. There appears to be a threshold associated with the "percolation" limit for conductivity, below which very little response is produced by the soot. A few more measurements are planned to characterize this limit.

C. McDonough, of the Microgavity Research Group at the Jet Propulsion Laboratory in Pasadena, asked CRL to carefully measure the dielectric properties of a Zerodur glass sample, so that they could subsequently determine the accuracy of a dielectric analysis technique they are developing. The group at CAMECO in Saskatoon also assisted by measuring the dielectric properties up to 6 GHz using a different technique.

A simple literature search revealed that the dielectric properties of heavy water had not been carefully measured in the microwave range. The system was carefully calibrated for dielectric values in the range of light water, and then used to measure the dielectric properties between 50 and 600 MHz of both light and heavy water at room temperature. The real part of the dielectric constant of heavy water is 9.7% larger than that of light water, while the dielectric loss tangent of heavy water has a stronger frequency dependence and is up to 1.5 times larger than that of light water in the centre of this frequency range.

1.3.5.2 Joint Studies with University of Florida Materials Engineering Department: The Application of Microwave Processing to Selected Ceramics

R.M. Hutcheon and G.F. Morin

The three previously-mentioned proposals for joint R&D work to be funded by various US agencies (NSF and DOE) were not accepted. The group at the University of Florida report that the present acceptance rate on proposals is $\approx 5\%$.

The academic collaboration is continuing well and has generated five joint papers in the microwave materials processing field. Measurements have been done on many samples to assist Prof. D.E. Clark and his students in the interpretation of their microwave processing results. These measurements include:

(a) Soda-lime silica float glass (PPG Industries) - 30 minutes annealing at 600°C appeared to have no influence on the microwave properties.

(b) Measurements on Corning Glass (code 0317) to 1000°C and on doping salts to 500°C (KNO_3, $AgNO_3$, Ceramicoat) used in experiments on the microwave enhancement of ion diffusion in glasses. These include the first measurements of the complex microwave dielectric constants of the liquid phase of these salts.

(c) Measurements to 1400°C on various doped Boehmite powders (produced by sol-gel precipitation). These powders are used as the binding or joining agent in experiments, to bond together bulk pieces of alumina in a microwave furnace.

1.3.6 Ion Accelerators

1.3.6.1 Chalk River Injector Test Stand (CRITS)

T. Taylor and W.L. Michel

The RFQ1 system, the culmination of almost thirty years of ion linear accelerator development at Chalk River Laboratories, was transferred to the Los Alamos National Laboratory (LANL) shortly after the beginning of the 1993-94 fiscal year. The LANL Accelerator Operations and

Technology (AOT) Division immediately initiated a programme to exploit the technology developed here.

The entire accelerator assembly, including a 50 keV microwave proton ion source, a 1.25 MeV radiofrequency quadrupole (RFQ) and numerous diagnostic devices, was reassembled and has been christened the Chalk River Injector Test Stand (CRITS). The system was reconfigured to conserve space and to eliminate redundant components. A compact high-voltage cage housing only the microwave plasma generator and the mass flow controller replaced the spacious high-voltage cage previously designed to accommodate the obsolete duoPIGatron ion source.

The microwave proton ion source was recommissioned during 1993 November with the support of Accelerator Physics (AP) Branch personnel. A 78 mA beam of 50 kV hydrogen ions was generated within eight partial days of operation. The AOT-10 group manager responsible for the installation was surprised and pleased that the system "works better than anticipated" and "sets a new standard for ease of operation".

The low-power testing of the 250 kW cw klystrode driven rf system for the 267 MHz RFQ was completed with the assistance of Continental Electronics personnel. The driver klystrode was operated at 100 W into a 3 kW load. The crowbar in the final power amplifier was fired. Most of the rf system controls were transferred to the control room.

During the next three months, the LANL schedule calls for the microwave proton source to be extensively characterized; the recommissioning of the rf system is to be completed; and, a high-current cw proton beam is to be accelerated to 1.25 MeV for the first time at LANL. Requests for assistance from CRL are expected for all of these tasks.

1.3.6.2 Ion Source Technologies

T. Taylor with J.S. Wills (TASCC Accelerators and Development Branch)

The microwave ion source technology developed for the Accelerator Physics Branch ion linear accelerator programme was successfully adapted to the requirements of the TASCC Accelerators and Development Branch. This work has been carried out by personnel in the TASCC Division with the assistance of Accelerator Physics Branch.

The prototype microwave ion source was fitted with an oven and a beam of Bi^+ was generated from elemental bismuth.

A crude plasma generator with permanent magnets replacing the solenoids was assembled. The microwave efficiency, although significantly reduced, was still adequate. Measurements with an oxygen ion beam showed that the emittance was as low as with the prototype microwave ion source. The permanent magnet plasma generator was installed on one of the TASCC ion source decks along with a potassium charge exchange canal, and beams of He^- and O^- were accelerated.

For details, refer to the progress report PR-TASCC-7, AECL-11028.

1.4 PUBLICATIONS AND LECTURES

Publications

AN ADVANCED HIGH-CURRENT LOW-EMITTANCE DC MICROWAVE PROTON SOURCE
T. Taylor and J.F. Mouris
Nuclear Instruments and Methods in Physics Research **A 336** (1993) 1-5.

MICROWAVE PROCESSING OF SIMULATED NUCLEAR WASTE CLASS II
R.L. Schulz, D.E. Clark, R.M. Hutcheon and G.G. Wicks
Ceramic Transactions, Microwaves: Theory and Application in Materials Processing II, **36**, 89 (1993).

REMOVAL OF POLYMETHYL METHACRYLATE BINDER FROM ALUMINA USING CONVENTIONAL AND/OR MICROWAVE HEATING
E.H. Moore, D.E. Clark and R.M. Hutcheon
Ceramic Transactions, Microwaves: Theory and Application in Materials Processing II, **36**, 325 (1993).

SURFACE MODIFICATION OF SODIUM ALUMINOSILICATE GLASSES USING MICROWAVE ENERGY II
Z. Fathi, D.C. Folz, D.E. Clark, and R.M. Hutcheon
Ceramic Transactions, Microwaves: Theory and Application in Materials Processing II, **36**, 333 (1993).

THE HIGH-TEMPERATURE MICROWAVE RESPONSE OF INDUSTRIAL FERRITES
R.M. Hutcheon, G.F. Morin, B.H. Smith, M.S. de Jong and F.P. Adams
Ceramic Transactions, Microwaves: Theory and Application in Materials Processing II, **36**, 469 (1993).

ELEVATED TEMPERATURE DIELECTRIC PROPERTY MEASUREMENTS: RESULTS OF A PARALLEL MEASUREMENT PROGRAMME
M. Arai, J.G.P. Binner, A.L. Bowden, T.E. Cross, N.G. Evans, M.G. Hamlyn, R.M. Hutcheon, G.F. Morin and B.H. Smith
Ceramic Transactions, Microwaves: Theory and Application in Materials Processing II, **36**, 539 (1993).

DESIGN OF A TUNER AND ADJUSTABLE RF COUPLER FOR A CW 2856 MHz RF CAVITY

M.S. de Jong, F.P. Adams, R.J. Burton, R.M. Hutcheon, T. Tran-Ngoc, A. Zolfaghari and P.T. Demos
Proceedings of the 1993 Particle Accelerator Conference, **2** (1993) 829.

A 2856 MHz RF CAVITY FOR THE MIT-BATES SOUTH HALL RING
M.S. de Jong, F.P. Adams, R.J. Burton, R.M. Hutcheon, T. Tran-Ngoc, A. Zolfaghari and P.T. Demos
Proceedings of the 1993 Particle Accelerator Conference, **2** (1993) 832.

CAVITY RF MODE ANALYSIS USING A BOUNDARY-INTEGRAL METHOD
M.S. de Jong and F.P. Adams
Proceedings of the 1993 Particle Accelerator Conference, **2** (1993) 835.

DESIGN OF A HIGH-POWER TEST MODEL OF THE PEP-II RF CAVITY
H.D. Schwarz, R.A. Bell, J.A. Hodgson, J.G. Judkins, K. Ko, N. Kroll, C.K. Ng, R.P. Pendleton, K. Skarpaas, G. Lambertson, R. Rimmer, M.S. de Jong, T. Tran-Ngoc, F.P. Adams M.G. Lipsett and W. Mellors
Proceedings of the 1993 Particle Accelerator Conference, **2** (1993) 1039.

OPERATION OF A HIGH-POWER CW KLYSTRODE WITH THE RFQ1 FACILITY
J.Y. Sheikh, A.D. Davidson, G.E. McMichael, L.W. Shankland and B.H. Smith
Proceedings of the 1993 Particle Accelerator Conference, **2** (1993) 1175.

A BOUNDARY-INTEGRAL-METHOD CODE FOR CAVITY RF MODE ANALYSIS
F.P. Adams and M.S. de Jong
AIP Conference Proceedings 297 of the Computational Accelerator Physics Conference, 43 (1994).

Conference Presentations

APPLICATIONS OF MICROWAVE ENERGY FOR WASTE REMEDIATION
R.L. Schulz, D.C. Folz, D.L. Clark, R.M. Hutcheon and G.G. Wicks
Paper presented at the 28th Int. Microwave Symposium and ISMI Section, Montreal, Canada, 1993 July 11-14.

Lectures

POTENTIAL AECL CONTRIBUTIONS TO A CANADIAN SYNCHROTRON LIGHT SOURCE
N.A. Ebrahim
Presented to Synchrotron Light Sources Subcommittee, NSERC Ad-hoc Committee on Materials Research Facilities, Ottawa, 1993 October 6-8.

SECTION 2

NEUTRON AND CONDENSED MATTER SCIENCE BRANCH

Edited by S.M. Kim

CONTENTS

2.1 NEUTRON AND CONDENSED MATTER SCIENCE BRANCH STAFF LIST

BRANCH MANAGER: B.M. Powell

Professional Staff

W.J.L. Buyers (1)
M. Couture
M.T. Dove(2)
E.D. Earle
J.D. Hepburn(3)
T.M. Holden
T.C. Hsu(4)
S.M. Kim
P.H.C. Lee(5)
M.A. Lone
F.J. Marsiglio
C.P. Martel(6)
R.B. Rogge(7)
J.H. Root
V.F. Sears
B. Sur(4)
E.C. Svensson
I.P. Swainson(8)
D.R. Taylor(9)
Z. Tun

Technical Staff

J.J.P. Bolduc
R.J.E. Deal
D.A. Doering
R.L. Donaberger(10)
J.H. Fox
E.R. Gaudette
M.D. Gauthier
L.E. McEwan
M.W. Montaigne
P.A. Moss
H.F. Nieman
M.M. Potter
J.A. Rollings (11)
G.A. Sims
H.C. Spenceley
D.C. Tennant

Secretarial Staff

J.S. Hill

(1) Sabbatical Leave, University of British Columbia, 1993 September-1994 September.
(2) Visiting Scientist, Cambridge University, Departed 1993 August 26.
(3) On attachment to SNO Project at Laurentian University, Sudbury.
(4) Research Associate.
(5) Terminated, 1993 November 30.
(6) Terminated, 1993 July 30.
(7) Joined NCMS Branch, 1993 October 1.
(8) Research Associate, jointly with University of Guelph.
(9) Visiting Scientist, Queen's University, 1993 September-1994 September.
(10) NSERC Technician with McMaster University attached to NCMS Branch.
(11) Joined NCMS Branch, 1993 August 16.

Visiting Scientists

O. Binbrek	University of Waterloo
E. Bonvin	Queen's University
J. Bouillot	Université de Savoie-France
D. Boyd	Queen's University
R.W. Cochrane	University of Montreal
M.F. Collins	McMaster University
R.A. Cowley	Oxford University
K. Elder	McGill University
P. Gangli	McGill University
B.D. Gaulin	McMaster University
M. Hamel	Université du Québec à Chicoutimi
C. Hargroves	Carleton University
M.J. Harris	Oxford University
M. Hayashi	Hitachi Limited
A. Hullin	Queen's University
T. Köppel	Mettler - Toledo, Switzerland
H. Lee	Queen's University
R. Lin	Studsvik Neutron Research Laboratory
A. Lodini	Laboratoire Léon Brillouin, Saclay
S. MacEwen	Alcan - Research and Development, Kingston
T.E. Mason	Toronto University
D. McMorrow	Oxford University
G. Mills	Salford University
M. Moorhead	Oxford University
D.G. Morris	Université de Neuchâtel
B. Mroz	A. Mickiewicz University
E. Norman	Lawrence Berkeley Laboratory
R.C. Peterson	Queen's University
D. Robson	Los Alamos National Laboratory
J. Schröder	GKSS Research Centre
M. Steinitz	St. Francis Xavier University
M. Sutton	McGill University
P. Swaddling	Oxford University
Y. Teisseyre	Université de Savoie-France
D.A.Tindall	Dalhousie University
B.H. Torrie	University of Waterloo
P.J. Webster	Salford University

Graduate Students

H. Abuluwefa	Oxford University
M. Gharghouri	McMaster University
E. Guerin	Université de Reims
J.G. Lussier	McMaster University
R.L. Millard	Queen's University
P. Prado	University of New Brunswick
R. Pridmore	University of Waterloo
A. Schröder	McMaster University
J. Smith	University of Manitoba
N. Townley	Queen's University
M.A. Wells	University of British Columbia
P.A. Willis	Queen's University
Y. Xu	McGill University
M. Zinkin	Oxford University

2.2 SUMMARIES

Condensed Matter Science

Analysis of $S(Q, \omega)$ data from liquid ^4He near T_λ was completed (2.3.1.1). The experimental lineshapes are well described by the Mori-Zwanzig formalism and are dominated by the contribution from the extended sound modes. In the non-superfluid regime they exhibit behaviour similar to that of classical noble-gas fluids.

A model has been proposed to describe the interaction of the 5f magnetic moments with the conduction electrons in URu_2Si_2 (2.3.1.2). In one dimension it is found that a low moment phase exists over a wide range of parameter space. It is hoped that in three dimensions the model will provide an understanding of the anomalously low moments found in several heavy-fermion compounds.

Polarized neutron measurements have shown that the weak order parameter observed below 17.5 K in URu_2Si_2 must have spin dipole character (2.3.1.3).

The existence of an exotic, non-local order has been postulated for URu_2Si_2, and its signature would be a particular field dependence for a magnetic peak. A search in fields up to 8T has been made for this exotic order at (100) in URu_2Si_2 (2.3.1.4). The data does not support the theory for this compound.

High-resolution neutron measurements at the 17.5 K transition in URu_2Si_2 show that as T_N is approached the spin-wave energy collapses and the spin susceptibility diverges (2.3.1.5). This confirms that the order parameter is proportional to the magnetic dipole.

Polarized neutron measurements on thin films of Co-Re multilayers observe a gradual spin-flop transition in the antiferromagnetic state and rotation of the spin order from antiferro to ferro at fields greater than 0.3T (2.3.1.6). This demonstrates strong interlayer magnetic coupling.

The modified pyrochlore $CsNiCrF_6$ is available in single crystal form. Neutron measurements observe diffuse scattering that develops continuously below ~ 30 K (2.3.1.7). A strong diffuse peak appears at $Q \sim 1.1$ Å^{-1} with weaker peaks at larger wave vectors. The data are compared with a simple model calculation and the agreement suggests the existence of very short-range correlations.

Powder diffraction measurements have been made on D_2O ice samples grown in large electric fields (2.3.1.8). The electric fields are found to have small but significant effects on the unit cell volume and the thermal parameters of the deuterium atoms.

Powder diffraction measurements were made for the Li-silicates $Li_2Si_2O_5$, Li_2SiO_3 and Li_4SiO_4 (2.3.1.9). The structure of Li_2SiO_3 was found to agree with that suggested by previous models, but that of $Li_2Si_2O_5$ was found to be orthorhombic rather than monoclinic, as believed previously. The refinement of $Li_2Si_2O_5$ led to a very different structure from those suggested previously; all Li sites were located and their partial occupancies were determined.

Longitudinal and transverse acoustic phonon dispersion curves have been measured in diopside, a natural chain silicate (2.3.1.10). The data is being used to refine the interatomic potentials for this silicate, since its dynamics have proved particularly difficult to model.

The order/disorder phase transition in ND_4Cl was investigated by powder diffraction measurements with isotopically pure ^{14}N and ^{15}N samples (2.3.1.11). The two data sets are being jointly refined to provide detailed structural information.

The temperature dependence of the crystal structure of KNO_3 was investigated by powder diffraction measurements (2.3.1.12) around the reconstructive phase transition at 397 K. The refinements show that, as for $CaCO_3$, the out-of-plane librations of the NO_3 ion play a major role in the transition, but, in contrast to $CaCO_3$, the in-plane librations of the NO_3 ion are relatively small.

The nature of the phase transition in the antifluorite $(ND_4)_2\ PdCl_6$ has been investigated by powder diffraction measurements (2.3.1.13). The low temperature phase was found to be monoclinic (space group C2/c), but the unexpected feature of the transition is that motion of the ND_4 ions dominates. They are found to rotate by ~ 45° relative to their orientation in the cubic phase.

Room temperature powder diffraction data were collected for the synthetic spinel $MgGa_2O_4$ and with 10%, 20% and 25% Mg_2GeO_4 as well as for $Mg_3Ga_2GeO_8$ (2.3.1.14). The lattice parameter was found to increase with Ge fraction, while the inversion parameter of $MgGa_2O_4$ was found to be larger than suggested by previous measurements.

The ferroelastic transition at 334 K in $K_3Na(SeO_4)_2$ has been investigated by powder diffraction measurements (2.3.1.15). The data suggests that the low temperature phase is monoclinic, while the high temperature phase must be a relatively simple structure, still undetermined.

Atomic ordering in titanium trialuminide alloys was investigated by powder diffraction methods at temperatures up to 1200°C (2.3.1.16). It was found that for some of the alloys the long range order on the Ti sublattice remains almost perfect, but for others the sublattice becomes increasingly disordered as the temperature increases.

Site ordering in the intermetallic alloys Al_3Ti-X (X = Ag, Fe, Ni, Mn) was investigated by powder diffraction methods (2.3.1.17). Preliminary analysis shows that for X = Fe and Ag the Ti sublattice is fully occupied by Ti atoms.

Crystallographic texture and interphase residual stresses were determined in an aluminum 2014 alloy reinforced by 20% SiC particulate (2.3.1.18). The texture is found to be generally weak. The SiC particles are found to be in compression while the Al matrix is in tension for extruded samples.

The plastic zone ahead of a fatigue crack was mapped out by neutron diffraction measurements (2.3.1.19). Compressive residual strains were found at the crack tip, becoming tensile ~ 3 - 4 mm from the tip. It was found, unexpectedly, that fatigue pre-cracking in the absence of load produces changes in the experimental linewidth.

The aberrations arising in near-surface measurements of strain were systematically investigated (2.3.1.20). Test measurements were made of the near surface strains in a heavily peened sample of Waspaloy.

The residual stress field introduced by shot peening and overloading U-shaped fatigue samples of aluminum AA7050-T73651 were measured by neutron diffraction (2.3.1.21). It appears that compressive stresses induced by the shot peening procedure were relaxed by the plastic deformation arising from overloading.

The residual stresses present prior to deformation in a binary Mg-Al alloy containing a hard second phase were measured by neutron diffraction (2.3.1.22). No stresses were found in pure Mg (a reference material) whether quenched, air-cooled or furnace-cooled and no stresses were present in the alloy as a result of a precipitation reaction.

Texture measurements were made on an AA5182 aluminum alloy to assess the effect of hot rolling variables on the as-deformed texture (2.3.1.23). It was found that, as total strain increased, the strength of the as-deformed texture also increased.

The textures of the α, β and hydride phases were measured in a specimen from pressure tube #R766 (2.3.1.24). The β-phase was found to exhibit a typical bcc rolling texture while the hydride texture corresponds to that of the α-phase. Analysis of the interface mis-orientations is in progress.

Residual stresses were measured in the ferrite phase (with a minority cementite phase) of mild steel as part of a program to understand plastic deformation in multi-phase materials (2.3.1.25). It was found that compressive microstresses in the ferrite phase are balanced by tensile stresses in the cementite phase.

A program has been written to calculate the multiphonon expansion of the incoherent scattering function in terms of a model for the velocity spectrum (2.3.1.26). It has been used to complete the analysis of data on crystalline and amorphous ice (2.3.1.27). The results confirm the earlier findings of excess intensity in $g(\nu)$ at ~ 0.6 THz and 11 K for the amorphous phase relative to that for the crystalline phase.

The Eliashberg equations have been solved for a model with retarded interactions and electron-hole asymmetry (2.3.1.28). Both effects are found to increase the superconducting transition temperature.

A new type of interaction has been included in the Hamiltonian for the generalized Eliashberg equations (2.3.1.29). The new term, an ion-modified Hubbard interaction, is found to result in corrections to the standard theory, but not to qualitatively different physics.

A general purpose program has been written that will determine the Hamiltonian for a many fermion system in two dimensions and diagonalize it to obtain exact eigenvalues for small systems (2.3.1.30). It will be used as a benchmark for approximate treatments such as BCS theory and T-matrix theory.

A theory for the conductivity of vortex cores in type II superconductors was developed (2.3.1.31). The theory is consistent with the observed cyclotron resonance and small chiral response.

Three approaches were taken to identify xz-polarized modes in ABX_3 stacked antiferromagnetic chain systems (2.3.1.32). The spin wave spectrum with single-ion anisotropy was calculated analytically; the spin structure factor was calculated, including magnon-magnon interactions; and a local field approach was used. Recent data is being analyzed in terms of these three theoretical approaches.

It has been suggested that multiple scattering effects or wavelength dependent attenuation might be responsible for small inconsistencies observed in measurements of residual strain in steel plates (2.3.1.33). A test experiment showed that multiple scattering effects are insignificant, but calculations of the wavelength dependent attenuation suggests this might be significant.

Neutrino Physics

Quality control of 150 acrylic sheets for the SNO detector has been performed (2.3.2.1). The Th and U content were significantly better than specifications. Fabrication procedures are now being tested to determine whether they degrade the quality of the sheets. The neutron activation analyses and γ-counting techniques used for the acrylic are now being used to test other materials (2.3.2.2).

A silicon diode cryotrap for radon detection has been designed, fabricated and tested (2.3.2.3). The cryotrap was selected as the primary device for Th assay of the D_2O in the SNO detector. It is expected to have a sensitivity of 10^{-16} g/g equivalent Th.

A calibration scheme for the photomultiplier tubes has been proposed for the SNO detector in which short-lived sources are produced by 14 MeV neutron irradiation of an appropriate target (2.3.2.4). The activity is then transported rapidly to a decay chamber in the D_2O by a fast gas transport system. The short-lived nuclei ^{16}N, ^{8}Li and ^{17}N are under test as possible calibration sources.

The CRL-SNO group continues to perform a variety of tasks that can be done most efficiently at CRL (2.3.2.5). Procedures for the transfer of D_2O and increased responsibility for the water systems are two such tasks.

At the SNO site, construction work to convert the laboratory and detector excavations underground into usable space is ~ 80% complete (2.3.2.6). Off-site progress continues and the geodesic support structure for the photomultipliers was test assembled and delivered to the Sudbury site. Delivery of the photomultiplier tube assemblies to Sudbury is on schedule. An additional $15.4M in funding was approved for completion of the project. The surface assembly building was declared in service (2.3.2.7) and service water, electrical and HVAC systems are operational. Cleaning procedures are being tested by establishing a clean room for ducting assembly prior to installation.

Nuclear Data and Modelling

Self-powered detectors are passive devices used to monitor neutron and gamma fields. Their responses to electrons and gamma-rays were investigated by Monte Carlo simulations (2.3.3.1). Filters were studied for the design of such detectors for on-line monitoring of electron accelerators and to investigate the enhancement of their gamma-ray sensitivity in a mixed electron and gamma-ray field. The calculations were compared with experimental data measured with ^{60}Co and ^{192}Ir gamma-rays (2.3.3.2). Good agreement was found between the measurements and the simulations.

As a test of the deterministic codes used for radiation shielding analysis for space missions, results from these codes were compared with those from Monte Carlo calculations (2.3.3.3). Comparison of the predictions for thick water targets suggests that discrepancies exist.

Monte Carlo calculations of the energy spectra of secondary protons and neutrons were used to analyze data from bubble detectors flown in three space missions (2.3.3.4).

In a study of the Iterated Prisoner's Dilemma problem it was found that multiple strategy communities could be sustained indefinitely (2.3.3.5).

Instrumentation

The higher order contamination in spin polarized beams was investigated by chopper measurements at the polarized beam triple-axis spectrometer (2.3.4.1). A small furnace has been developed to fit on the Eulerian cradle and thus be oriented under computer control (2.3.4.2). A new high-precision, slit system was fabricated for use in near-surface strain measurements and the precision of sample positioning was significantly improved (2.3.4.3). Modifications were made to the sample tables to ensure that their angular positions are retained when the coupling clutch is disengaged (2.3.4.4). A rapidly installable shelf was designed and fabricated to allow easier extraction and installation of beam channel components for DUALSPEC (2.3.4.5).

Modifications were made to the DUALSPEC gates to introduce an interlock switch and easier fault diagnosis (2.3.4.6). A high speed drive has been installed on the η-axis of the Eulerian cradle. This has increased its throughput for texture measurements by a factor of ~ 3 (2.3.4.7). A remote hand-held control has been installed at DUALSPEC to drive any motor on the spectrometer. The control has an alphanumeric display that shows the drive name, current position, acceleration time, motor speed and any off-limit conditions.

Support Services

A prototype grounded anode multiwire detector with 4 mm wire spacing was completed and put into service with the ANDI group. Its performance has been so good that a production model to meet the ANDI specifications is under construction. This will have 32 active wires with 2 mm separation (2.3.5.1). A second pumping/filling station has been put into operation (2.3.5.4) and a new cryopump has been installed (2.3.5.5).

A prototype silicon diode cryotrap for ultra-sensitive radon detection was fabricated for the SNO group. It proved to be so successful that this design has been selected by the SNO collaboration (2.3.5.7) for Th chain assay of the D_2O. A miniature furnace was fabricated to fit on the Eulerian cradle and a special, hostile environment enclosure was made for a standard furnace. Movement limiters were installed on two focussing monochromators.

Glass connectors and traps were fabricated for an IAEA contract to Romania (2.3.5.8). A further prototype for demonstration of a passive reactor safety system was constructed. Quartz furnace tubes were fabricated to fulfil a contract with SRB Technologies.

2.3 INDIVIDUAL REPORTS

2.3.1 Condensed Matter Science

Physics

2.3.1.1 Sound Modes in Non-Superfluid ^{4}He

E.C. Svensson with W. Montfrooij (Risø National Laboratory)

In the last period we reported (PR-PHY-6:2.3.1.1; AECL-10878) the results of an analysis of the roton excitations in liquid ^{4}He at temperatures close to the superfluid transition temperature, T_λ, based on the Mori-Zwanzig (MZ) projection formalism. This formalism states that the relaxation function

$$S_{sym}(q,\nu) = \frac{1-\exp(-\beta h\nu)}{\beta h\nu} S(q,\nu) \qquad (1)$$

can always be described by a sum of Lorentzian lines, commonly referred to as the eigenmodes of the fluid. Thus, the fluid can be viewed as a gigantic macromolecule with only a few available modes of response to a disturbance, such as being struck by a neutron. Of particular importance are the so-called extended sound modes (frequencies $\pm\nu_s$) which are the continuous extension in q of the hydrodynamic sound waves.

We have now completed an analysis in terms of the MZ formalism of neutron scattering results for non-superfluid ^{4}He at several temperature and pressure values: (4.2 K, SVP = saturated vapour pressure), (4.2 K, 20 bar), (4.2 K, 25 bar), (2.35 K, 16.7 bar) and (2.3 K, SVP). As was the case for our previous analysis of rotons near T_λ, we find that in all cases the experimental line shapes are very well described by the MZ formalism. With one exception, the contribution from the extended sound modes is totally dominant. The exception occurs in the low-q region for the (4.2 K, SVP) data set (A.D.B. Woods, E.C. Svensson and P. Martel, Can. J. Phys. **56** (1978), 302) where the extended heat mode (diffusive heat transport mechanism) makes a significant contribution.

As an example of the results we have obtained, we show in Fig. 2.3.1.1 the dispersion relation for the extended sound modes for the (4.2 K, SVP) data set. At very low q, the dispersion is given by the first-sound velocity (solid curve). The upward deviation in the region $0.3 \leq q \leq 1.0$ Å^{-1} is caused by "mode coupling" effects which are particularly large for (4.2 K, SVP). For the other four data sets, these mode coupling effects, and hence the deviation from the velocity-of-sound line in the region $q \leq 1.0$ Å^{-1}, are much smaller. In the region $q \lesssim 2$ Å^{-1} (i.e., in the region of the main peak of the static structure factor, S(q), and the roton minimum in superfluid ^{4}He) a

"propagation gap" appears in the dispersion relation for the extended sound modes, for all data sets. This is because, in this region, the damping rate of the momentum fluctuations (which is the only free parameter in our analysis and completely determines the dispersion) has become so large that propagating waves can no longer be sustained by the fluid.

Our analysis shows that the extended sound modes in low temperature ($T \leq 4.2$ K) non-superfluid ^{4}He exhibit behaviour very similar to that observed for "classical" noble-gas fluids. In one respect, however, non-superfluid ^{4}He is quite different. Namely, the extended sound modes dominate the neutron scattering spectra to a far greater extent than has yet been observed for "classical" fluids (such as liquid Ne and Ar, and even dense ^{4}He gas at temperatures ≥ 25 K) where the extended heat mode normally dominates the scattering for essentially all q values.

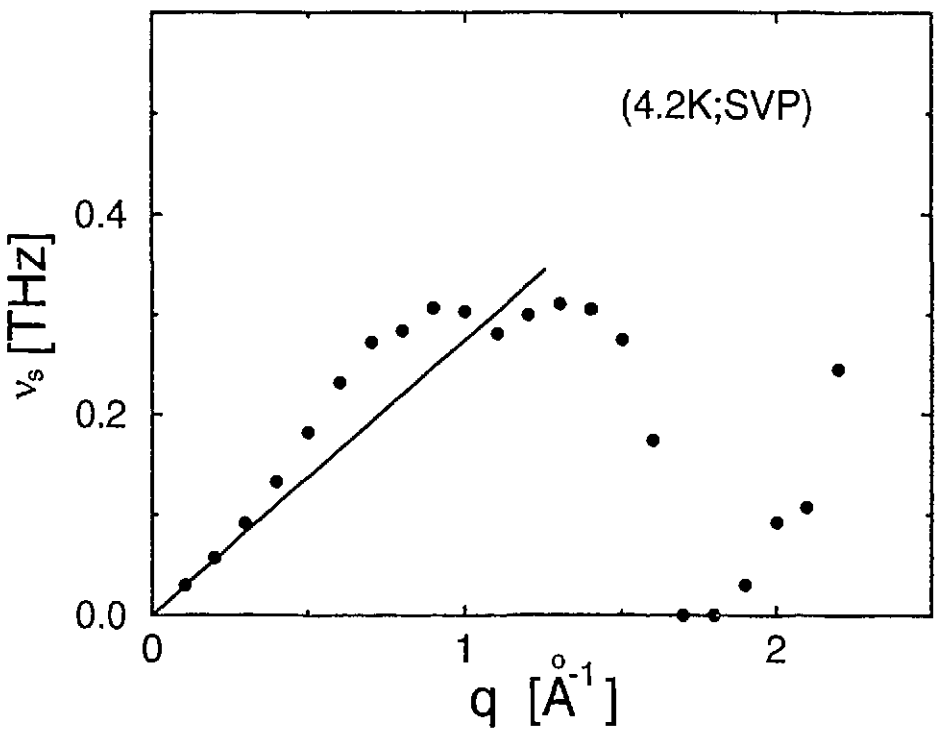

Fig. 2.3.1.1 Dispersion relation for the extended sound modes in non-superfluid ^{4}He at 4.2 K and SVP obtained by analysis of neutron scattering results in terms of the Mori-Zwanzig projection formalism (see text). The solid curve shows the velocity of first sound.

2.3.1.2 Low Magnetic Moments in Heavy-Fermion Systems

W.J.L. Buyers with A. Sikkema, J. Gan and I. Affleck (University of British Columbia)

A model to describe 5f magnetic moments interacting with conduction electrons has been studied for the case of the anisotropic compound URu_2Si_2. The resultant Kondo model has on-site exchange between f and conduction electrons, while the f crystal field splitting acts as a transverse field opposing ordering. Mean-field analytical and self-consistent computer calculations in one dimension have shown that a low moment phase exists over a wide range of parameter space. By contrast, f spins interacting with a fixed interionic exchange coupling can only have a low induced moment for a fortuitously small range of exchange to crystal field splitting. The new Kondo model shows logarithmic behaviour and a broken spin symmetry for any ratio of the onsite to the f splitting and to the conduction electron bandwidth. These results are consistent with an earlier idea coming from neutron scattering results that the effective f-f exchange through the electrons in fact decreases as the moment switches on below the phase transition. It is hoped that for three dimensions the model will provide a new basis for understanding the origin of the anomalously low moments observed in several heavy-fermion compounds.

2.3.1.3 The Nature of the Order Parameter in the Heavy-Fermion System URu_2Si_2

W.J.L. Buyers and Z. Tun, with M.B. Walker and W. Que (University of Toronto), A.A. Menovsky (University of Amsterdam) and J.D. Garrett (McMaster University)

The weak order parameter observed below the 17.5 K transition in URu_2Si_2 has been variously attributed to magnetic dipoles, quadrupoles or octupoles. By polarized neutron scattering we have shown that the order parameter breaks time reversal invariance and so cannot be quadrupolar or a spin nematic. Of the five dipolar and octupolar order parameters that are then allowed by symmetry, polarization analysis reveals that only the spin dipole, M_z, orders at the transition.

2.3.1.4 Search for Exotic Spin Order in a Low-Moment Heavy-Fermion Superconductor

W.J.L. Buyers with T.E. Mason (University of Toronto) and J.D. Garrett (McMaster University)

V. Barzykin and L.P. Gor'kov have advanced the theoretical possibility that the anomalous low magnetic moment seen at low field in URu_2Si_2 is not the true order parameter, but that an exotic non-local but strong order exists that could not be

observed in previous neutron scattering experiments. One of these exotic states is a triple-spin correlator in which spins at three different sites may order, while the average spin at any one site remains zero. They predict that by applying a large field, a magnetic peak would appear whose intensity would increase with field, H, as $(H/H_0)^4$ with $H_0 \sim 10$ Tesla.

We have searched in fields up to 8 Tesla for such exotic order at (100) in URu_2Si_2 from 4 K to 25 K (T_N = 17.5 K). In contrast to the theory the magnetic neutron scattering intensity is observed to *decrease* with field. The power law is $I = M^2 = M_0^2\,[1 - (H/H_0)^{1.5}]$ with H_0 = 14 Tesla. This behaviour is consistent with a simple picture in which the field drives down the magnetization of the eight antiparallel nearest neighbours faster than it enhances the parallel magnetization of the central uranium atom in this induced moment system.

We conclude that the theory of exotic spin ground states does apply to this particular material with its large crystalline (Ising) anisotropy. The theoretical predictions are valid only when interatomic exchange is the only interaction of importance and that is certainly not the case for most heavy-fermion crystals.

2.3.1.5 Spin-Wave Collapse and Incommensurate Fluctuations in URu_2Si_2

W.J.L. Buyers and Z. Tun, with T. Petersen and T.E. Mason (Risø National Laboratory), J.-G. Lussier and B.D. Gaulin (McMaster University) and A.A. Menovsky (University of Amsterdam)

We performed high-resolution neutron scattering using the cold neutron source at Risø in Denmark to test whether the 17.5 K transition in URu_2Si_2 is driven by a divergence of a magnetic order parameter. At the ordering wave vector, as T_N was approached, the spin-wave energy collapsed and the spin susceptibility diverged. This confirms that the order parameter is proportional to the magnetic dipole as shown by recent symmetry arguments and polarized neutron scattering. We also observe incommensurate fluctuations above T_N, suggesting that competing temperature-dependent interactions may influence this weak-moment transition.

2.3.1.6 Observation and Switching of the Antiferromagnetic Order in a Multilayer Exhibiting Giant Magnetoresistance

W.J.L. Buyers, I. Swainson and Z. Tun, with M. Sutton (McGill University) and R.W. Cochrane (Université de Montréal)

The recently discovered phenomenon of giant magnetoresistance is expected to lead to major applications for switching in the electronics industry. When a magnetic field is applied to a synthetic structure formed by MBE (Molecular-Beam-Epitaxy) or CVD (Chemical Vapor Deposition) techniques in which non-magnetic layers alternate with

magnetic layers (typically 10-50 Å thick), the resistance of the thin film composite is found to decrease by as much as a factor of two. This is much greater than the magnetoresistance of normal metallic alloys where the change is only a few percent. The large resistance at zero field arises because conduction electrons are scattered by the disorder produced by antiferromagnetically oriented adjacent magnetic layers. When a field is applied the layers are forced to align ferromagnetically, thus eliminating the magnetic disorder and lowering the resistance.

Neutron scattering is an ideal way to see inside these atomically thin layers and probe their magnetic arrangement. We have observed a gradual spin-flop transition in the antiferromagnetic state and gradual rotation of the spin order from antiferro to ferro at fields higher than 0.3 Tesla in a thin film of Co-Re multilayers $Re_{50}[Co_{24}/Re_6]_{50}Re_{10}$. Polarized neutrons were used for this experiment and glancing-angle measurements down to scattering angles of 0.1° were performed. The results demonstrate a strong interlayer magnetic coupling and are qualitatively similar to the behaviour recently reported for the Co-Cu system (A. Schreyer, et al., Phys. Rev. **B47** (1993), 15334). This similarity in the magnetic coupling of the two systems contrasts with the large differences in their magnetoresistances, and indicates that they provide a good testing ground for the theories of giant magnetoresistance.

2.3.1.7 The Short-Range Magnetic Structure of Frustrated Pyrochlore $CsNiCrF_6$

Z. Tun and I.P. Swainson, with M.J. Harris, M.P. Zinkin and B.M. Wanklyn (Oxford University)

A great deal of interest has developed in materials containing antiferromagnetically coupled magnetic moments which are geometrically frustrated, so that in principle there are many possible ground states. Examples include two-dimensional systems such as corner-shared triangular lattices and Kagomé lattices (a network of corner-shared hexagons). In three dimensions the frustration may occur if the magnetic ions occupy the corners of corner-shared tetrahedra. This is the situation realised in the pyrochlore structure.

Several transition metal fluorides with the general formula $CsX^{2+}Y^{3+}F_6$ (where X=Fe,Ni,Mn; Y=Fe,Cr,V) crystallise in a modified form of the pyrochlore structure with space group Fd3m. The magnetic X^{2+} and Y^{3+} ions are randomly distributed at the corners of the tetrahedral framework. Neutron scattering studies of these compounds (W. Kurtz et al., Solid State Comm. **18** (1976), 1479; L. Bevaart et al., Phys. Rev. **B26** (1982), 6150) have shown the presence of a large amount of diffuse magnetic scattering, revealing the presence of strong antiferromagnetic (AFM) short-range order. A similar phenomenon has been observed in another pyrochlore $Tb_2Mo_2O_7$ (Gaulin et al., Phys. Rev. Lett. **69** (1992), 3244). However, all these neutron scattering studies were carried out with powder samples.

$CsNiCrF_6$ is a modified pyrochlore that contains strong AFM interactions, and presumably a frustrated ground state. Unlike the previously studied materials, it is available in single crystal form. Two experiments have been performed at Chalk River which confirm the presence of the characteristic diffuse magnetic scattering in a single crystal of $CsNiCrF_6$. The measurements were performed on the C5 and E3 spectrometers, both in the two-axis configuration with a pyrolytic graphite (002) monochromator providing neutrons with wavelength $\lambda = 2.37$ Å. A PG filter was placed in the scattered beam to suppress higher-order $\lambda/2$ and $\lambda/3$ neutrons, and the sample was cooled with the M3 cryostat on C5 and a CTI closed-cycle refrigerator on E3. The measurements on C5 provided a rough temperature dependence of diffuse scattering, while those on E3 allowed a more detailed study.

The diffuse scattering that developed continuously below 30 K was determined by subtracting the observed intensities at ≥ 60 K from the intensities at 12 K and adding a constant to ensure that the difference is zero at $Q = 0$. Fig. 2.3.1.2 shows the net diffuse intensity in three radial scans close to symmetry directions (but carefully avoiding Bragg peaks). All the scans contain a strong peak of diffuse scattering at ~ 1.1 $Å^{-1}$, together with weaker peaks at larger wave vectors. This feature, observed for the first time with a single crystal of this geometrically frustrated material, is the most significant result. It allows a direct comparison between the theoretical calculations of the scattering function S(Q) and experimental data.

The simulated scattering cross section from a single tetrahedron has been compared to the experimental data. The simulation was performed by calculating S(Q) of a model containing a single tetrahedron, and by adjusting the spin configuration and the scale factor to match the observed and calculated intensities (same scale factor for all three directions). The resultant S(Q) curves are shown in Fig. 2.3.1.2. For a simple model with very few adjustable parameters the agreement is remarkable, suggesting a very short-ranged correlation.

Molecular Physics

2.3.1.8 Structure of Ice Grown in an Electric Field

E.C. Svensson with M. Farzaneh and M. Hamel (Université du Québec à Chicoutimi), J. Bouillot and Y. Teisseyre (Université de Savoie) and R.L. Donaberger (McMaster University)

The DUALSPEC diffractometer has been used to carry out neutron powder diffraction measurements on D_2O ice samples grown in high electric fields and on a reference sample grown in zero field. The purpose of this study was to investigate possible effects on the structural parameters of ice caused by growth under conditions chosen to simulate those giving rise to the deposition of ice on high voltage cables used for electric power transmission.

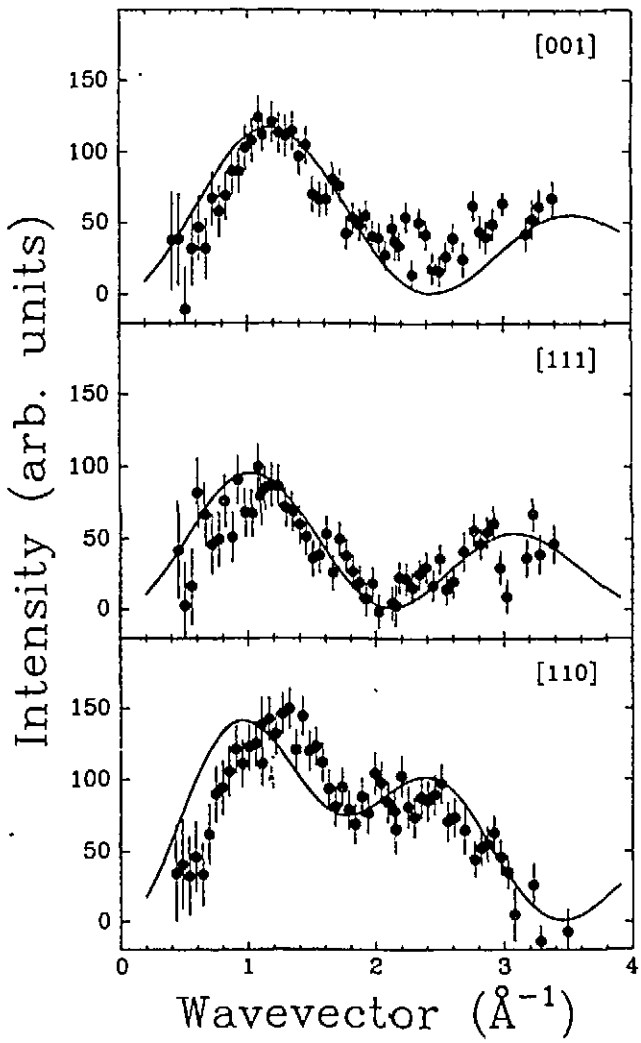

Fig. 2.3.1.2

The special ice samples were made in the "High Voltage Laboratory" of the Université du Québec à Chicoutimi by allowing high-purity D_2O vapour to freeze onto a conductor held at -12°C. Samples were made with the conductor subjected to voltages of + and - 5, 15 and 20 kV/cm and to zero applied voltage. The samples were "broken" from the conductor and crushed into coarse powders at -25°C, and then transported to Chalk River with their temperature being maintained in the range -10 to -30°C. At Chalk River they were cooled to liquid nitrogen temperature and ground into fine powders for the diffraction measurements which were carried out with the samples in thin-walled cylindrical vanadium cans of inner diameter 0.50 cm. Measurements were carried out at 225 K on four ice samples (0, +15, -15 and +20 kV/cm) and the empty cell using 1.5 Å neutrons [from a Si(531) monochromator at $2\theta_m = 110°$] and covering the range of scattering angles $5 \leq \emptyset \leq 120°$ in 0.05° steps. The samples were rotated continuously during the measurements and the total counting time for each sample was ~18 hours.

Preliminary Rietveld analysis of the diffraction profiles indicates that growing ice samples in a high electric field has small but significant effects on the unit cell volume and the parameters for the deuterium atoms, particularly the Debye-Waller (thermal) parameters. For example, changes between 0 and 15 kV/cm are about 10 times the estimated uncertainties. It is rather interesting that the sign of the change in the unit cell volume is opposite for -15 kV/cm (positive change) and +15 kV/cm (negative change) while the magnitude of the change (0.3%) is the same. More detailed analysis of the results is in progress and further measurements are planned.

2.3.1.9 The Structures of Li-silicates

I.P. Swainson and B.M. Powell, with M.T. Dove (Cambridge University)

The crystal structures of Li-silicates are the principal source of chemical information about Li-O coordination. The crystalline silicates are important, as they provide a basis for understanding the nature of Li-silicate glass, since it is known that many Li-glasses have radial distribution functions very similar to their crystalline counterparts. Previous lattice energy minimization calculations revealed a number of possible faults in the available crystallography. Many of the previous refinements were performed with X-rays. Li shares a similar problem to H for X-ray diffraction. It has only three electrons, so that the form factor is so small as to make the atom nearly invisible. Whilst the neutron scattering length of Li is also small, it is observable with neutrons, given sufficient counting time. Experiments were performed on powdered samples of $Li_2Si_2O_5$, Li_2SiO_3 and Li_4SiO_4 (all grown by the Department of Chemistry, University of Cambridge) at room temperature on the C2 DUALSPEC diffractometer.

The refined structure of Li_2SiO_3 (a chain silicate) was found to be in reasonable agreement with previous models. In contrast, a previous refinement of $Li_2Si_2O_5$ had found the structure to be monoclinic, whereas the lattice energy calculations had suggested an orthorhombic cell. Our experiment found that the structure refined better as an orthorhombic cell than as a monoclinic structure. The most interesting information appears to be on the island silicate Li_4SiO_4, in which the SiO_4 tetrahedra are unlinked. Two previous refinements had given radically different suggestions for the structure. Tranqui et al. (Acta Cryst B35 (1979), 2479) had proposed a large-scale superstructure, which the lattice energy calculations suggested had some or all of the Li atoms in the wrong positions. The Rietveld refinements showed that this structure was clearly incorrect. A much better model was achieved using the older model of Völlenkle et al. (Monat. Chemie 99 (1968), 1360). However, whilst the cell is much smaller, it still calls for partial occupancy of Li sites. These occupancies had been determined from the X-ray studies on the basis of very weak residual electron densities in different syntheses. The occupancies of the first three atoms had been assigned as 2/3, 1/2, 1/2, (to be simple fractions of integers) but those of atoms 4-6 were not determined by the X-ray data and had been set to 1/3 to maintain the stoichiometry. The data from C2 suggested a new ordering scheme for atoms with a

lower χ^2 for the fit and in which all the *R*-factors were smaller than a model using the originally suggested occupancies. Atoms 1-6 were assigned occupancies of 1/2, 2/3, 1/3, 1/2, 1/6, 2/3. This new model did not require that the partial occupancies be easily expressible fractions, although the fact that they came out to be so gives us some confidence in the refinement. The successful location of Li atoms in these artificial Li-silicates using neutron powder diffraction has prompted us to study the natural chain silicate spodumene $LiAlSiO_6$. This material, aside from being a natural Li-silicate, has unusually small thermal expansion, and glasses of its composition are proposed as future materials for fusion reactors.

2.3.1.10 Low-frequency Dispersion Relations in Diopside, $Mg_2Si_2O_6$ -- a Natural Chain Silicate

I.P. Swainson with M.T. Dove (Cambridge University)

Diopside represents a whole class of chain silicates, called the pyroxenes, which make up a large portion of both the continental and oceanic crust as well as the upper mantle. As interatomic potentials have become available, there have been many attempts to model the lattice energies and dynamics of minerals with the ultimate goal of trying to predict their behaviour under geologically realistic temperatures and pressures. A new generation of quantum-mechanically based potentials are being developed for silicates and it is essential that better data become available. Diopside has proved particularly difficult to model with existing potentials despite its relative simplicity. This is in part because of the lack of data. A large natural single crystal of diopside (approximately 7 cm^3) originating from Pierre Point, New York, was used to measure phonon dispersion curves. Relatively few measurements have been made on any natural materials and most have concentrated on relatively simple materials such as quartz, which has been extensively studied. The unit cell of diopside is monoclinic and the material has approximately 60 phonon branches. Even this structure is relatively simple compared to many mineral systems. Because of the great complexity of the dispersion relations, it was decided to measure only low-frequency modes. This was done for all three sections, a^*-c^*, b^*-c^* and a^*-b^*, to try to measure branches with different possible polarizations.

The measured longitudinal and transverse acoustic modes should substantially improve upon the early Brillouin scattering determinations of the elastic constants of diopside. In addition, several strong low-frequency optic modes were measured in each section. Work is underway to relate the measured dispersions to those calculated using existing potentials. The potential will then be refined using the observed data, so that other thermodynamic quantities can be calculated with reasonable certainty.

2.3.1.11 Orientational Order-Disorder Transition in ND_4Cl

I.P. Swainson with P. Willis and R.J.C. Brown (Queen's University) and R.L. Donaberger (McMaster University)

There has been little previous neutron diffraction data on the order-disorder transition in ND_4Cl, despite the fact that it is a well-known example of such a transition. Measurements were made in the disordered phase (Pm3m) above T_c at 260 and 290 K, and in the ordered phase (P43m) at three temperatures: 240, 200 and 5 K. Two isotopically-pure ^{14}N- and ^{15}N-samples had been prepared of powdered deuterated ammonium chloride, in order to make use of the different scattering lengths of the two N-isotopes (0.937 and 0.644 fm, respectively). The experiment was performed on the C2 DUALSPEC diffractometer and the data refined using the facility for joint refinement available in the GSAS Rietveld refinement code.

Both ^{14}N and ^{15}N data sets were refined simultaneously in a constrained refinement, so that the two sets of observations could be fitted to a single structural model, with an allowance made for the differing coherent scattering lengths, background parameters and profile parameters. The data at 5 K were used to extract an accurate N-D bond length of 1.030(1) Å. Despite the interest in order-disorder in ammonium compounds, few experiments have been performed on any deuterated ammonium compounds to accurately determine this bond length, so the present measurements supplied a much needed value for the literature. In the higher temperature refinements in which the disorder of the ND_4 ion begins to become important, this bond length was fixed so that more accurate information about the anisotropic temperature factors of the D-atom could be extracted.

Whilst the chief point of the experiment was not to extract order parameter information (only a few temperatures were measured), it was possible to determine the degree of disorder of the ND_4 ion. This experiment was designed largely as a test of the usefulness of joint isotope refinement methods. Because of its success, it is planned to perform further experiments on isotopically-pure deuterated ammonium compounds.

2.3.1.12 Phase Transitions in KNO_3

I.P. Swainson with M.T. Dove (Cambridge University)

KNO_3 is of interest as it possesses phases that are isomorphic to both of the two phases of $CaCO_3$ (aragonite and calcite), a compound which has been heavily studied at Chalk River and elsewhere recently. KNO_3 has the aragonite structure at room temperature, in which the K ions take up an approximately hexagonally close-packed arrangement, but at 397 K it transforms reconstructively into the disordered calcite structure, in which the K ions are approximately cubic close-packed and in which the

NO_3^- groups are rotated relative to the aragonite structure. This is important as the disordered calcite phase in $CaCO_3$ has never been observed experimentally, although measurements very close to the transition point have been made on the C2 DUALSPEC diffractometer so that the nature of the disordering process is at least known.

We obtained powder diffraction patterns at a number of temperatures from 300 K to 560 K and refined the structure at each temperature. The important information concerns the libration amplitude of the nitrate molecular ions on heating. The transition to the disordered calcite phase involves rotations about the molecular 3-fold axis. However, as in calcite, the largest thermal expansion of the cell is along the direction normal to the planes of the molecular ions. Our refinements showed that this is probably due to a large amplitude of out-of-plane libration of the trigonal NO_3^- ions (as in $CaCO_3$). However, in calcite the rotational disorder of the planar trigonal CO_3 ions in this plane is an even larger effect. In KNO_3 the in-plane librations are relatively small.

Calcite itself is at the extreme end of stability for its crystal structure in terms of cation radius and so is likely to show the most extreme effects. Recently the disordered phase of calcite has been successfully simulated using molecular dynamics (R. Lynden-Bell, Cambridge University). It is hoped that as the model of disorder of calcite is developed it will be possible to explain the difference in the disordering behaviour of these two compounds.

2.3.1.13 Phase Transitions in $(ND_4)_2PdCl_6$

I.P. Swainson and B.M. Powell, with R.M. Weir (Royal Military College)

The antifluorites have been extensively studied at Chalk River over the last ten years. The high-temperature antifluorite (R_2MX_6) structure is cubic, but undergoes a number of different structural transitions to tetragonal, orthorhombic and monoclinic cells, depending on many factors, including the size of the R-cation. When R is a metal cation (Na, K, etc.) the transitions are due almost solely to rotation of the octahedral MX_6 units in the structure. It was known from previous calorimetric measurements that $(ND_4)_2PdCl_6$ undergoes a first order transition at 30 K, but nothing was known about the low-temperature phase.

The structure was refined at room temperature (cubic form) and at 5 K using the GSAS Rietveld refinement code and using atomic temperature factors based on experimental data taken from C2. Both the ND_4 and MX_6 complexes were modelled as rigid units for both temperatures, and in the low-temperature phase were free to rotate. It was found that the low-temperature phase was monoclinic (C2/c). The most surprising features of the transition were that the MX_6 unit rotations are almost insignificant (about 2°), and that the orientation of the ND_4 ions is the most important

part of the transition mechanism, rotating approximately 45° relative to the cubic phase. It appears to be a steric effect, so that the D atoms of separate ND_4 molecules repel one another. It was also possible to show that the N-D vector points away from the MX_6 complex in both symmetrically distinct ND_4 molecules.

Previous refinements of ammonium antifluorites have not been able to model ammonium orientation, as they used a slightly different refinement method in which the temperature factor of the D-atom and its orientation could not be refined simultaneously, so that it is not clear whether this is unique to this composition or not. Another ammonium antifluorite that was examined, $(ND_4)_2PtCl_6$, proved to be impure, so the effect could not be tested. Work continues on the refinements of the related transitions in the largely unstudied compounds ND_4PF_6 and NH_4PF_6.

2.3.1.14 Cation Ordering in Synthetic $MgGa_2O_4$-Mg_2GeO_4 Solid Solution

I.P. Swainson with R. Millard and R. Petersen (Queen's University)

The spinels are an important group of structures with a wide variety of compositions allowing for a great deal of solid solution. Natural Si-spinels are important constituents of parts of the earth's mantle (but can only be stabilized under high pressure). The chemistry of Ge is sufficiently close to that of Si; however, it provides a low-pressure analogue of the Si-spinels. There is extensive solid-solution of Mg_2GeO_4 in $MgGa_2O_4$ spinel at high temperatures (up to 30 mole % Mg_2GeO_4 at 1400°C). Lienenweber and Navrotsky (Phys. Chem. Min. **16** (1989), 497) found an increase in the *a* cell edge with increased Mg_2GeO_4 component in Mg_2GaO_4 spinel, even though the Mg_2GeO_4 lattice is significantly smaller. They predicted that cation disorder across the Mg_2GaO_4-Mg_2GeO_4 solid solution would account for the observed cell edges. Also, at a 1:1 ratio of $MgGa_2O_4$ to Mg_2GeO_4, a spinelloid phase $Mg_3Ga_2GeO_8$ is stable, and is suggested to have extensive cation disorder (Barbier and Hyde, Phys. Chem. Min. **13** (1986), 382).

Room temperature neutron diffraction data were collected on the DUALSPEC powder diffractometer C2, for end-member $MgGa_2O_4$ and spinels of composition 10%, 20% and 25% Mg_2GeO_4, (quenched at 1400°C) as well as for spinelloid $Mg_3Ga_2GeO_8$ (50% Mg_2GeO_4). Rietveld structure refinements of the neutron data, using DBWS-9006, show the cell edge of our $MgGa_2O_4$-$Mg_2GeO_4$to vary from a = 8.2883(2) Å in end-member $MgGa_2O_4$ to a = 8.3059(1) Å at 25% Mg_2GeO_4. These values show the same trend as found by Lienenweber and Navrotsky (1989) but our values are systematically higher (they found a = 8.2817(4) Å and 8.2992(4) Å at 0% and 27% Mg_2GeO_4, respectively). Furthermore, our end-member $MgGa_2O_4$ had an inversion parameter of x = .90(3) (i.e., 90% of the tetrahedral site is occupied by Ga) giving it a more inverse cation distribution than that found in previous refinements.

The Mg and Ga cations rapidly disorder with addition of Ge (which remains essentially on the tetrahedral site), passing through a random distribution to become a disordered normal distribution within the limit of the solid-solution. At 25% Ge, the tetrahedral site contains 32% Ga (x = .32(2)), making this spinel slightly more normal than predicted by the cation distribution model of Lienenweber and Navrotsky (1989) (x = .38). Rietveld refinement of the spinelloid $Mg_3Ga_2GeO_8$ (50% Mg_2GeO_4) is underway, to allow comparison with the spinels.

2.3.1.15 Neutron Diffraction in Ferroelastic $K_3Na(SeO_4)_2$

S.M. Kim and B.M. Powell, with H. Kiefte (Memorial University of Newfoundland) and B. Mroz (A. Mickiewicz University)

Recently it has been discovered that the compound $K_3Na(SeO_4)_2$ undergoes a first order ferroelastic phase transition at 334 K. The anomalous thermal, dielectric, elastic and optical behaviour observed in this compound suggested that the ferroelastic phase 2/m is reached in two steps. On cooling through 346 K this crystal undergoes a continuous ferroic phase transition from $\bar{3}$m to 3 or 32 point group. At 334 K a further discontinuous ferroelastic phase transition to monoclinic 2/m takes place. At present, the only structural studies are the X-ray measurements obtained far from the transitions (290 K and 390 K).

We have carried out neutron powder diffraction measurements on $K_3Na(SeO_4)_2$ compound in order to observe the postulated structural phase transition at 346 K, and to determine the temperature dependence of the order parameter (monoclinic distortion) below 334 K. The measurements were made between 304 K and 390 K using the C2 DUALSPEC diffractometer located at the NRU Reactor. The diffraction profiles show numerous narrow, single peaks, in addition to the overlapping peaks, confirming a relatively simple structure at these temperatures. The data are currently being analyzed using the Rietveld program GSAS.

Materials Science

2.3.1.16 Atomic Ordering and Lattice Site Location in Al_3Ti-Based Alloys

S.M. Kim with D.G. Morris (University of Neuchâtel) and R.L. Donaberger (McMaster University)

The titanium trialuminide alloys have received extensive investigation from the materials engineering community since these intermetallics are of low density, have good resistance to oxidation, and keep strength to high temperatures. The binary alloy Al_3Ti has the DO_{22} crystal structure and is very brittle. However, substituting some of the aluminium by a transition metal, such as Cr or Mn, leads to a change of the crystal structure to $L1_2$ with some improvement in ductility.

The long range order and site location of various atoms in the $L1_2$ phase Al-Ti-X alloys (X = Cr, Fe, etc.) have been studied previously by several groups with X-ray diffraction technique at room temperature. However, the results were inconsistent and inconclusive, because of the overlap of some of the second phase peaks with the main diffraction peaks, as well as the use of incorrect or imprecise analyses.

Since the various second phases present at room temperature are expected to dissolve in the matrix at high temperatures, and since the long-range order parameter is expected to depend on temperature, we have carried out neutron powder diffraction measurements on Al-Ti-X alloys (X = Cr, Cu, Fe and Mn) as a function of temperature from room temperature to 1200°C. The measurements were made on the C2 DUALSPEC powder diffractometer located at the NRU reactor. The rapidly-solidified powders were produced by spray depositon method and had a mean diameter of about 50 microns.

The data were analyzed with the Rietveld analysis program GSAS. It was found that the site location of various atoms deduced from this analysis depended strongly on the temperature factors. An assumption of a uniform temperature factor, which was used in previous X-ray measurements and analyses, was found to be entirely inadequate, and that it was essential to assign different temperature factors for the two different sublattices. The temperature factor for the atoms on the aluminium sublattice was significantly larger than that of the atoms located on the titanium sublattice at all temperatures including room temperature.

Preliminary analyses show that in $Al_{66.7}Ti_{25.7}Mn_{7.6}$ and $Al_{64}Ti_{28}Fe_8$, the Ti sublattice is occupied mostly (98 ± 2%) by Ti atoms at all temperatures up to 1200°C. In $Al_{62}Ti_{27}Cu_{11}$, the Ti sublattice is also occupied mostly by Ti atoms at room temperature, but as the temperature is increased the alloy becomes increasingly disordered - such that at 1200°C, the Ti sublattice contains either (5 ± 2)% Al or (3 ± 1)% Cu. Whether the atoms locating at the Ti sublattice are Al or Cu, or some combination of the two, cannot be determined by neutron diffraction measurements alone - for this purpose, combined neutron and X-ray diffraction measurements are required. In $Al_{65}Ti_{26.9}Cr_{8.1}$ at room temperature, the Ti sublattice is occupied by Ti atoms plus (4 ± 2)% Al or Cr atoms. At 1200°C the Ti sublattice is occupied by Ti atoms plus about (12 ± 2)% Al or Cr atoms. As in the case of $Al_{62}Ti_{27}Cu_{11}$, neutron diffraction measurements alone cannot distinguish whether the atoms occupying the Ti sublattice are Al or Cr. It is not clear at present why in $Al_{66.7}Ti_{25.7}Mn_{7.6}$ and $Al_{64}Ti_{28}Fe_8$, the long-range order on the Ti sublattice is almost perfect, while in $Al_{62}Ti_{27}Cu_{11}$ and $Al_{65}Ti_{26.9}Cr_{8.1}$, the Ti sublattice as well as the Al sublattice become increasingly disordered as the temperature is increased.

2.3.1.17 Site Location of Atoms in the $L1_2$ Intermetallic Compounds Al_3Ti-X (X=Fe, Ag, Ni and Mn) by Neutron Diffraction

S.M. Kim with A. Kameyama and M. Kogachi (University of Osaka Prefecture)

Intermetallic compounds of $L1_2$ structure Al_3TiX (X=Mn, Fe, etc.) are considered promising candidates for high temperature structural materials which are light, strong and oxidation resistant. Some of the mechanical properties of these compounds are expected to be controlled by the strength of atomic bonds and the site location of the various constituent atoms. Although previous X-ray diffraction measurements at room temperature have provided some information on this topic, X-ray measurements alone cannot give complete information, since there are three atomic species distributed over two different sublattices.

We have carried out neutron powder diffraction measurements on $Al_{65.5}Ti_{26}Ag_{8.5}$, $Al_{65.8}Ti_{25.1}Fe_{9.1}$, $Al_{66.5}Ti_{25.5}Ni_{8.0}$ and $Al_{64.5}Ti_{27.2}Mn_{7.9}$ from room temperature to 1200°C. The measurements were made on the C2 DUALSPEC powder diffractometer located at the NRU reactor. The specimens were fabricated using plasma arc furnace and pulverized by ball milling process. The mean size of the powders thus produced was about 10 microns. Neutron diffraction profiles showed that these compounds also contained small amounts of second phases at room temperature as well as at high temperatures, making it difficult to analyze. In addition, small amounts of Al_2O_3 (one or two percent in volume) were also formed at temperatures 1000°C and above - partly owing to the very high surface to volume ratio of these powders.

The data were analyzed using the Rietveld analysis program GSAS. The temperature factor for the Al sublattice was assumed to be different from that for the Ti sublattice. In addition, the amount of Al_2O_3, its lattice parameters and the uniform temperature factor were varied for the high temperature data. Preliminary results so far indicate that in $Al_{65.8}Ti_{25.1}Fe_{9.1}$, the Ti sublattice is mostly (99 ± 1)% occupied by Ti atoms at all temperatures between 20°C to 1200°C. In $Al_{65.5}Ti_{26}Ag_{8.5}$ the Ti-sublattice is also mostly (99 ± 1)% occupied by Ti atoms at temperatures between 1000°C and 1200°C.

2.3.1.18 Internal Stresses in a Particulate Reinforced Al:SiC Composite

T.M. Holden with N.J. Townley and J.D. Boyd (Queen's University) and D.J. Lloyd (Alcan International)

The crystallographic texture and the interphase residual stresses have been determined by neutron diffraction in an aluminum 2014 alloy (Al-4.4 Cu-0.5 Mg) reinforced with 20 vol.% SiC particulate. Small coupons were cut from as-prepared and hot-extruded billets to relieve the macroscopic strains resulting from manufacture, and the measurements were made at 5° intervals between the extrusion

direction and the transverse direction. Measurements were made on the (002) matrix peak and the (220) and (440) SiC peaks as only these peaks are well separated in the diffraction pattern.

The as-cast sample shows random texture for both Al matrix and particulate. The sample prepared with 20:1 extrusion ratio (the ratio of the initial cross-sectional area of the billet to its final area) shows a weak (1.8 times random) axially symmetrical texture with (002) poles aligned along the extrusion direction. The SiC lines exhibit no texture. The texture is still weaker for 5:1 extrusion ratio.

The SiC in the matrix exhibits residual compression with respect to the SiC powder used to make the specimens, and the Al in the composite exhibits residual tension for the extruded samples. The magnitudes of the stresses are consistent with the effect of the mismatch of the thermal expansion. The average matrix stress in the as-cast sample is much less than the average matrix stress in the extruded samples. Metallography reveals large (300 mm diameter) particulate-free regions which would be expected to have no interphase stresses. Extrusion reduces these regions, making the distribution of particles more uniform. For the extruded samples a systematic difference was noted between the strains parallel and perpendicular to the rolling direction. This effect is connected with the average separation of the SiC particles which is different parallel and perpendicular to the rolling direction.

2.3.1.19 Measurements of Diffraction Line Broadening and Residual Strain Near the Crack Tip in Compact Tension Samples

T.M. Holden with J. Smith and N. Bassim (University of Manitoba)

The purpose of the present experiment was to map out the plastic zone ahead of a fatigue crack formed in compact tension samples subjected to different pre-cracking stress intensity factors and different quasi-static loads. The experiments were performed at the E3 spectrometer at the NRU reactor with a wavelength of 2.3289 Å in a high resolution configuration designed to give a linewidth of about 0.3°. High spatial resolution was also required to map out the plastic zone and a gauge volume of 1.4 x 1.4 x 1 mm^3 was used. The measurements were made of the strain component normal to the crack plane at a number of positions near the crack tip. The samples which had been subjected to a quasi-static load during the fatigue process each showed about a 16% increase in diffraction linewidth at the crack tip. This decreased to zero at about 3 mm from the crack tip. These samples also showed compressive residual strains of about -8×10^{-4} at the crack tip, rising through zero strain 1.5 - 2.0 mm from the tip, to a tensile maximum of $+7 \times 10^{-4}$ at locations 3-4 mm from the tip. The fatigue sample prepared with zero quasi-static load and the smallest stress intensity (20 MPa $m^{1/2}$) showed no linewidth change as a function of distance from the tip and no residual stress. On the other hand the sample prepared with no quasi-static load, but a stress intensity of 47 MPa $m^{1/2}$ showed a 6% increase

in linewidth as well as a small (-2.5×10^{-4}) residual stress at the crack tip. Not unexpectedly, a residual strain accompanies any inhomogeneous strain deformation. The surprising feature is that the fatigue pre-cracking in the absence of a load can produce linewidth changes.

2.3.1.20 The Measurement of Residual Strains Near Surfaces

T.M. Holden and R.B. Rogge with P.J. Webster and G. Mills (University of Salford)

Previous measurements (PR-PHY-6:2.3.1.20; AECL-10878) highlighted several sources of systematic error in near-surface measurements. The variation of neutron wavelength across the beam width, and the offset of the location of the irradiated material from the centre of the gauge volume, can be brought down to the level of the statistical error by reducing the dimensions of the gauge volume. A further source of error is the parallax in the detector when the exit slit is not close to the centre of the gauge volume. This may be avoided by special slit design (2.3.4.3) permitting the slit-to-gauge-volume-centre distance to be less than 1.5 mm. An innovative method of performing the scans with the multiwire detector gives a factor five gain in efficiency over a single detector. Test measurements were made of the (113) peak of Ni powder with slit widths of 0.3 mm as the powder surface was moved through the gauge volume in both reflection and transmission geometries. The shift in angle was about one standard deviation when the gauge volume is centred at the nominal wall position.

Measurements of the normal and in-plane strains were made on a heavily peened sample of Waspaloy. The normal strains were in tension, $(22 \pm 5) \times 10^{-4}$, near the surface, becoming compressive 0.3 mm below the surface and reaching maximum compressive values of $(-7 \pm 3) \times 10^{-4}$ (at 0.4 mm below). The in-plane strain was compressive near the surface, $(-30 \pm 5) \times 10^{-4}$, becoming tensile 0.3 mm below the surface to reach a maximum tensile strain of $(+6 \pm 3) \times 10^{-4}$ at 0.4 mm below the surface. An increase in diffraction linewidth was noted beginning at the location of the "overshoot"; i.e., about 0.4 mm below the surface.

Strain measurements were also made on heat-treated, carburized and peened samples. The same qualitative features were observed, namely high tensile normal strains, and high compressive in-plane strains and linewidth increases corresponding to the position of the overshoot peak. Analysis methods have now to be developed to deconvolute the strain and the width at each part of the gauge volume for the cases where the gauge volume is partly filled.

2.3.1.21 Residual Stress Distribution in a Shot Peened and Compressively Overloaded Aluminium Fatigue Sample

T.M. Holden and R.B. Rogge with R. Lin (Uppsala University)

U-shaped fatigue samples, made of aluminum AA7050-T73651, were shot peened in the load critical surfaces, namely the inner surface of the U-curve and its two side-surfaces. The shot-peened samples were then subjected to a static compressive load in the hoop direction to simulate a straightening operation, which caused plastic deformation of the surface region of the inner U-curve.

To investigate the residual stress field introduced by the shot peening and overloading processes, residual stress measurements were carried out with the L3 spectrometer at NRU. Residual elastic strains of the axial, hoop and radial components were obtained both at the mid-thickness and at 1 mm depth from the side. In addition, two sets of scans were also made from the mid-thickness towards the surface along the inner U-curve at 1 mm and 2.5 mm depth, respectively.

Preliminary data analysis showed that hoop tensile stresses exist in the surface region of the inner U-curve, with a maximum stress of 130 MPa at the mid-thickness and 50 MPa at 1 mm depth. The tensile stresses decrease with increasing distance from the inner surface and change to compressive stresses at about 3 mm depth. On the other hand, compressive stresses were found in both radial and transverse directions in the inner surface region. The effect of plastic deformation and recovery on radial and axial strains is expected to be the same (but opposite to the hoop strain) and decreased by ν, Poisson's Ratio, while the effect of shot peening would be to make the radial strain more tensile and the axial strain more compressive. However, we observe that the axial and radial strains are nearly equal. Therefore, it seems that any compressive stresses that might have been induced by the shot peening process were relaxed by the plastic deformation arising from overloading in compression.

The hoop stress distribution curve obtained at the mid-thickness agreed with X-ray measurements carried out on a similar sample, with the stress maximum found at a slightly different location. For neutron diffraction measurements the maximum appeared at the surface of the inner U-curve while for X-ray diffraction measurements it was found at 1 mm distance from the surface.

2.3.1.22 Mechanical Properties of a Binary Mg-Al Alloy

J.H. Root with M. Gharghouri (McMaster University)

Work is continuing at McMaster University to investigate the partitioning of internal stresses between a relatively large volume fraction (8%-9%) of a hard second phase and the magnesium matrix during deformation of a binary Mg - 8.5 wt% Al alloy.

The second phase is obtained by artificial aging which yields large platelets of the intermetallic $Mg_{17}Al_{12}$ approximately 10 μm long and 3 μm wide and deep. Pure magnesium, with a similar grain size and texture, was chosen as a base material with which to compare the deformation behaviour of the composite. The current experiments were undertaken to determine whether any residual stresses are present in the two materials before deformation. Measurements of small angular shifts in diffraction peaks were made with the C2 DUALSPEC powder diffractometer. The shifts were analyzed to determine strain and residual stress. It was found that no significant stresses are present in the pure metal whether it is quenched, air-cooled, or furnace-cooled after annealing to produce the desired grain size. It also appears that no stresses are present in the alloy as a result of the precipitation reaction, but work is continuing at McMaster University to confirm this. Mechanical tests are being performed at McMaster University in order to obtain stress-strain data for the material. It is then desired to perform tests at Chalk River using the in-situ stress rig to observe the evolution of internal stresses during deformation.

2.3.1.23 Texture Development in Hot Rolled AA5XXX Aluminum Alloys

J.H. Root with M.A. Wells (University of British Columbia)

Texture measurements were made on an AA5182 (Al-4.5%Mg) aluminum alloy using the E3 neutron diffractometer at Chalk River. These measurements complete earlier work to assess the effect of hot rolling variables (total strain, strain rate and temperature) on the as-deformed texture characteristics for an AA5182 aluminum alloy. The current set of experiments examined the effect of total strain (0.5 - 2.0) and deformation temperature (350°C-500°C) on the texture characteristics. The work showed that the total strain has a significant impact on the as-deformed texture and that, as the total strain increased, the strength of the as-deformed texture also increased. In addition, the manner in which the texture evolved during static recrystallization was assessed. Volume fraction estimates of the texture components present in the as-deformed structure and during recrystallization will be calculated with software at the Alcan International Research Laboratories in Kingston. The textures developed during recrystallization will then be correlated to the microstructure produced under each condition.

2.3.1.24 Texture of Minority Phases in Pressure Tube Materials

J.H. Root with R.W.L. Fong (Fuel Channel Components Branch) and P. Gangli (McGill University)

Current theory maintains that, for a given zirconium-hydride concentration, hydride orientation and re-orientation is only dependent on the texture of the alpha-phase and on the stress-temperature history of the material. There is reason to believe that mis-orientation relationships, which occur at hydride-beta, alpha-beta and alpha-beta-

hydride interfaces, strongly influence strength, fracture and heat resistance behaviour of zirconium alloys in a compound manner.

Neutron diffraction has provided the simultaneous measurement of the textures of alpha, beta and hydride phases in a single specimen from tube #R766, which contained 41.4 ppm (wt) of added deuterium in the predominant form of δ-hydrides. Beta-phase (200) and hydride (111) pole figures are shown in Fig. 2.3.1.3. The beta-phase exhibits a typical bcc rolling texture. The hydride texture exhibits a (111) intensity distribution that includes a broad distribution in the radial-hoop plane, corresponding to the main feature of the alpha-phase (0002) pole figure. The correspondence of features between the alpha (0002) and hydride (111) was expected from observations by transmission electron microscopy (J.S. Bradbrook, et al., J. Nuc. Mater. 42 (1972), 142). Because the neutron diffraction data sample all of orientation space and provide true volume sampling of the crystallite orientations, the analysis of interface mis-orientations can now be performed, in principle.

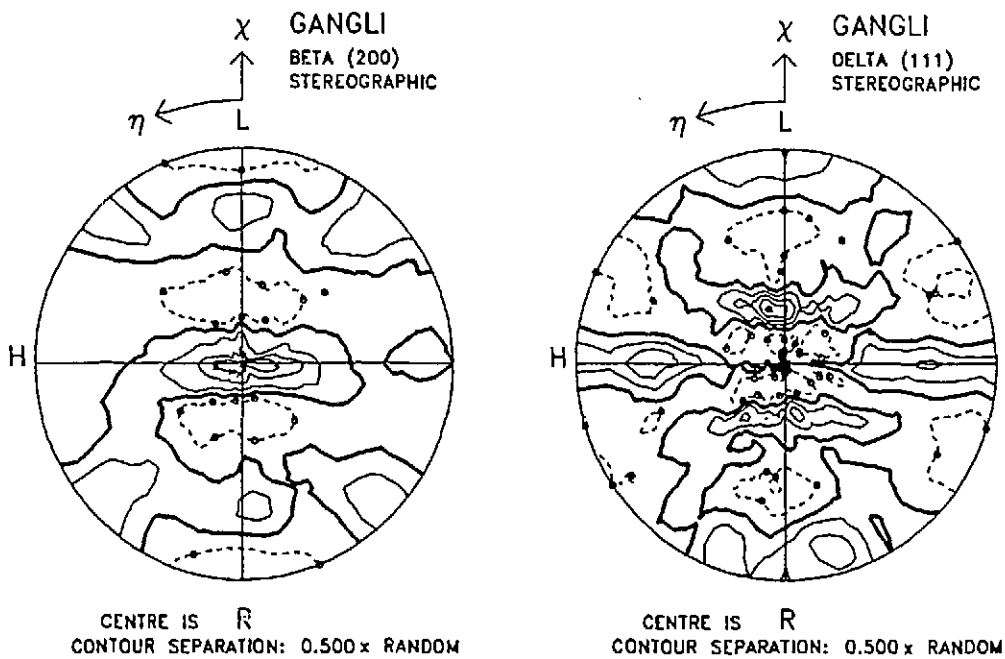

Fig. 2.3.1.3

2.3.1.25 Residual Stresses in Iron-Cementite Composites

J.H. Root with J. Schröder (GKSS Forschungszentrum)

As part of a research project at the GKSS Forschungszentrum, to understand plastic deformation in multi-phase materials, neutron diffraction measurements were made to determine the residual stresses in the ferrite phase of mild steel (0.45 wt% C). These stresses were expected to be balanced by stresses in the minority cementite phase. However, the cementite has a low symmetry (orthorhombic) and comprised a small volume fraction of the steel. The diffraction peak intensities were not large enough to determine stresses in the cementite with adequate precision on the GKSS neutron diffraction instrument.

Two series of specimens of carbon steel (0.77 wt% C), one with spheroidized and the second with normalized microstructures, were produced with various amounts of uniaxial plastic deformation. Neutron diffraction patterns were collected with the high-throughput, DUALSPEC powder diffractometer at Chalk River. Patterns were collected for a number of orientations of each specimen, to sample many stress components with each diffraction peak. The specimens with the spheroidized microstructures produced very intense ferrite peaks and weak, but well-defined cementite peaks. As the plastic deformation increases, the axial compressive strains in the ferrite increase from -6×10^{-4} to -8×10^{-4}. The strains deduced from shifts in 10 cementite peaks are tensile and of higher magnitude, with values as high as $+64 \times 10^{-4}$ detected. Thus, the compressive microstresses in the ferrite phase of the steel are balanced by tensile stresses in the cementite. Because the volume fraction of cementite is about 10%, larger strains and stresses are needed to balance those of the ferrite matrix. The specimens with the normalized microstructure (pearlitic, with cementite layers of thickness 20-100 nm) produced broad, weak cementite peaks, whose analysis is more complicated, and not yet completed.

Theory

2.3.1.26 Mathematica Program for the Incoherent Scattering Function

V.F. Sears

A Mathematica program has been written to calculate the multiphonon expansion of the incoherent scattering function $S(Q, \nu)$ as a function of the frequency ν at a specified wave vector Q and temperature T in terms of an assumed model for the velocity spectrum $f(\nu)$. The $f(\nu)$ is the Fourier transform of the velocity autocorrelation function for the scattering atom and is closely related to the phonon density of states $g(\nu)$. For a cubic Bravais lattice $f(\nu)$ is equal to $g(\nu)$ but, in general, $f(\nu)$ depends on both the phonon frequencies and the phonon polarization vectors. The program was tested using the Debye model for $g(\nu)$, with parameters appropriate

for aluminum, and it was verified that the calculated S(Q, ν) approaches the result for the impulse approximation at large Q as it should.

This program is now being used to make multiphonon corrections in neutron inelastic scattering experiments. It has been applied in the analysis of the experiments on crystalline and amorphous ice (2.3.1.27) and it will be applied to data for cristobalite.

2.3.1.27 **Phonon Density of States in Crystalline and Amorphous Ice**

V.F. Sears and E.C. Svensson, with W. Montfrooij (Risø National Laboratory) and D.D. Klug (National Research Council)

In the previous report (PR-PHY-6: 2.3.1.2; AECL-10878) we described results for the phonon density of states of the hexagonal (Ih) phase of crystalline ice and of the high-density amorphous (hda) phase at T = 11 and 80 K which were obtained from a preliminary analysis of recent high-resolution neutron inelastic scattering experiments at Q = 2.5 $Å^{-1}$ and a frequency range −0.10 to 3.66 THz. We have now corrected these data for the effect of multiphonon scattering, using a Mathematica program (2.3.1.26) and have put the g(ν) results on an absolute scale.

To do this, we first took our earlier results (D.D. Klug, E. Whalley, E.C. Svensson, J.H. Root, and V.F. Sears, Phys. Rev. B44 (1991), 841) for the velocity spectra f(ν) of the Ih and hda phases, which were determined from neutron inelastic scattering measurements at Q = 6 $Å^{-1}$ and T = 15 K, and used them to calculate S(Q, ν) for both these phases at Q = 2.5 $Å^{-1}$ and T = 11 and 80 K where the new high-resolution experiments were performed. We found that this value of Q is sufficiently small that we could terminate the multiphonon expansion after the two-phonon term with negligible error. Table 2.3.1.1 lists the calculated values of $S_n(Q)$, which is the integrated intensity of the n-phonon contribution to S(Q, ν), as well as the calculated values of u (the rms displacement of a hydrogen atom in the direction of Q) and T_0 (the average kinetic energy of a hydrogen atom).

We next fit gaussians to the elastic peaks in the new data, in order to subtract the elastic scattering from the total scattering. The resulting inelastic scattering distributions were then normalized by fitting their integrated intensities to the corresponding calculated S(Q, ν) curves. Finally, we subtracted the calculated multiphonon scattering from the normalized total inelastic scattering to get the one-phonon scattering, and hence the normalized velocity spectrum f(ν), for each distribution. These were then converted to the phonon density of states g(ν) using the same model as in our earlier work (loc. cit.). The new g(ν) results for ice Ih at 11 K are shown by the dots in Fig. 2.3.1.4 where they are compared with the earlier lower resolution results (solid line). The agreement between the two sets of results is generally good, although there are some as yet unexplained discrepancies above

TABLE 2.3.1.1

Calculated quantities for Ih and hda ice (see text)

Ice Phase		Ih	Ih	hda	hda
Temperature (K)		11	80	11	80
$S_n(Q)$	n = 0	0.807	0.736	0.795	0.728
	n = 1	0.173	0.226	0.182	0.231
	n = 2	0.019	0.035	0.021	0.037
	n = 3	0.001	0.003	0.002	0.004
	total	1.000	1.000	1.000	1.000
u (Å)		0.185	0.222	0.192	0.225
T_0 (K)		508	509	472	474

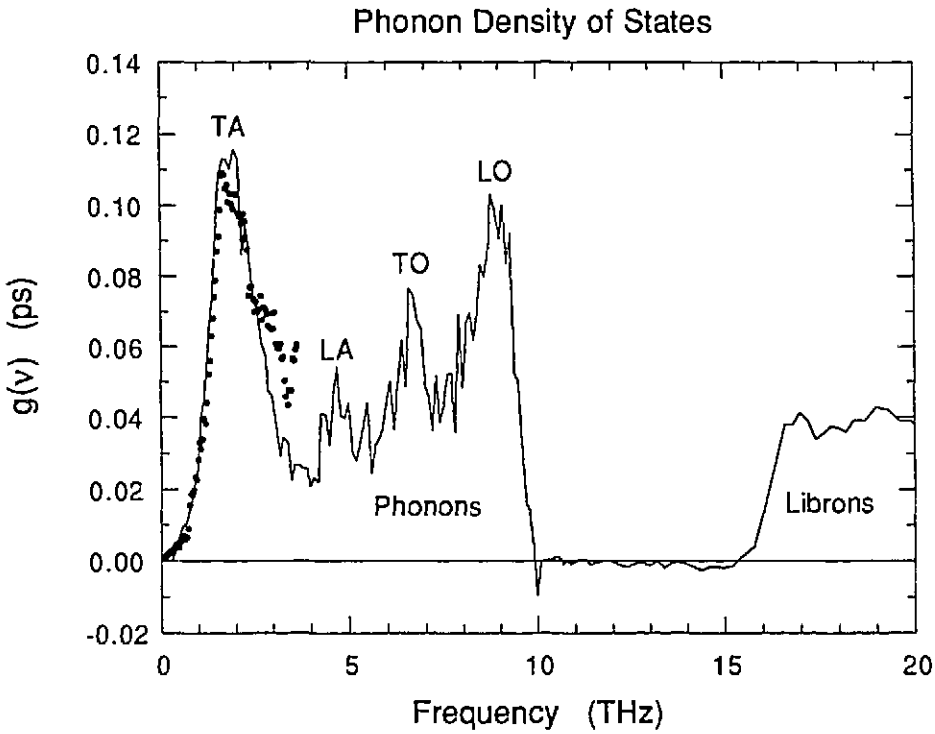

Fig. 2.3.1.4 Comparison of our earlier results (solid line) for the phonon density of states g(ν) for ice Ih at 15 K with those from the present analysis of newer high-resolution measurements at 11 K (dots).

3 THz that are larger than one would expect from the statistical uncertainties. The most interesting physics is in the region below 1 THz where our preliminary analysis showed an excess of intensity in g(ν), centered at about 0.6 THz, for the hda phase at 11 K relative to that for the Ih phase at the same temperature. The present more accurate analysis confirms this conclusion.

2.3.1.28 Electron-Ion Superconductivity with Electron-Hole Asymmetry

F.J. Marsiglio with J.E. Hirsch (University of California at San Diego)

The work reported in the previous progress report (PR-PHY-6:2.3.1.24;AECL-10878) has been completed. The Eliashberg equations for the electron self-energy and pairing function have been solved numerically for a model with retarded interactions which does not have electron-hole symmetry. This model is motivated by the structure of the cuprate superconductor. We have found that the superconducting T_c is enhanced because of both retardation and electron-hole asymmetry in the hole-hole interaction.

2.3.1.29 Novel Mechanism for Superconductivity Through Electron-Ion Interactions

F.J. Marsiglio

Generalized Eliashberg equations for superconductivity were derived, starting from a model Hamiltonian that includes the standard electron-ion interaction (Holstein-type coupling denoted by α), and, in addition, a new type of interaction; an ion degree of freedom that couples to the electron double occupancy (ion-modified Hubbard model with coupling denoted by α'). To keep the calculation tractable, we performed a perturbation expansion in α'/α. No qualitatively different physics emerges as a result of the inclusion of this new interaction, but quantitative corrections to the standard theory result from the new coupling.

2.3.1.30 Exact Diagonalizations of Many-Fermion Systems

F.J. Marsiglio

Two outstanding questions remain to be resolved concerning interacting electrons in two dimensions. First, do interacting electrons exhibit fermi liquid behaviour, and second, under what conditions is the ground state superconducting? To put more approximate treatments (e.g. BCS, T-matrix, etc.) on a rigorous footing, a general purpose program has been written which will determine the Hamiltonian matrix and diagonalize it to obtain the exact eigenvalue spectrum for small systems. Further work to compute other properties is in progress.

2.3.1.31 Conductivity of Vortex Cores

T.C. Hsu with H.D. Drew, E-J. Choi and S. H-T. Lihn (University of Maryland)

Vortices are whirlpool-like defects in the wavefunction of paired electrons in superconductors. Their properties are important in determining the behaviour of superconductors in real applications. A theory for the conductivity of vortex cores in type II superconductors was further developed and compared to the latest experimental results from the University of Maryland. The theory is consistent with the observed cyclotron resonance and small chiral response at the vortex core excitation frequency in a number of high temperature superconductors. A model incorporating pinning by linear defects (which breaks cylindrical symmetry) was able to explain the observed non-chiral response at the core excitation frequency.

2.3.1.32 Calculation of Spin Structure Factors in ABX_3 Compounds

T.C. Hsu, Z. Tun and M. Couture with J.-G. Lussier (McMaster University)

The identification of the spin excitation spectrum of stacked antiferromagnetic chains is nearly complete. Spin wave spectra and neutron scattering structure factors in stacked antiferromagnetic chains were calculated in order to compare with experiments on $CsNiCl_3$ and $CsMnI_3$ by Z. Tun, J-G. Lussier and W.J.L. Buyers.

The problem of identifying the "xz polarized" modes in the ABX_3 stacked antiferromagnetic chain systems was attacked from three fronts: (a) the non-interacting spin wave spectrum in the presence of single-ion anisotropy was calculated analytically; this calculation was made possible with the recent acquisition of symbolic manipulation software (MAPLE V); (b) the numerical calculation of the spin structure factor, $S(q,\omega)$, taking into account magnon-magnon interactions to lowest order was performed; this requires ignoring the single ion anisotropy term; (c) finally, a computer program utilizing the local field approach of Buyers, Holden and Perreault was ported to the Challenge-L workstation with modification to treat the case $S \neq 1$. The most recent experimental data are being analyzed with respect to these theoretical calculations.

2.3.1.33 Multiple Scattering and Wavelength Dependent Scattering in Steel Plates

T.C. Hsu, F. Marsiglio and J.H. Root

A systematic study has been undertaken of the effects of multiple scattering and wavelength dependent attenuation on residual strain measurements by neutron diffraction in steel plates. There have been persistent observations of small inconsistencies in residual strain measurements by neutron scattering in large

samples. Discrepancies of order of 1 part in 10^4 were observed depending on whether or not the neutron beam traversed a long (~ 10 mm) path through the sample material before reaching the gauge volume. It was proposed that multiple scattering or wavelength dependent attenuation might explain these discrepancies. It was decided to test these possibilities in a systematic study of residual strain in a set of steel plates. A calculation was performed that showed wavelength dependent attenuation could be significant at the level of 1 part in 10^4 at a depth of 10 mm in steel plates. Experimental results agreed roughly with the calculations and further measurements are being performed to improve the statistical significance. The experiment has shown that the effects arising from multiple scattering are insignificant. Theoretical tables will be produced which can be used in the future to make corrections for wavelength dependent attenuation in common metallic elements.

2.3.2 Neutrino Physics

2.3.2.1 Acrylic Sheet Quality Control

E.D. Earle, R.J.E. Deal and E.R. Gaudette

SNO has purchased 150 acrylic sheets, 2" by 72" by 117", and 20 acrylic sheets, 4" by 69" by 72". These sheets represent about 80% of the sheets made by Polycast for SNO. The remainder were rejected because of defects. The quality control of the purchased sheets has been performed by the manufacturer, Polycast, and by CRL. Almost all of the sheets purchased satisfied the thickness, inclusions and mechanical specifications. The Th and U content specifications were also well satisfied and, in fact, were in general an order of magnitude better than the specifications. The optical transmission of the sheets varied between batches (a batch consisted of 10 to 20 sheets) and some purchased sheets did not meet the optical specifications.

The vessel will contain 112-2" sheets and 10-4" sheets. The remaining 48 sheets are being used to test the vessel-fabricator's procedures and as spares for the vessel. The sheet inventory was examined and the selection of spares was based on Th/U content (the 13 sheets in batch 80 were about five times worse than the others) and on optical quality (the worst sheets were not assigned to the vessel).

This stage of the acrylic quality control is complete. We are now testing various aspects of the fabrication. To date, samples that have been thermoformed, machined, annealed and bonded, while worse than the virgin material, still meet the Th/U content specifications. The expected optical deterioration at the bond joint is as expected but the bulk of the sheet is unchanged optically.

2.3.2.2 Th/ U Content in Plastics by NAA

E.D. Earle, R.J.E. Deal and E.R. Gaudette

The neutron activation analysis (NAA) and gamma counting facilities at CRL that are being used to measure the Th/U content of the acrylic are also used to measure the Th/U content in other materials. Measurements have been conducted on kevlar and vectran, two possible fibres for the acrylic vessel suspension ropes, on possible piping materials for the water process systems and on nylons being considered by Borexino for their solar neutrino detector. Environment Research Branch uses the counting system for their cleanest or lowest background samples. This program will continue.

2.3.2.3 Silicon Diode Cryotrap for Radon Detection

B. Sur, E.D. Earle, E.R. Gaudette and R.J.E. Deal, L.E. McEwan, G.A. Sims with E. Bonvin and A. Hamer (Queen's University)

The silicon diode cryotrap is an ultra-sensitive radon detection system, developed for monitoring the D_2O radiopurity in SNO. The Th chain contamination of the D_2O, crucial for SNO background determination, will be measured by flowing it through filters with MnO_2 coated acrylic beads which will extract ^{224}Ra. The cryotrap system will then be used to assay the ^{224}Ra by trapping and detecting its noble gas daughter, ^{220}Rn, which is emanated from the MnO_2 beads. At the projected D_2O radiopurity of 10^{-15} g/g equivalent ^{232}Th, an assay of some 50 tonnes of water will produce only about 90 ^{220}Rn atoms in 15 days of counting.

The trap itself is a 1 cm^3 gas-tight cell consisting of a stainless steel middle piece, with thin-walled SS inlet and outlet tubes. The walls of the cell are 1 cm x 2 cm bare Si PIN photodiodes with indium seals made directly to their active surfaces. Our studies have shown the cryotrap to be an efficient Rn trap at liquid nitrogen temperature. It is also an excellent detector of alphas from Rn and its daughters, with good energy and time resolution, 50% geometrical efficiency and very low intrinsic background. It is expected that the MnO_2 - Si cryotrap system will have a sensitivity of 10^{-16} g/g equivalent Th for a 50 tonne D_2O sample.

In a series of meetings in 1993 August and September, the Si diode cryotrap was selected as the primary device for the Th chain assay of the D_2O in SNO. It is expected that eventually up to 20 cryotrap systems may be required at Sudbury. As a start, SNO has commissioned five cryotrap systems to be set up at CRPP, Ottawa for studies of the water purification system and systematics of the monitoring techniques. The CRL group is in the process of procuring these initial five systems. The production cryocell design, based on development devices made at CRL and Queen's, has been synthesized and five units are being machined at STC, Ottawa. We have obtained quotations for major components such as liquid nitrogen cryostats,

vacuum pumps, clean recirculation (diaphragm) pumps, gauges, valves, etc. After considerable dialogue, the cryostats have been ordered from Andonian Cryogenics in Massachussetts and will be delivered to CRL in 1994 late January. We are testing the pumping speed of the diaphragm recirculation pumps at low pressures (~ 10 torr) because these specifications are not available from the manufacturers. With the fortuitous discovery of a low-cost GAST pump which is used by the Radiation and Industrial Safety Branch at CRL, we are close to finding an affordable pump for this purpose. The design of machined components has been finalized. These are being machined at the Queen's University Physics machine shop.

We have modified and tested existing preamp modules at CRL for use in processing the Si diode signals. These modules were used previously in neutron spectrometer multi-wire gas detectors. They are based on a combination of an AMPTEK203 charge-sensitive preamp + shaping amp. and an AMPTEK206 voltage amp. + discriminator. These modules have good noise characteristics and alpha-particle resolution. The experimental values are in fact no worse than a "standard" ORTEC142 preamp and ORTEC471 spectroscopy amp. set-up. The AMPTEK206 amplifier obvitates the need for a main (NIM) amplifier in the signal processing circuit. The projected use of these modules (after modification) in the SNO cryodetectors will result in a cost savings of at least $50,000 for the SNO project.

We continue to develop and test the cryodetector and associated monitoring systems. A new cryocell design with a grooved 0.015" wide indium seat, larger Si active area, and with an angled inlet directed at one of the Si diodes, was commissioned from the Mechanical Equipment Development Branch. This cell has been constructed and as expected has performed better than the previous cells. We have designed and built a novel "mushroom" shaped MnO_2 filter column. This allows for radically different aspect ratios for the shape of the bead packing during Ra extraction (long and narrow) and Rn emanation (thin and flat) without an external transfer. The machining and welding of these SS columns were undertaken with special attention to U and Th chain contamination. The background of the finished columns is satisfactorily low, and early indications from water flow studies at CRPP are that these columns perform significantly better than previous models.

Finally, we have designed and constructed a "water trap" to be operated at about 120 K to act as a pre-filter for condensible gases such as water vapour in the Rn trapping loop of the cryotrap system.

2.3.2.4 D-T Neutron Generator Based Gas Calibration Sources for SNO

B. Sur, E.D. Earle, E.R. Gaudette and R.J.E. Deal with V. Koslowsky, E. Hagberg, M. Watson (Nuclear Physics Branch) and E.B. Norman (Lawrence Berkeley Laboratory)

We have proposed a calibration scheme for the SNO detector in which suitable high decay energy (hence short-lived) sources are produced by 14 MeV neutron irradiation of an appropriate gaseous or solid target material. The neutrons are to be obtained from a small D-T neutron generator, located in a "pit" in one of the SNO underground laboratory corridors. We propose then to quickly transport this activity to an appropriate decay chamber in the D_2O volume by fast gas transport through a Teflon capillary tube. Such gas-capillary fast transport systems are used by many groups around the world, including the ISOL group at TASCC.

a) ^{16}N

The nucleus ^{16}N decays with a 7.13 second half-life, and produces a 6.13 MeV gamma-ray with a 68% branch. At a delivered decay rate of about 100 per second, this source is envisaged as the "everyday" calibration source for monitoring relative PMT efficiencies, the absolute energy scale and "gain shifts". We propose to produce this source via the $^{16}O(n,p)$ reaction with pure O_2 gas as both target and source carrier gas. The concept and quantitative production rates, efficiencies, etc., have been successfully verified in a series of experiments carried out at the D-T generator facilities in Health Physics Branch. Computer programs have been written to calculate yields, and to optimise chamber dimensions. These programs show that a decay rate of 100 s^{-1} will be easily obtained with a neutron generator intensity of less than 10^7 neutrons s^{-1}. The next step in this project is to specify and procure a D-T generator so that engineering of the system can proceed.

b) ^{8}Li

The nucleus ^{8}Li beta-decays with a 0.84 s half-life and an end-point energy of 13 MeV. The beta-spectrum shape is almost the same as the ^{8}B decay solar neutrino spectrum which will be observed in the SNO detector. Calibration with this source will thus verify the detector's ability to distinguish spectral distortions in the neutrino spectrum arising from proposed neutrino oscillation scenarios. We propose to produce ^{8}Li via the $^{11}B(n, \alpha)$ reaction with 14-MeV neutrons from the D-T generator. The ^{8}Li nuclei recoiling from the target will be transported to the detector volume by aerosol particles in a He gas stream flowing through a Teflon capillary tube. The viability of this scheme has been verified at the TASCC facility: a broad distribution of neutrons peaked around 12 MeV was generated by a 28-MeV deuteron beam incident on a thick Be target. The installed gas

transport and detection systems of the ISOL group were utilized. The experiment confirmed a ^{8}Li production rate of 2 x 10^{-7} per neutron for a BN target. The results also confirmed the contamination of the activity by ^{11}Be (13.8 s half-life) made via the ^{11}B(n,p) reaction. In a subsequent experiment, we attempted to suppress the relative yield of ^{11}Be by coating the surface of the target with an inert layer of carbon. The relative yield of ^{11}Be was suppressed from 7.5% to 2% with a 1 mg cm^{-2} inert coating while the ^{8}Li production rate dropped to 44% of the value with no coating. The residual contamination is hypothesized to arise from production via high energy neutrons from the broad incident neutron beam.

We have attempted to verify the ^{8}Li production and transport rates and the ^{11}Be suppression factor from monoenergetic 14 MeV neutrons obtained at the D-T generator facility in the Health Physics Branch. Other features of this new experiment are a long (15 m) capillary transport line, a 90% pure B target made with 97% isotopic ^{11}Be powder, and calibrated interchangeable inert layers made of stretched polypropylene foils. Preliminary results indicate a capillary transport efficiency of approximately 50%.

Optimization codes have been written as a first step towards designing a ^{8}Li calibration source for SNO. The results of these codes indicate that with ^{11}B target foil of 5.0 cm diameter surrounding a D-T generator operating at 10^{8} neutrons s^{-1}, a calibration source strength of 1 ^{8}Li decay s^{-1} is possible in the present SNO geometry.

c) ^{17}N

The nucleus ^{17}N decays via beta-delayed neutron emission (> 95% B.R.) with a half-life of 4.4 s. Detection of the beta particles, by photons created in a scintillator-decay chamber for instance, would thus provide a tag for each neutron created in such a source. This would provide an extremely useful way of determining the absolute neutron detection efficiency of the SNO detector. Beta-neutron coincidences observed in the D_2O would also be a way of calibrating the efficiency of a proposed method of on-line background determination in the SNO detector.

We propose to produce ^{17}N via the ^{17}O(n,p) reaction with 14 MeV neutrons from a D-T generator. We have attempted to validate this scheme by transporting recoils from a 50% enriched $W^{17}O_3$ target foil by a nitrogen gas stream in a capillary at the D-T generator facility. We attempted to detect the decay neutrons from ^{17}N in a NE213 liquid scintillator detector. However, the detection rate to background ratio in this scheme was insufficient to observe the predicted production rate of ^{17}N atoms. Therefore, LBL has purchased 1 STP litre of 55% enriched $^{17}O_2$ gas to be used as both target and transport carrier gas in a recirculating gas-capillary scheme for producing this source.

2.3.2.5 Miscellaneous SNO Work

E.D. Earle and B. Sur

The CRL-SNO group continues to interface with the other SNO project institutions and to perform a variety of work that can be done most efficiently at CRL.

One of the main responsibilities of the Associate Director is to ensure that proper procedures for the transfer of D_2O are in place. SNO has set up a Heavy Water Management Authority which is interfacing with CRL Nuclear Materials Branch, the AECB, AECL CANDU and Ontario Hydro. Programs to test the D_2O and to make the brine for SNO at CRL are being developed.

The calibration sources to be deployed in the vessel must be manipulated. CRL engineers have produced a conceptual design of a boom arrangement that meets the SNO specifications. However, at the present time a cheaper string design is being explored at Queen's University, but it does not yet meet the specifications.

CRPP's major responsibility within the SNO project has been the water systems. Because these systems include the D_2O systems and the monitoring of water for Rn, the overlap of CRL and CRPP responsibilities is increasing. It is expected that some of the CRPP work load, which the SNO management has identified as onerous, will be transferred to CRL.

2.3.2.6 Overview of the SNO Project

J.D. Hepburn (SNO Site Manager at the Creighton Mine of INCO, Sudbury)

The construction work required to convert the laboratory and detector excavations underground into useable space has continued. Difficulties with the transportation of construction personnel have been minimal, and productivity (hours per day per worker) has been higher than expected. The difficulties of doing construction work underground, mainly related to many people working in a confined space, have been addressed by holding frequent coordination meetings. Material transport has been maintained by organizing, roughly once per month, a special shift devoted to movement of SNO materials underground.

While construction is approximately 80% complete, the schedule has slipped about six weeks. It is hoped to pick up some of this time in the detector installation phase. In December a problem appeared with the movable assembly platform in the cavity. This is being resolved, but has led to an additional delay in other cavity work; all other work is continuing as planned. The present date for start of the clean phase construction is late January.

Off-site progress continues to be good. The most notable achievement was the complete assembly, above ground, of the photomultiplier-tube, geodesic support structure produced by the Lawrence Berkeley Laboratory. The dismantled, cleaned structure is now in Sudbury awaiting assembly. Delivery of photomultiplier tubes with bases (from Queen's University) and reflector assemblies (from Oxford University) to Sudbury is on schedule.

The Canadian funding agencies approved an additional $15.4M for completion of the project. All activities are now under even closer scrutiny for costs.

Plans are in place to work a full three shifts per day, five days per week during the two-month INCO shutdown that starts January 3.

2.3.2.7 SNO Project Management

J.D. Hepburn (SNO Site Manager at the Creighton Mine of INCO, Sudbury)

The combined site offices of Monenco-Agra/Canatom and SNO operated smoothly, with local purchases being arranged through Laurentian University and others via Queen's University.

The Surface Assembly building, in which the photomultipliers, reflectors, and mounting panels will be assembled, was declared in-service on October 13. Staff has been hired, and all equipment and procedures are in place for a January 3 start of production.

Operational aspects of the laboratory controls, monitoring and alarms systems have been considered. The system will use the same hardware and software as the water system controls. It is a supervisory system only; all operating systems have their own local, autonomous controls.

SNO site staff have been making regular visits underground to inspect work and ensure that the requirements are being met. So far, although many points have been noted and amended, no fundamental problems have appeared.

Assistance has been given to physicists visiting on site, for such purposes as: work in the low-background laboratory on the 4600 ft. level, tests of as-installed magnetic coils and a prototype power supply for them, measurement of air pressure changes (resulting from INCO turning on and off various mine ventilation fans), and quality control tests on urylon coatings (leading to QC on installation of the main cavity liner).

The first submission to NSERC for laboratory operating funds was made.

Much work has been required to specify and purchase equipment needed for operations. This is now virtually complete, in time for the start of operations in January of service water, electrical, and HVAC systems.

Experience with cleaning procedures has been gained by establishing a clean room in which HVAC ducting was assembled prior to installation. Also, the cavity deck and control room steelwork has been cleaned in preparation for repainting.

Site manager participation in overall project management continued, including aspects of costs, scheduling, accounting, inventory, insurance, invoice approvals, and attendance at project/design coordination and project progress meetings.

2.3.3 Nuclear Data and Modelling

2.3.3.1 Sensitivity of Self-Powered Detector (SPD) Probes to Electron and Gamma-Ray Fields

M.A. Lone with P.Y Wong (Mathematics and Computation Branch)

A Self-Powered Detector (SPD) is a simple passive device, consisting of a coaxial probe with a metallic outer sleeve known as a collector, a mineral oxide insulating layer, and a metallic inner core called an emitter. SPD's are used in nuclear reactors for monitoring neutron and gamma fields (R.B. Shields, Self-Powered Flux Detectors, A Bibliography with Summaries, AECL-8109, (1983)). Responses of SPD's to electrons and gamma-rays of various energies were investigated with Monte Carlo simulations using the ITS code (J.A. Halbleib, R.P. Kensek, T.A. Mehlhorn, G.D. Valdez, S.M. Selzer and B.J. Berger, Sandia National Laboratory Report SAND91-1634(1992)). Transmission filters were studied for design of threshold SPD's for on-line monitoring of the energy spectrum of high-power industrial electron accelerator beams. Filters were also investigated for enhancement of the gamma ray sensitivity of an SPD placed in a mixed electron and gamma-ray field.

A suitable SPD for monitoring of electrons is one with an outer sleeve collector made of a low Z material, and an inner electrode (emitter) of a high Z material. This configuration provides high sensitivity and a sharp threshold for electron energy. For normal operations the outer sleeve of an SPD is connected to an electrical ground and the emitter is connected to a low impedance load for derivation of the SPD signal from the charge collected at the emitter. Fig. 2.3.3.1 shows the calculated charge build-up in the emitter zone of SPD's built with, 1.8 mm diameter emitter, 0.31 mm thick MgO insulator zone, and Inconel-600 collector of wall thicknesses ranging from 0.7 mm to 6 mm. The signal from the emitter displays features typical of a threshold device. The threshold for detection of electrons is found to be approximately equal to the energy at which the electron range is equal to the collector wall thicknesses. This collector material serves as a transmission filter. If

we define an SPD probe threshold as the electron beam energy at which the charge build-up in the emitter is only 1% of its peak, then the information in Fig. 2.3.3.1 shows that the threshold energy depends linearly on the thickness of the Inconel-600 collector. Spectral distribution of an electron beam may be determined by unfolding techniques from SPD data collected simultaneously with judiciously selected collector thicknesses.

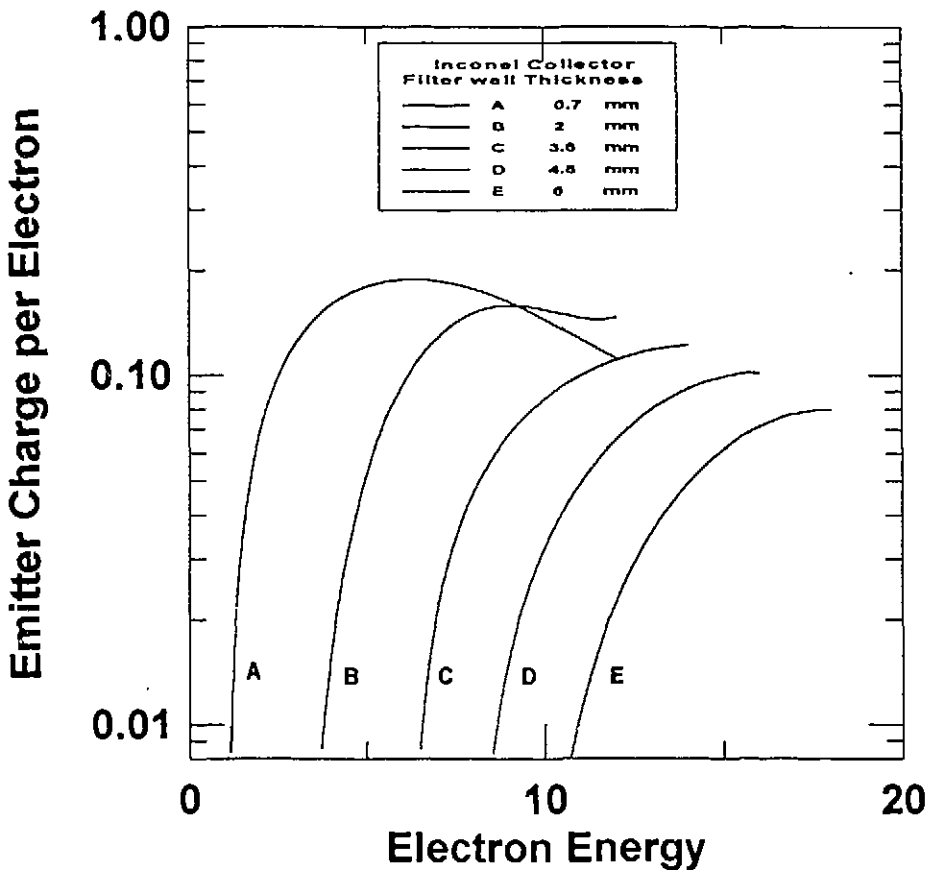

Fig. 2.3.3.1 Charge build-up in the emitter zone of SPD, with emitter 1.8 mm dia W, insulator 0.31 mm thick MgO and Inconel-600 collectors of various thicknesses.

An optimum SPD for monitoring of gamma rays consists of a collector of a low Z material and an emitter of composite Z material. For these SPD's the inner core of the emitter could be made of a low Z material with a thin cladding of a high Z material like Pt. Because of the small dimensions of a typical SPD, the gamma interaction probability is low and the SPD's in general have low probability of charge build-up at the emitter arising from the interaction of an external gamma ray compared to an external electron.

Furthermore, the charge build-up from the external gamma-ray-induced electron emission from the emitter zone is opposite to that from the implantation of the external electron in the emitter zone. In addition, if the SPD is surrounded by a medium, then the gamma-ray interactions in this medium will produce electrons that propagate with the gamma-ray field. Thus the net signal from an SPD probe placed in a gamma field may depend on the environment of the SPD probe.

Fig. 2.3.3.2 displays the gamma-ray sensitivity calculated for an SPD probe with a Pt-clad emitter (Inconel core diameter 1.44 mm with 0.062 mm Pt clad), MgO insulator (0.33 mm thick), and Inconel-600 collector (thickness 0.386 mm). The sensitivity was calculated for various configurations and surrounding media of air and water including transmission filters of Zr and Pb. In Fig. 2.3.3.2 the curve with solid data points shows the sensitivity of a bare probe placed in air. The rapid rise above 2 MeV results from escape of γ-induced high energy electrons from the emitter zone.

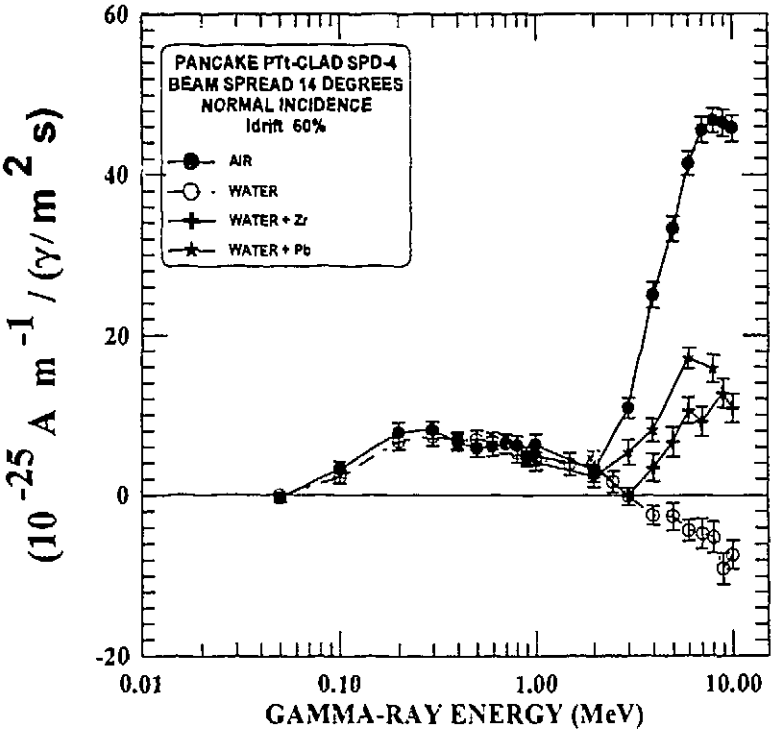

Fig. 2.3.3.2 Gamma-ray sensitivity of a Pt-clad SPD with, emitter of 1.44 mm diameter Inconel-600 core plus 0.062 mm Pt clad, insulator of 0.33 mm MgO, and Inconel-600 collector of 0.386 mm wall thickness. The legend identifies the surrounding medium and the configuration.

The curve with the open circle data points shows the response when the detector is surrounded by a water medium in the same gamma-ray field. The external electrons generated in the water penetrate the detector, and collection of these in the emitter zone generates a negative charge at the emitter. The wall thickness of the collector of this probe stops external electrons of energy below 1 MeV; consequently, the sensitivity below 1 MeV is found to be independent of the surrounding medium.

Surrounding the SPD with a high density high Z medium such as Zr or Pb reduces contributions from the external electrons. This is clear from the data shown in Fig. 2.3.3.2. Earlier reports (N.P.Goldstein, IEEE Tran. NS 20 (1973), 549; D.S. Hall, IEEE Trans. NS 29 (1982), 646) had stipulated that there is no difference with respect to the Z of the surrounding medium. However, the codes used in those studies did not include the bremsstrahlung mechanism and there may be differences in the treatment of the multiple scattering of electrons. Our findings show clearly that filters of high Z materials surrounding SPD suppress the overall contribution of external electrons and may be necessary for monitoring of broad energy gamma-ray fields in a water medium. Without these filters, the contribution from low- and high-energy gamma rays and their associated electrons may cancel out and reduce the magnitude of the net signal.

So far, we have considered probes with a high-Z Pt cladding on the emitter. The photo electric process in this high Z cladding material provides the higher sensitivity at low gamma-ray energies. This is demonstrated by the data shown in Fig. 2.3.3.3 calculated for a probe similar to that discussed in Fig. 2.3.3.2, with the exception that the Pt cladding is replaced with Inconel. The absence of a high Z material in the emitter results in a reduction of the emission of electrons from the emitter by the photo electric process. The sensitivity of this probe is almost zero at gamma-ray energy below 1 MeV, and is very sensitive to the magnitude of the electron drift from the MgO insulator region.

Again for gamma-ray energy above 1 MeV the sensitivity depends on the surrounding medium. In air the sensitivity increases because of the increasing loss of the number of Compton electrons from the emitter. The charge build-up at the emitter arising from the electrons coming from a water medium is greater than the direct gamma-ray interactions in the emitter, and results in the reversal of the polarity of the signal from the emitter. Insertion of a transmission filter of high Z material such as Pb reduces the contribution from the external electrons and maintains the polarity of the signal.

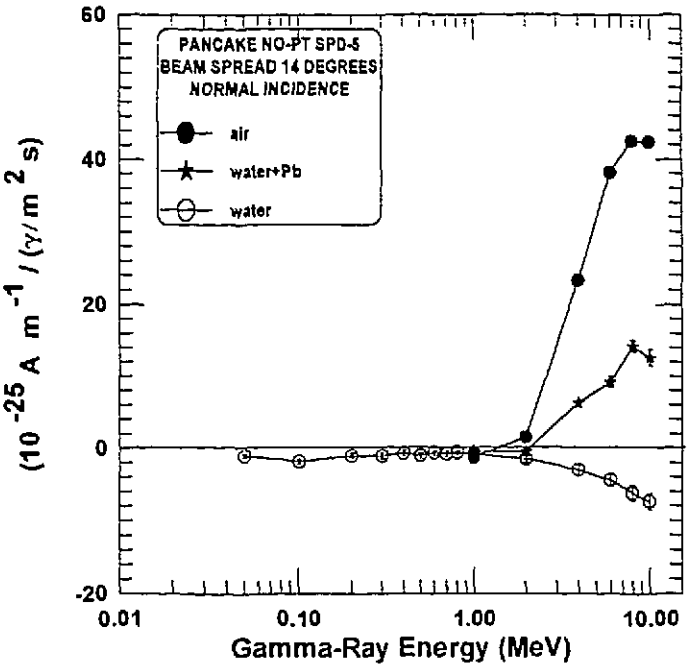

Fig. 2.3.3.3 Gamma-ray sensitivity of a low Z emitter SPD. The Pt-clad on the emitter of the SPD in Fig. 2.3.3.2 is replaced with Inconel-600. The legend identifies the medium surrounding the SPD.

2.3.3.2 Measurement of the Sensitivity of an SPD Probe in ^{60}Co and ^{192}Ir Gamma-Ray Fields

M.A. Lone and M. Montaigne

The sensitivity of a Self-Powered Detector (SPD) probe was measured in ^{60}Co and ^{192}Ir gamma-ray fields using the irradiation facilities at Chalk River Laboratories. The SPD probe (Pt-clad emitter of 1.44 mm Inconel core with a 0.062 mm Pt clad, MgO insulator of thickness 0.33, and an Inconel-600 collector of wall thickness 0.386 mm) was coiled in a pancake shape with an outer diameter of 9 cm. The electrical current from the probe was measured using a Keithly 487 picometer. This instrument was calibrated using a Keithly 261 current source. The calibration accuracy ranged from 0.6% for the nA range to 1.7% for the 0.01 nA range. The background current readings were in the sub pico-ampere range. In order to reduce this background current, proper precautions were taken to eliminate ground loops and mechanical vibrations of the probe and the lead cables.

The ^{60}Co facility at CRL is a gamma-220 cell that contains a cylindrical sample chamber of height 20.5 cm and diameter 15 cm. In irradiation position the chamber is surrounded by 16 source pencils that are placed near the circumference. The gamma field in the chamber is calibrated with a Ferris Sulfate dosimeter and for the period of our measurements the dose rate at the centre of the chamber was (0.33 ± 0.017) M rad/h in a tissue equivalent material. This dose rate is equivalent to a flux of 1.56×10^{15} (γ/m^2s) of gamma rays of 1.25 MeV average energy. The dose is fairly uniform at the centre but varies by about 5% near the edges of the irradiation chamber and the measurements were repeated with the probe placed at different locations in the irradiation chamber.

The gamma flux in the cavity contains a low energy component from the back scattered 0.25 MeV gamma rays. Earlier studies (R.B. Shields, AECL-3564 (1970)) had indicated two components with effective energies of 1.25 MeV and 0.25 MeV, and fluxes in the proportions of 91.1% and 8.9%, respectively. The contribution to the dose is in the proportion of 98.1% from the 1.25 MeV gamma rays and 1.9% from the 0.25 MeV. With this division of the observed 0.33 M rad/h dose in the gamma-220 cell, the fluxes of 1.25 MeV and 0.25 MeV gammas are, respectively, 1.52×10^{15} and 0.14×10^{15} (γ/m^2s) . The uncertainty in these values from the dose and conversion factors is estimated to be about 7%.

Measurements showed that the sensitivity did not depend on whether the probe was in air or in water. This is in complete agreement with our computed results as discussed in section 2.3.3.4. The total current in the probe calculated for the two-component gamma field in the cell is 0.6 nA, compared to the measured value of 0.71 nA. The current computed using the calculated sensitivity data reported by Hall (IEEE Trans. NS 29 (1982), 646) for a similar type probe is 0.16 nA at 1.25 MeV. This is almost a factor of four smaller than our measured value.

The ^{192}Ir radiography inspection facility at CRL uses industrial ^{192}Ir gamma cameras. The source half-life is 74.2 days. The gamma-exposure device consists of a source storage castle with a teleflex source guide tube containing a crank and cable assembly. A source of dimensions 2 mm by 3 mm is at the tip of this cable and can be cranked to the inside of a thin-walled exposure tip of the guide tube. Two cameras were available. Measurement were made using both cameras by positioning the exposure tips at equal distances on either side of the probe. The probe lead cable was encored firmly, in order to reduce the mechanical vibrations that generated background noise current. The whole assembly was in air on top of a wooden bench.

The nominal strength of the two sources listed on the shipping papers was 46 curies on the day of the experiment. The strength of the industrial sources is determined by dosimeters using a conversion factor of 0.5 R/h per curie at 1 meter distance. The disintegration of ^{192}Ir by beta decay (95.3%) and EC (4.7%) produces 2.28 gammas of average energy 0.35 MeV. Measurement were made as a function of the distance

from the sources, and the results are given in Table 2.3.3.1. The measured signal from the SPD shows the $1/R^2$ variation expected for an isotropic source. However, there is a systematic discrepancy of about 30% from the calculated value, but this is comparable to the overall uncertainty of 25% in our measurements. The estimated uncertainties are 10% source strength, 20% gamma branch, 10% solid angle, and 5% picometer calibration. Fig. 2.3.3.4 shows that the measured values of the SPD sensitivity in ^{60}Co and ^{192}Ir γ-ray field are in good agreement with our Monte Carlo simulations.

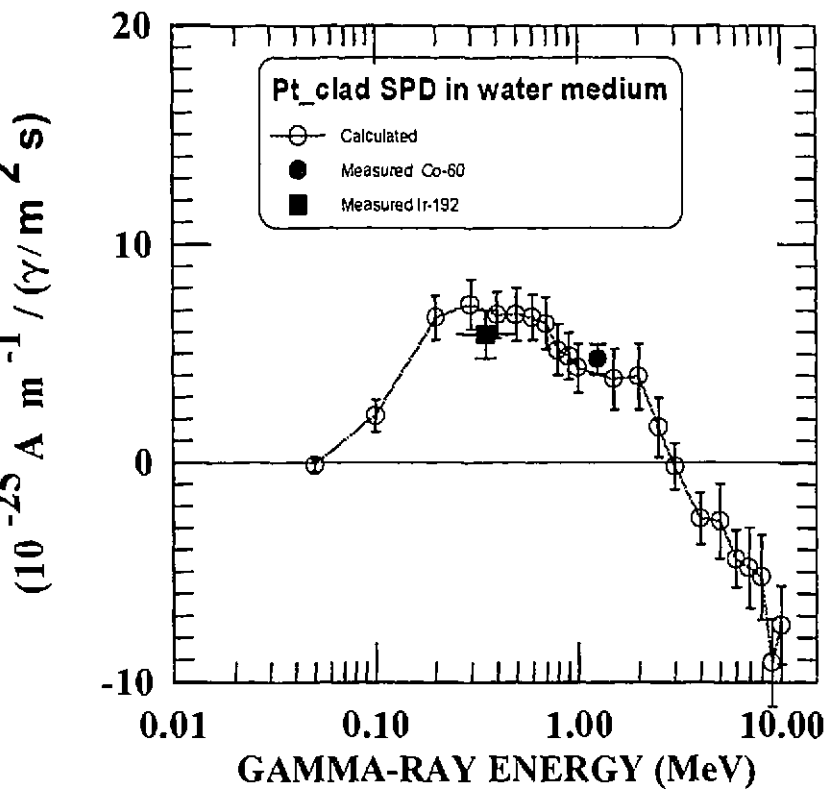

Fig. 2.3.3.4 Comparison of calculated and measured gamma-ray sensitivity in water of a Pt-clad SPD with emitter of 1.44 mm diameter Inconel-600 core plus 0.062 mm Pt-clad, insulator of 0.33 mm MgO, and Inconel-600 collector of 0.386 mm wall thickness. The legend identifies the gamma-ray source.

TABLE 2.3.3.1

Summary of Data from Measurements in ^{192}Ir

Run	Distance from Source (cm)	Flux $10^{13}(\gamma/m^2.s)$	Measured Current (pA)	Calculated Current (pA)
1	5	12	35.3	71
2	10	3	11.5	17.8
3	15	1.3	5.1	7.6
4	20	0.75	3.0	4.4
5	30	0.33	1.1	2.0

2.3.3.3 Nuclear Fluxes in a Water Target Exposed to Solar-Flare Protons

M.A. Lone with P.Y. Wong (Mathematics and Computation Branch) and J.L. Shinn and J.W. Wilson (NASA Langley Research Center)

Over the last several years, a family of deterministic transport codes (J.W. Wilson et al., Transport Methods and Interactions for Space Radiations, NASA RP-1257 (1991)) developed at NASA Langley Research Center has been used as the engineering tool in radiation-shielding analysis for various space missions. These codes assume the straightahead approximation (J.W. Wilson, NASA TP-2178 (1983)) with the data base containing a rather detailed description of the basic physical processes, and yet are computationally efficient when compared to Monte Carlo codes.

For verification of the deterministic codes, the secondary energy spectra of protons and neutrons in a 100 g/cm^2 thick water target exposed to the 1956 February solar-proton spectrum were calculated using the deterministic baryon transport code (BRYNTRN) and the Monte Carlo code LAHET (Los Alamos High Energy Transport Code -P.R. Prael and H. Lichtenstein, LA-UR-89-3014 (1989)). The comparison of the detailed neutron and proton spectral shapes at various layers in the water target is a stringent test of the representation of the actual physics involved.

Fig. 2.3.3.5 and Fig. 2.3.3.6 show a comparison of the energy spectra of neutron spectrum at 1 and 30 cm depth in a 100 cm thick water target as calculated by BRYNTRN and LAHET. There is a reasonable agreement at 30 cm depth, but at lower depths the BRYNTRN code predicts lower values of the neutron flux. It appears that the neutron albedo (neutrons coming back from deeper layers), which is not currently treated in BRYNTRN, might be a cause for this discrepancy.

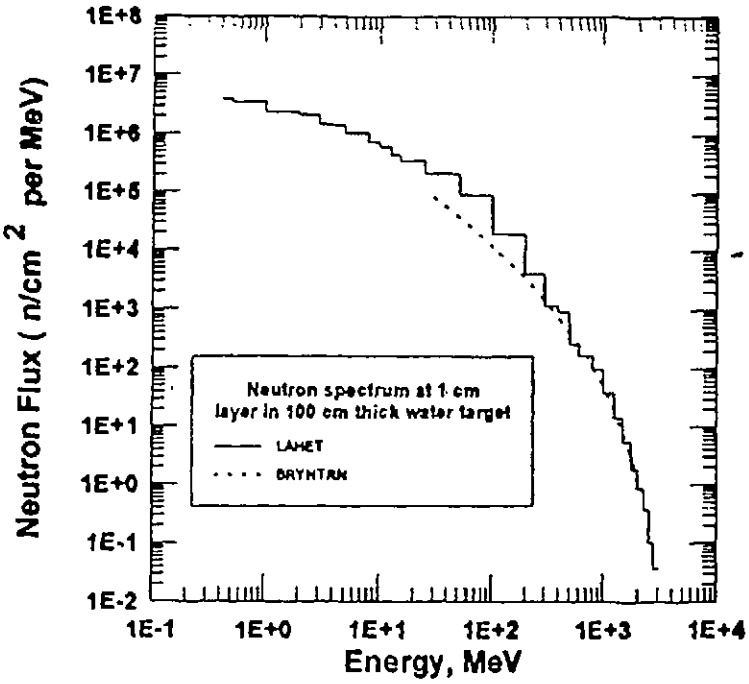

Fig. 2.3.3.5 Neutron flux at 1 cm depth in a 100 cm thick water target exposed to the 1956 February solar-proton spectrum.

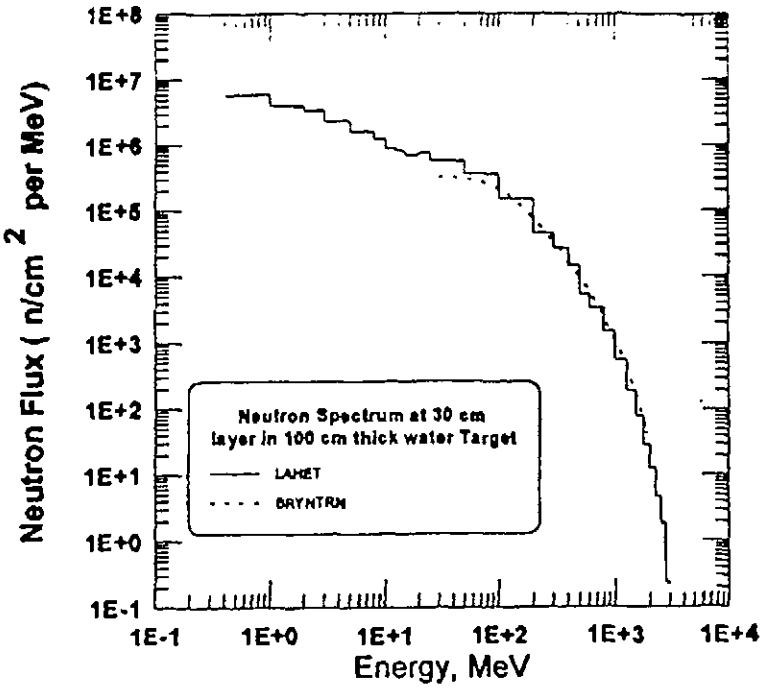

Fig. 2.3.3.6 Neutron flux at 30 cm depth in a 100 cm thick water target exposed to the 1956 February solar-proton spectrum.

Furthermore, it appears that the non-elastic neutron production cross sections in BRYNTRN may underestimate results from the Bertini interaction model incorporated in LAHET.

2.3.3.4 Spectra of Secondary Neutrons and Protons from Interactions of 100 to 1000 MeV Protons in 2 cm Thick Al

M.A. Lone with P.Y. Wong (Mathematics and Computation Branch) and H. Ing (BTI, Chalk River)

Bubble detectors (H. Ing and H.C. Birnboim, Nuclear Tracks and Rad. Meas. 8 (1984), 285) provide a convenient and novel technology for measurements of neutrons. Bubble detector spectrometers have been flown in three space missions: Bion-9, Bion-10 and MIR, for in situ monitoring of the neutron radiation fields. In a joint project between BTI and CRL, we are re-analyzing the observations made in these missions. For this purpose the energy spectra of secondary protons and neutrons produced by the interactions of 100 to 1000 MeV protons in 2 cm thick Al were computed with the Monte Carlo code LAHET. Fig. 2.3.3.7 shows the calculated spectra of secondary neutrons.

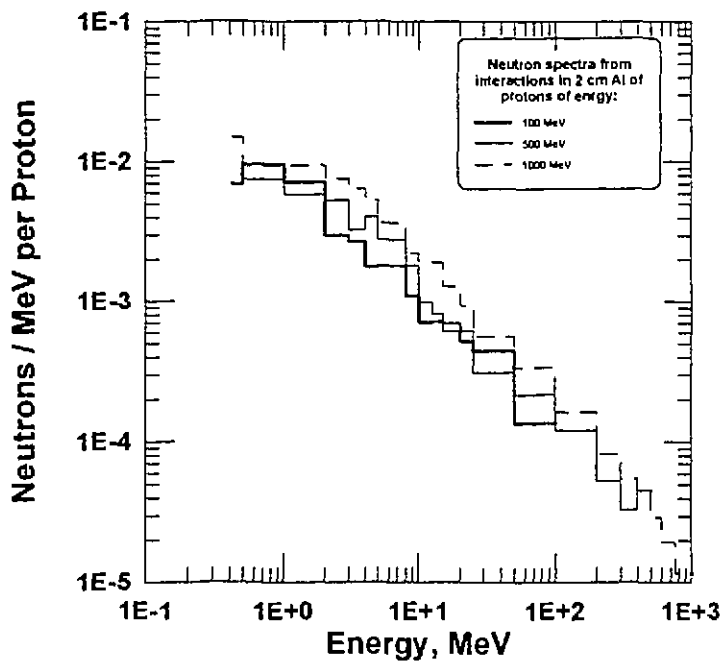

Fig. 2.3.3.7 Spectrum of neutrons produced by interactions of protons in a 2 cm thick Al target. The legend identifies the proton energy.

Previously the data from these space measurements had been analyzed using response matrices originally established by calibration with monoenergetic neutrons at energies below 17 MeV. The newer computed spectral distributions of neutrons and protons inside the spacecraft are being used to re-assess the bubble detector response at high energies using reaction data and to re-examine the spectral results obtained from earlier analysis.

2.3.3.5 The Iterated Prisoner's Dilemma Problem

T.C. Hsu with S. Schroeder, J. Mortimer and M. Panju (Deep River Science Academy) and L. Hsu (University of Waterloo)

A study of the Lattice Iterated Prisoner's Dilemma was completed.
The iterated prisoner's dilemma problem is an interacting many-body problem in which competing strategies repeatedly play a 2x2 "game" with two choices, 'cooperate' or 'defect'. From the point of view of one competitor it is always more favourable to choose defect, but if the game is repeated then it may pay to develop a cooperation between two competitors. The effect of the restriction of the play of this game to near neighbours was studied by computer simulation. Interesting and novel collective behaviour was found. In particular it was found that multiple strategy "communities" could be sustained indefinitely. The Lattice Iterated Prisoner's Dilemma is related to many-body physics, because it shares the property that interactions between near-neighbours affect long-distance and long-time correlations of the system as a whole.

2.3.4 Instrumentation

2.3.4.1 Bench Marking of the C5 Polarized Neutron Triple-Axis Spectrometer

D.C. Tennant and Z. Tun with R.L. Donaberger (McMaster University)

One undesirable feature of spin polarized neutron beams produced by ferromagnetic crystal monochromators is that the flux of higher order neutrons (with wavelengths $\lambda/2$, $\lambda/3$, etc., where λ is the desired wavelength) in the beam is unacceptably high. In the case of Cu_2MnAl Heusler crystals routinely used on the DUALSPEC facility (the C5 Polarized Beam Triple-Axis Spectrometer), the problem is so serious that, apart from a few special cases, the experiments could not be performed without a proper neutron filter. It is therefore important to measure the higher-order contamination directly, and bench mark the performance of the spectrometer for a typical configuration.

The measurements were carried out with a neutron beam chopper installed in the diffracted beam (DB) from the Heusler monochromator. The chopper allowed only a small fraction (0.76%) of the beam to pass through as short pulses (22 μs), and the

velocity spectrum of each pulse was analyzed by the time-of-flight method. The distance from the chopper to the detector was 1.5 m, corresponding to a neutron flight time of ~ 1 ms, and there was no possibility of frame overlap between adjacent pulses. The spectra obtained at various monochromator angles $2\theta_m$ are plotted in Figure 2.3.4.1. The figure shows that the flux of $\lambda/2$ neutrons in the unfiltered DB directly from the monochromator is higher than the λ neutron flux. The beam also contained some $\lambda/3$ neutrons. The ratio between $\lambda/2$ flux and λ flux is least favourable at high $2\theta_m$.

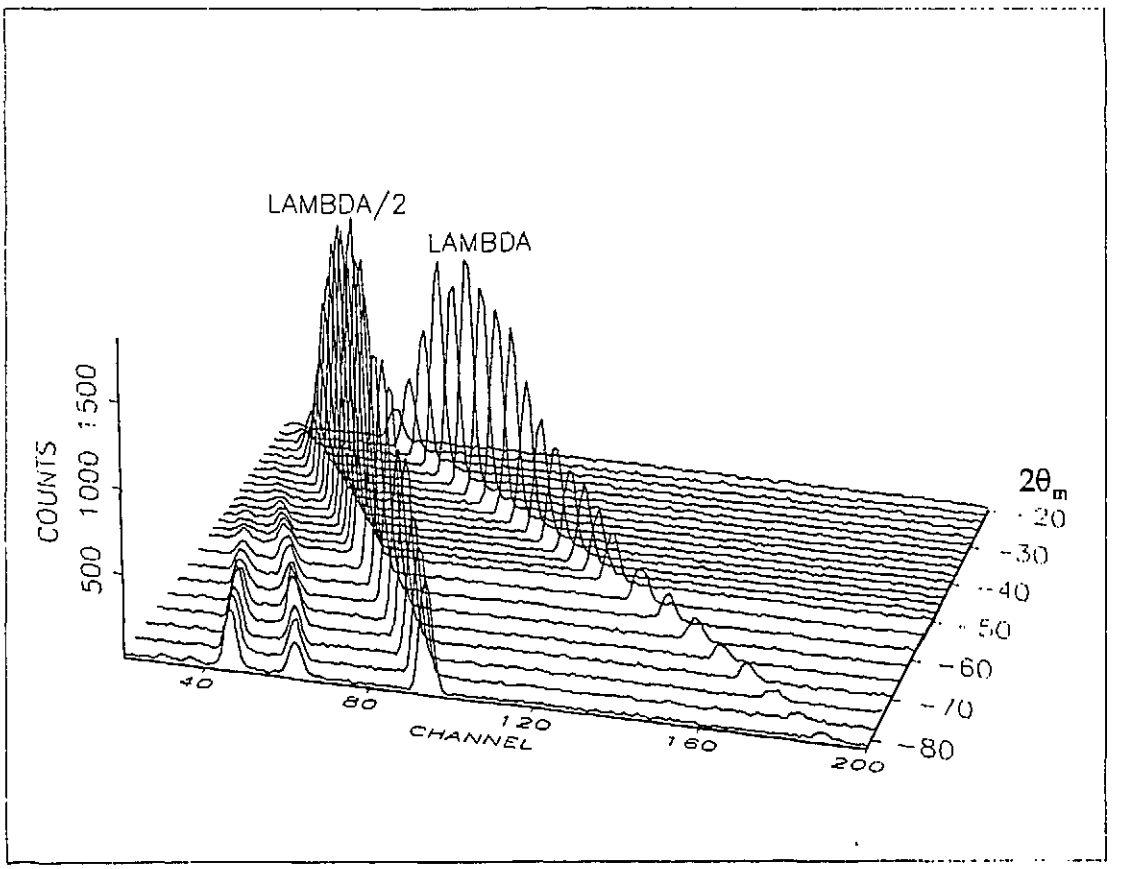

Fig. 2.3.4.1

In a typical polarized neutron experiment the spin state of neutrons after the sample is determined by another Heusler crystal used as the analyzer. In order to bench mark a fully equipped spectrometer, a Heusler analyzer and a Mezei neutron-spin flipper were installed in the straight-through beam after the sample position (i.e., $\phi = 0°$). The time-of-flight measurements were carried out at $2\theta_m = 2\theta_A = 40.37°$, a setting corresponding to one of the most "popular" wavelengths $\lambda = 2.37$Å. The

spectra, shown as Scans 1 to 6 in Figure 2.3.4.2, were measured under the following conditions:

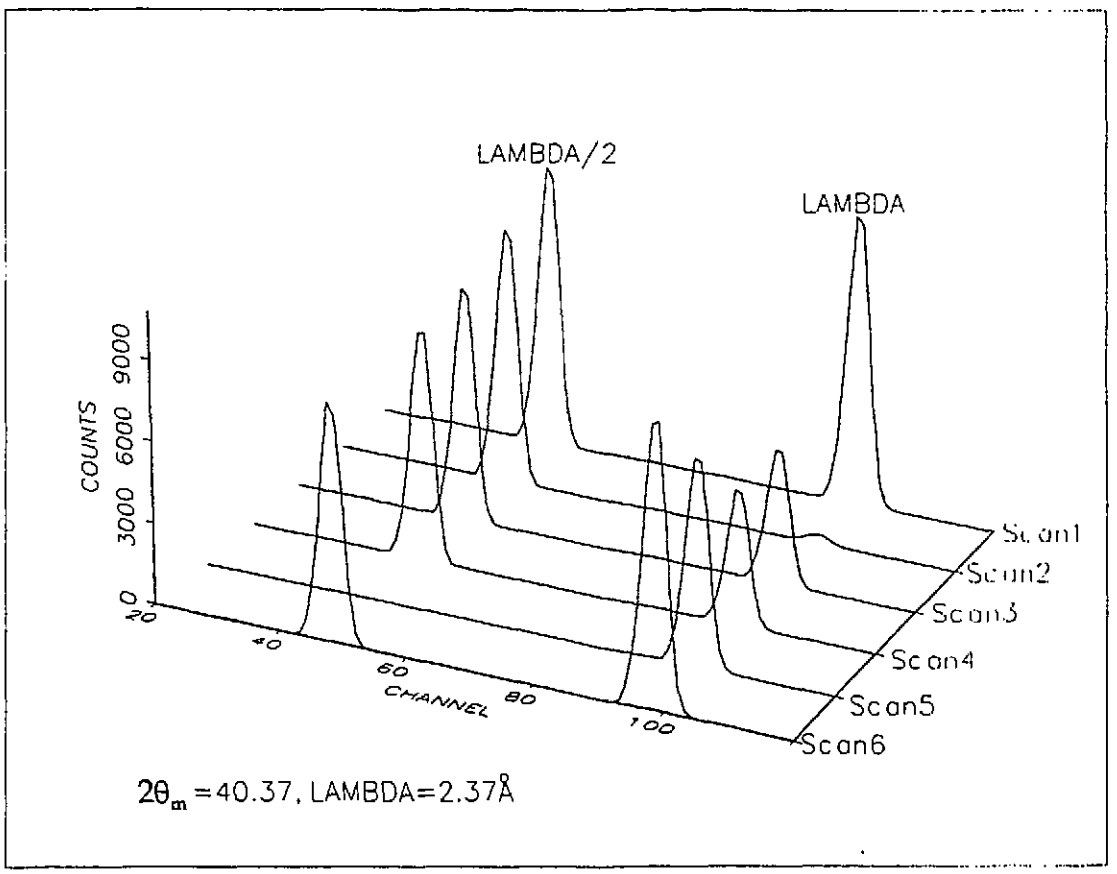

Fig. 2.3.4.2

Scan 1 Unfiltered DB flux with the Mezei flipper OFF.

Scan 2 Same as Scan 1, but the Mezei flipper was turned ON and tuned to minimize the λ neutron flux (tuned for the first minimum corresponding to π rotation of Larmor precession. Flipper currents were 1.35 Amp for the scattered beam horizontal field (SBHF), and 1.13 AMP for the scattered beam vertical field (SBVF).

Scan 3 Same as Scan 1, but with a beam depolarizer in DB. The depolarizer was a mild-steel plate inserted in the beam away from the guide fields. The stray field at the depolarizer position was 20 gauss.

Scan 4 Same as Scan 2, but with the depolarizer in DB.

Scan 5 Same as Scan 1, but the beam is filtered through a PG filter.

Scan 6 Same as Scan 2, but the flipper had been detuned; i.e., the flipping current, SBHF, was increased beyond the value set for Scan 2 so that the λ neutron flux was at the maximum corresponding to 2π Larmor precession (the maximum was found experimentally at SBHF = 2.72 Amp, SBVF = 1.13 Amp). Under this condition the flipper was tuned for $\lambda/2$ neutrons.

By comparing the scans in Figure 2.3.4.2, the following conclusions can be drawn:

1. Without filtering out the $\lambda/2$ neutrons, the highest flipping ratio one could hope for at λ = 2.37Å is ~ 2:1.

2. The ~ 30:1 flipping ratio routinely achieved on C5 is essentially limited by the flipper efficiency and not by the residual higher-order neutrons in the beam.

3. The flux of $\lambda/2$ neutrons is reduced by a factor of 1470 by the PG filter. The transmittance factor for λ neutrons is 71%.

4. The depolarization of DB by the depolarizer is complete. It can therefore be used to measure beam polarization and flipper efficiency at other wavelengths.

5. The $\lambda/2$ beam cannot produce a polarized signal even when the flipper is tuned to spin-flip these neutrons. The signal polarization can therefore be taken as a proof that an experimentally observed feature is not caused by higher-order neutrons.

2.3.4.2 Furnace Development

D.C. Tennant and J.H. Root

Maintaining specimen alignment is an inherent problem common to all high temperature furnaces in which crystals are being studied using neutron scattering techniques. A small furnace has been developed which fits on an existing Eulerian Cradle and can be easily positioned under computer control. With the furnace mounted and all the electrical and vacuum lines connected, the crystal can be rotated by more than 180° within each of the cradle's arcs (x and n). This flexibility enables the researcher not only to realign a crystal at each temperature, but also to re-orient the furnace and crystal to investigate a complete set of directions in reciprocal space.

The furnace is designed to be easily serviced and has a small hot zone to achieve high temperatures with relatively low power. The maximum specimen size is

6 x 6 x 6 mm. The vacuum is maintained by an oil diffusion pump connected to the furnace with approximately 2 m of 12 mm ID rubber tubing. A specimen temperature of 1250 K is reached with approximately 250 watts. However, further heater development is required as the present tantalum foil design tends to distort and sag rather quickly above 800 K.

2.3.4.3 Design of Slit Systems for Near Surface Strain Measurements by Neutron Diffraction

J.H. Fox and L.E. McEwan

In order to measure residual strains very close to sample surfaces affected by shot-peening, etc., special equipment is required to avoid serious systematic errors. The requirements are for very narrow exit slits (.5 - .1 mm), very close positioning of the slits to the sample and precision positioning of the sample.

The new slits were designed to be interchangeable on the supporting tunnel as in the existing design. The snout was shaped to a point in plan view with an included angle of 80°. This enables the snout to clear the sample surface at a scattering angle of 80° or more. The slits were defined by two pieces of cadmium with the gap at the apex of the pointed snout.

The snout/tunnel assembly was mounted on a precision linear stage with micrometer adjustment for fore and aft positioning of the slits relative to the sample surface. This stage was mounted in a cradle which was also mounted on a micrometer-adjustable stage at right angles. This allowed transverse positioning of the slits in the neutron beam for centering. The X, Y, Z translators for the sample were fitted with high resolution optical linear encoders. The sample can now be positioned within 5 μm (.0002") and position cannot be lost.

2.3.4.4 Direct Coupling of Encoder-to-Sample Table

J.H. Fox and L.E. McEwan

The sample tables at N-5, L-3 and E-3 spectrometers incorporate an electro-magnetic clutch between the motor drive and the rotating table. The angle reading encoder was coupled to the driver side of the clutch, so the position of the table was lost when the clutch was disengaged or slipping.

Examination of the drawings revealed that with minor modifications and a shaft extension, the encoder could be coupled to the driven side of the clutch such that the angular position could not be lost. This modification has now been completed on all spectrometers.

2.3.4.5 Beam Channel Component Tooling

J.H. Fox

The beam channel components (benders, shapers, collimators and shielding blocks) of the C-5 spectrometer are heavy and have no support when extracted from the beam channel for configuration changes. A detachable shelf was required to support the components prior to hoisting.

The shelf was designed to be quickly and easily installed and removed by one person and clears the dovetail link between the drum and the sample table. Tension rods between the outboard end of the shelf and the drum support the cantilevered load without bearing on the dance floor surface.

2.3.4.6 DUALSPEC Beam Gate Control

M. Potter and M. Montaigne, with M. Yuke (Civil and Electrical Design Branch)

The ROM-based program that controls the C2 and C5 gates has been modified. The messages displayed by the new version of the program are more descriptive, making faults easier to diagnose. Every time a gate is operated the program verifies that the optical switches used to sense the gate position are working. If a failed switch is detected the gate is stopped and a message identifying the failed switch is displayed.

In the past, the vanes that trigger the optical switches have been bent and dislocated when they collided with the taper pin that is inserted to align the gate. The shape of the taper pin has been changed to prevent it from having contact with the vanes, and an interlock switch has been added that inhibits the gate from moving unless the taper pin is fully extracted.

2.3.4.7 Spectrometer Control System

M. Potter and M. Montaigne, with K. Wright (Construction and Trades Services Branch)

The stepper motor and associated control hardware that drives the Eta axis of the Eulerian Cradle has been replaced with a high speed version. This reduces the time for one revolution of the Eta axis from 160 seconds to 11 seconds. The higher speed drive has increased the throughput of texture profile measurements from one to three per day.

The encoder electronics for the C2 and C5 spectrometers has been redesigned. In the new design, noise, caused by ground loops, has been reduced by isolating the case

and logic grounds. Also, a time delay has been added to the pulse logic line, to eliminate errors caused by a logic rack condition that occurred when a drive changed direction, and a built-in error detection circuit has been added to record an invalid output code from the encoder optical unit.

A remote hand-held control to select and drive any motor on the spectrometer has been installed at C5. The control is linked to the CAMAC by a 30 foot cable and control is implemented by an interrupt service subroutine that is part of the spectrometer control program. The control uses the motor configuration parameters such as base rate, acceleration and slew rate that have been entered into the data base by the DSCANS program. In addition to the switches used to drive the motor, the control has a 40 character alphanumeric display used to display the drive name, current position (live display), acceleration time, motor speed and off limit conditions.

2.3.4.8 Reactor Beam Hole Use

D.C. Tennant

NRU operated for 145 days between 1 July and 31 December. Spectrometer use is given below (efficiency is % of available reactor operating time used for experiments).

Beam hole	No. of experiments	No. of participating CRL scientists	No. of participating non-CRL scientists	Efficiency
C2	22	6	24	92%
C5	8	3	7	88%
E3	11	5	10	98%
L3	5	6	1	96%
N5	5	7	6	98%
T3	3	4	1	8%

2.3.5 Support Services

2.3.5.1 Multiwire ^{3}He Neutron Detectors

G.A. Sims, J.J-P. Bolduc, D.C. Tennant, H.C. Spenceley and B.M. Powell

1) 13-Wire Detectors

a) MAC-1-9-13

This unit has passed the acceptance tests performed at T3 at the NRU Reactor.

b) MC-1-8-13 (DC Grounded Anode-Prototype)

After the employment of several cathode materials, metallized alumina proved to be the most successful. A consistently clean and improved environment was achieved within the detector. This permitted a stable H.T. operation and an exceptionally low background noise rate: a favourable combination. During a 118 hour background test, no wire exhibited more than 3 counts/hour (see Fig. 2.3.5.1). Also, no shift in peak channel was observed over a 15-day run.

We have now progressed from this prototype to the production model as a result of these substantial improvements in detector characteristics and operation.

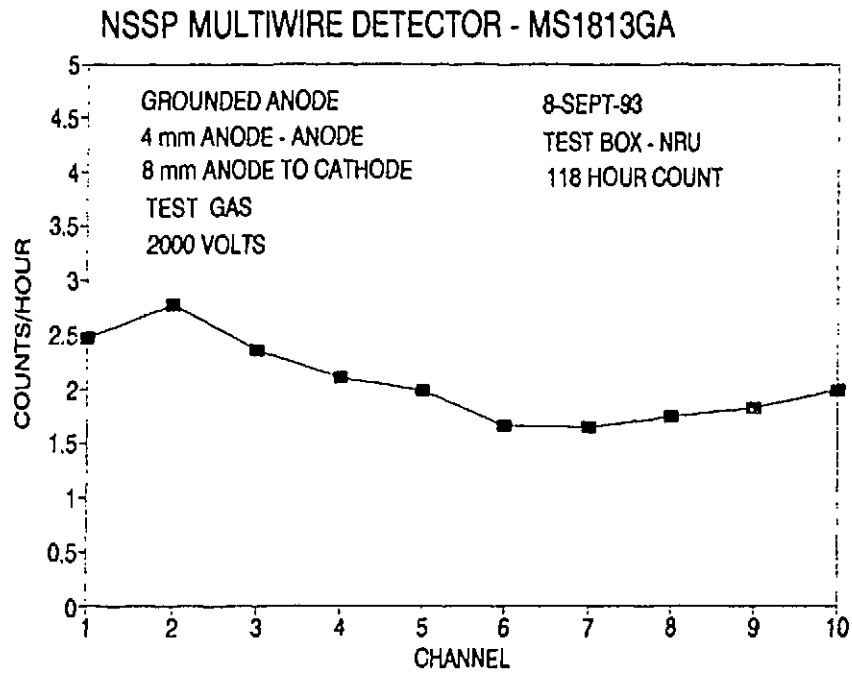

Fig. 2.3.5.1

c) MA-2-9-13 (ANDI)

This detector is continuing to demonstrate excellent reliability and performance during the reporting period.

d) MA-3-9-13

This unit remains in service and performing well for the ANDI group at the NRU Reactor.

2) 20-Wire Detectors (MA-1-2-20 and MA-2-2-20)

Fabrication and developmental studies on all multiwire detectors with a conventional H.T. anode design will not be pursued at the present time.

3) 32-Wire Detector (Grounded Anode) (MA-93-32)

The problems associated with degassing of the cathode materials, etc., were solved and the prototype detector quality was such that the fabrication of the production model was undertaken immediately.

The detector group has concentrated all its efforts on a grounded anode detector with 32 active wires. It has a 2 mm anode to anode spacing and an 8 mm anode to cathode distance. The window dimensions are 6.4 cm x 14 cm x 0.32 cm thick. A total of 38 anode wires are incorporated; however, the last 3 wires on each side are employed as field shaping wires. These particular specs are such as to meet the specific experimental needs of the ANDI group.

To date, this unit has been fabricated, cleaned, assembled, leak tested, vacuum baked (three weeks) and fingerprinted with the Residual Gas Analyser. Partial pressures of water are in the order of 3×10^{-9} torr. This is a factor of 10 better than our best previous readings. An indium seal design has replaced the Helicoflex ∆ seal (metal o-ring) previously used on the smaller detector bodies. The 32 preamps and mother board are wired directly behind the detector body and are housed in an integral unit attached to the detector. This configuration will be tested along with the detector early in 1994.

2.3.5.2 New AMS Counter

G.A. Sims and H.C. Spenceley, with H.R. Andrews (Nuclear Physics Branch)

A second assembly consisting of the ΔE stage, Bragg detection system, Frisch grid, valves, feedthroughs and mounting plate has been constructed and assembled. This unit has since been delivered to the Nuclear Physics Branch to be utilized as a spare/prototype assembly.

2.3.5.3 Elastic Recoil "Backgammon" Detector

G.A. Sims with J.S. Forster (Nuclear Physics Branch)

The construction drawings for this detector have been completed. Fabrication will commence as soon as the necessary materials arrive on-site (1994 January).

2.3.5.4 Gas Handling Station #2

G.A. Sims

A second detector pumping/filling system has been assembled and has been in operation for the last 3-4 months. It is pumped by a turbomolecular pump with residual gases and contaminants monitored by a RGA (Residual Gas Analyser). This system will alleviate many of the delays that were experienced whenever pumping/vacuum baking were necessary on more than one detector.

2.3.5.5 Cryopumping Station Upgrade

G.A. Sims

The old unreliable CTI Cryotorr 7 pump has been removed and replaced with a Cryotorr 8 unit. All the necessary vacuum plumbing and gauging for this unit are now complete. A significant increase in pumping speed and dependability will be demonstrated with this upgrade.

2.3.5.6 Ge Detector Repairs

J.J-P. Bolduc

Seven Ge detectors from Fuel Engineering and one from Neutron Radiography were repaired during the six-month period.

2.3.5.7 Mechanical Laboratories

L.E. McEwan and H.C. Spenceley

The "SNO" Cryotrap Test Rig Mark II is complete, has been tested and is in use. The water-trap for radon detector for SNO has been started and should be completed by the end of the year.

The miniature light bulb furnace is now complete. It has been tested and used for its first experiment.

A specimen environment chamber furnace has been started. Most components have been fabricated, but some problems remain to be solved.

Movement limiters were manufactured and installed on both curved monochromators.

A shelf for C-5 was made and is now ready to be installed.

Linear encoders were ordered and mounted on the ANDI X-Y table.

A break-away snout and a near-surface snout have been manufactured and are now in use by the ANDI group.

Other work completed includes an adjustable graphite filter, eight vanadium cans for powder samples, seven crystal mounts and 16 varied sample preparations for ANDI.

The work done in Building 116 Mechanical Laboratory was as follows:

About 70% of the time was spent on multiwire detectors, the 20 and 32-wire and A.M.S. Detector.

About 15% of the time was spent on cutting silicon crystals for monochromators.

About 15% of the time was spent for SNO and the Glassblowing shop, machining lucite blocks for optical checks for SNO.

Manufactured jigs to hold glass and quartz.

2.3.5.8 Glassblowing Laboratory

D.A. Doering

Major jobs completed during the period are listed by branches as follows:

Chemical Operations

One hundred and fifty-eight alumina columns, fifty-two bent 35/20 ball joints and six final product recovery headers were made for the ^{99}Mo isotope production.

Waste Management Systems

In order to identify liquid waste contained in forty-five gallon drums, fifty glass sampling tubes were made.

Environmental Research

Eleven glass connectors and six large tritium, air molecular sieve traps were fabricated for an IAEA Romanian contract.

Thermalhydraulics

Construction of prototype No. 4 of the reactor vault moderator cooling safety valve was completed, to demonstrate its passive cooling abilities. Fabrication of the first prototype glass reactor shutdown absorber was completed.

Fuel Engineering

Six vertical quartz reaction furnace tubes were fabricated, to allow research to continue on the development of new reactor fuels.

Reactor Materials Research

Four borosilicate glass cells were fabricated, with platinum wire seals through the glass walls.

Two fifteen and three quarter inch diameter glass circles were cut out of flat glass for vacuum gauge windows.

System Chemistry and Corrosion

Thirty-five thin-walled NMR tubes were modified to study irradiated water solutions.

Fuel Materials

Emergency repairs were made to two quartz tubes broken in transit from Germany. This allowed a visiting German scientist who was conducting a one-month scientific study to complete the experiment on time.

Chemical Engineering

Five quartz plasma tubes with tangential entrances were repaired and two new ones were constructed, to allow experiments to continue on the decomposition of H_2S into H_2 and S. Five borosilicate glass, water-cooled columns with rectangular glass centre tubes were fabricated.

Several interconnecting glass pieces were constructed for a parylene film coating apparatus.

Nuclear Physics

Four quartz water-cooled aerosol generators were repaired to fit a temperature-controlled vacuum oven, which forms an integral component of a gas transport system at the isotope separator online facility of TASCC.

Accelerator Physics

Twenty-four 6 mm quartz sample holders were fabricated to measure high temperature dielectric properties of various samples.

Physical Chemistry

Six thin-walled nuclear magnetic resonance tubes were brought to the Glassblowing shop, to have their concentricity corrected, to enable them to be spun at high frequency in the magnetic field.

Twelve NMR tubes were modified with No. 9 O-ring joints, to allow for different samples to be analyzed.

General Chemistry

Twenty cold traps with break seals were fabricated for tellurium analysis. A complete newly designed gas rack was constructed for tellurium extraction. Two, seventy-five millimetre diameter glass, tee-shaped containers were constructed, with a base to hold heavy water. Several N + O standard preparation water-cooled quartz glass vessels were constructed.

Neutron and Condensed Matter Science

A tour of the Glassblowing shop was given to Phil Gaudette and Kevin Wegner, two representatives of S.R.B. (Saunders-Roe) of Pembroke. S.R.B. makes very small tritium lights and they were interested in exchanging ideas about glassblowing with a

scientific glassblower. Because of the exchange of glassblowing skills and ideas, a contract was secured with S.R.B. to fabricate six quartz furnace tubes.

One hundred and sixty sample vials were fabricated to contain ashed acrylic, to conduct quality control checks on the acrylic sheets being produced for the underground heavy-water tank installation at the Sudbury SNO site.

Four round quartz glass domes and six 19 mm quartz flanged specimen chambers were constructed for use in the neutron scattering experiments.

A report entitled "A System for Rapid Measurements of RF and Microwave Properties up to 1400°C" acknowledged the glassblower, D.A. Doering, for his glassblowing contributions.

Two demonstrations were given in the 1993 program for the Annual Chalk River Science for Educators Seminar.

Peter A. Moss started his formal scientific glassblowing apprenticeship under the leadership of Master Glassblower D.A. Doering on November 15.

2.4 PUBLICATIONS AND LECTURES

Publications

THE LATTICE PARAMETERS OF AUSTENITE AND FERRITE IN Fe-C ALLOYS AS FUNCTIONS OF CARBON CONCENTRATION AND TEMPERATURE
M. Onink, C.M. Brakman, F.D. Tichelaar, E.M. Mittemeijer, S. van der Zwaag, N.B. Konyer and J.H. Root
Scripta Metall. Mater. **29** (1993), 1011

NON-DESTRUCTIVE EVALUATION OF RESIDUAL STRESS IN AN ALUMINA-MULLITE COMPOSITE BY NEUTRON DIFFRACTION
B.R. Marple and J.H. Root
Proc. Second Canadian International Composites Conference and Exhibition, Canadian Association for Composite Structures and Materials (1993), 685

TOPOGRAPHY OF TETRAHYDROCANNABINOL IN MODEL MEMBRANES USING NEUTRON DIFFRACTION
A. Makriyannis, T. Mavromoustakos, K. Kelly, K.R. Jeffrey and P. Martel
Biochimica et Biophysica Acta **1151** (1993), 51

POLARIZATION ANALYSIS OF MAGNETIC EXCITATIONS IN $CsMnI_3$
J-G. Lussier, R.W. Erwin, J.W. Lynn, A. Harrison and Z. Tun
Phys. Rev. **B48** (1993), 6152

THERMAL EFFECTS IN THE STRUCTURE OF AMMONIUM PERRHENATE
R.J.C. Brown, A.M.C. Harnden, J.K. Reid and B.M. Powell
Acta Cryst. **B49** (1993), 463

A NEUTRON DIFFRACTION STUDY OF ACID SITES IN H-SAPO-37
L.M. Bull, A.K. Cheetham, P.D. Hopkins and B.M. Powell
J. Chem. Soc., Chemical Communications (1993), 1196

UNIAXIAL-STRESS DEPENDENCE OF THE PHONON BEHAVIOR IN THE PREMARTENSITIC PHASE OF $Ni_{62.5}Al_{37.5}$
S.M. Shapiro, E.C. Svensson, C. Vettier and B. Hennion
Phys. Rev. **B48** (1993), 13223

MITIGATION OF HARMFUL EFFECTS OF WELDS IN ZIRCONIUM ALLOY COMPONENTS
C.E. Coleman, G.L. Doubt, R.W.L. Fong, J.H. Root, J.W. Bowden, S. Sagat and R.T. Webster
AECL-10950, COG-93-376, October 1993

NATURE OF THE ORDER PARAMETER IN THE HEAVY-FERMION SYSTEM URu_2Si_2
M.B. Walker, W.J.L. Buyers, Z. Tun, W. Que, A.A. Menovsky and J.D. Garrett
Phys. Rev. **71** (1993), 16

EFFECT OF THREE-PARTICLE CORRELATIONS IN LOW-DIMENSIONAL HUBBARD MODELS
T.C. Hsu and Benoît Douçot
Phys. Rev. **B84** (1993), 2131

FREQUENCY DEPENDENT CONDUCTIVITY OF VORTEX CORES IN TYPE-II SUPERCONDUCTORS
T.C. Hsu
Physica **C213** (1993), 305

THE SPECTRAL FUNCTION OF A ONE-DIMENSIONAL HOLSTEIN POLARON
F.J. Marsiglio
Phys. Lett. **A180** (1993), 280

LOW-FREQUENCY FLOPPY MODES IN β-CRISTOBALITE
I.P. Swainson and M.T. Dove
Phys. Rev. Lett. **71** (1993), 193

OBSERVATION OF LATTICE MELTING AT THE FERROELASTIC PHASE TRANSITION IN Na_2CO_3
M.J. Harris, R.A. Cowley, I.P. Swainson and M.T. Dove
Phys. Rev. Lett. 71 (1993), 2939

FIRST-PRINCIPLES STUDIES ON STRUCTURAL PROPERTIES OF β-CRISTOBALITE
I.P. Swainson and M.T. Dove
Phys. Rev. Lett. 71 (1993), 3610

^{3}He(n, γ) ^{4}He CROSS SECTION AND THE PHOTODISINTEGRATION OF ^{4}He
R.J. Komar, H-B. Mak, J.R. Leslie, H.C. Evans, E. Bonvin, E.D. Earle and T.K. Alexander
Phys. Rev. C48 (1993), 2375

GENERALIZED QUANTUM SYMMETRIES AND THE SUPER-ALGEBRAS $U_q(gl(1|1))$
M. Couture and H.P. Leivo
Proc. XIX International Colloquium on Group Theoretical Methods in Physics, Salamanca, Spain, Eds. del Olmo, M.A., Santader, M., and Mateos Guilarte, J. (CIEMAT) (1992), 87

YANG-BAXTER ALGEBRAS WITH GENERALIZED STATISTICS
M. Couture and H.P. Leivo
Proc. CAP/NSERC Summer Institute in Theoretical Physics on "Quantum Groups in Integrable Systems and Statistical Mechanics", Eds. Letourneux, J. and Vinet, L. (World Scientific) (1992), 33

FIFTY YEARS OF THEORETICAL PHYSICS AT AECL: 1943-1993
V.F. Sears
Physics in Canada 49 (1993), 209

THE LATTICE DYNAMICS OF CLATHRATE HYDRATES: AN INCOHERENT INELASTIC NEUTRON SCATTERING STUDY
J.S. Tse, B.M. Powell, V.F. Sears and Y.P. Handa
Chem. Phys. Lett. 215 (1993), 383

GENERALIZED DISTORTED-WAVE BORN APPROXIMATION FOR NEUTRON REFLECTION
V.F. Sears
Phys. Rev. B48 (1993), 17477

Reports

A Gd PROPORTIONAL COUNTER SYSTEM FOR USE AS A NEUTRAL CURRENT DETECTOR IN SNO
C.K. Hargrove, I. Blevis, D. Paterson and E.D. Earle
SNO-STR-93-032

^{16}N: A CALIBRATION SOURCE FOR SNO (U)
B. Sur, E.D. Earle, E. Gaudette and R. Deal
SNO-STR-93-041

POLYCAST ACRYLIC SHEETS
E.D. Earle, R. Deal and E. Gaudette
SNO-STR-93-042

POLYPROPYLENE PIPE AND BEADS
H.W. Lee, E.D. Earle, J.X. Wang, B. Knox and K. McFarlane
SNO-STR-93-065

A SI DETECTOR CRYOTRAP FOR WATER RADIOACTIVITY MONITORING IN SNO
E. Bonvin, A. Hamer and B. Sur
SNO-STR-93-066

Lectures

HEAVY FERMIONS: GIANT SPECIFIC HEAT, SPIN WAVE COLLAPSE AND INCOMMENSURATE FLUCTUATION
W.J.L. Buyers
Institute of Technology, Tokyo
1993 September 20

INDUSTRIAL APPLICATIONS OF NEUTRON SCATTERING
J.H. Root
NSERC Committee on Materials Research Facilities
1993 October 8

MAGNETIC MOMENTS IN METALS - ARE THE ELECTRONS REALLY HEAVY?
W.J.L. Buyers
Physics Department, University of British Columbia
1993 November 4

QUANTUM SPIN CHAINS
W.J.L. Buyers
Physics Department, University of British Columbia
1993 November 20

STRUCTURE AND DYNAMICS OF AMORPHOUS AND CRYSTALLINE ICE
E.C. Svensson
Physics Department, University of Ottawa
1993 December 2

MINI-COURSE ON THE HIGH FREQUENCY CONDUCTIVITY OF VORTEX CORES IN TYPE II SUPERCONDUCTORS
T.C. Hsu
Center for Superconductivity Research, University of Maryland
1993 October 5,7,14

APPARENT STRAIN EFFECTS DUE TO WAVELENGTH DEPENDENT ATTENUATION IN STEEL PLATES
T.C. Hsu
Theoretical Physics Lunch Seminar, CRL
1993 November 29

S-WAVE vs D-WAVE SUPERCONDUCTIVITY IN HIGH TEMPERATURE SUPERCONDUCTORS
T.C. Hsu with F.J. Marsiglio
Theoretical Physics Lunch Seminar, CRL
1993 November 15

HIGH-TEMPERATURE PHASE TRANSITIONS IN CALCITE AND DOLOMITE
I.P. Swainson
American Crystallographic Association Annual Meeting, Albuquerque, NM
1993 May 27

PHASE TRANSITIONS IN CARBONATES
I.P. Swainson
CINS User Meeting, Toronto
1993 September 6

LOW-FREQUENCY FLOPPY MODES IN β-CRISTOBALITE
I.P. Swainson
Department of Physics and Astronomy, Michigan State University
and Steacie Institue for Molecular Research, NRC, Ottawa
1993 November 1 and 3

QUANTUM GENERAL LINEAR SUPERGROUP, BRAID STATISTICS AND TRANSMUTATION
M. Couture
3rd International Wigner Symposium, Oxford
1993 September 5-11

FURTHER STUDIES OF A ^{14}C -- DOPED GERMANIUM DETECTOR
F.E. Wietfeldt, Y.D. Chan, M.T.F. da Cruz, A. Garcia, E.E. Haller, W.L. Hansen, R-M. Larimer, K.T. Lesko, P.N. Luke, E.B. Norman, R.G. Stokstad and I. Zlimen, B. Sur and M.M. Hindi
Asilomar DNP Meeting, 1993

Si DETECTOR CRYOTRAP FOR SINGLE ATOM RADON DETECTION
B. Sur, E. Bonvin and A. Hamer
Asilomar DNP Meeting, 1993

Cat. No. /No de cat.: CC2-11016E
ISBN 0-660-15440-4
ISSN 0067-0367

To identify individual documents in the series, we have assigned an AECL- number to each.

Please refer to the AECL- number when requesting additional copies of this document from:

Scientific Document Distribution Office (SDDO)
AECL Research
Chalk River, Ontario
Canada K0J 1J0

Fax: (613) 584-1745 Tel.: (613) 584-3311
ext. 4623

Price: C

Pour identifier les rapports individuels faisant partie de cette serie, nous avons affecté un numéro AECL- à chacun d'eux.

Veuillez indiquer le numéro AECL- lorsque vous demandez d'autres exemplaires de ce rapport au:

Service de Distribution des Documents Officiels
EACL Recherche
Chalk River (Ontario)
Canada K0J 1J0

Fax: (613) 584-1745 Tél.: (613) 584-3311
poste 4623

Prix: C